CENTRO DE INVESTIGACIÓN CIENTÍFICA Y DE EDUCACIÓN SUPERIOR DE ENSENADA, BAJA CALIFORNIA

PROGRAMA DE POSGRADO EN CIENCIAS EN ÓPTICA

Fundamentals and applications in the detection of coincident entangled photon pairs

Tesis

para cubrir parcialmente los requisitos necesarios para obtener el grado de

Maestro en Ciencias

Presenta:

Guillermo Daniel Jiménez Gómez

Ensenada, Baja California, México

2014

Tesis defendida por

Guillermo Daniel Jiménez Gómez

y aprobada por el siguiente comité

_____

Dr. Kevin Arthur O'Donnell

Director del Comité

_____
Dra. Veneranda Guadalupe Garcés Chávez

Miembro del Comité

_____
Dr. Eugenio Rafael Méndez Méndez

Miembro del Comité

_____
Dr. Hector Manuel Escamilla Taylor

Miembro del Comité

_____
Dr. Helmut Maske Rubach

Miembro del Comité

_____
Dr. Pedro Negrete Regagnon
*Coordinador del Programa de
Posgrado en Óptica*

_____
Dr. Jesús Favela Vara
Director de Estudios de Posgrado

Noviembre, 2014

Abstract of the thesis presented by Guillermo Daniel Jiménez Gómez as a partial requirement to obtain the Master of Science degree in Master in Sciences in Optics.

Fundamentals and applications in the detection of coincident entangled photon pairs

Abstract by:

_____

Guillermo Daniel Jiménez Gómez

A theoretical and experimental study is presented of the entangled photon pairs produced by spontaneous parametric downconversion in a periodically-poled KTP crystal. The quantum state of downconverted light is derived from first principles and the rate of pair detection is calculated rigorously. The quasi phase-matching condition is used to design pair-detection experiments which employ single-photon counting modules and coincidence detection logic. The theoretical results are compared with the experimental observations of the pair rate as a function of signal polar angle and crystal temperature, obtaining good agreement. The dependence of pair rate on detection aperture sizes is also studied. Applications using photon pairs are presented which include the characterization of the time response of the detectors, the determination of the phase-matching angles as a function of crystal temperature, and an evaluation of the homogeneity of the poling in the nonlinear crystal. Further results are shown with the pump laser in two-frequency operation, which are strikingly different from the results with a single-frequency.

Resumen de la tesis que presenta Guillermo Daniel Jiménez Gómez como requisito parcial para la obtención del grado de Maestro en Ciencias en Óptica.

Fundamentos y aplicaciones de la deteccion de pares de fotones entrelazados coincidentes

Resumen elaborado por:

Guillermo Daniel Jiménez Gómez

Se presenta un estudio teórico y experimental de las parejas de fotones entrelazados producidos por emisión espontánea paramétrica descendente en un cristal de KTP periódicamente polarizado. El estado cuántico de la luz espontánea paramétrica descendente es derivado a partir de principios fundamentales y la tasa de detección de pares es calculada rigurosamente. La condición de cuasi empatamiento de fases es utilizada para diseñar experimentos de detección de pares los cuales emplean módulos contadores de fotones individuales y lógica de detección de coincidencias. Los resultados teóricos son comparados con observaciones experimentales de la tasa de pares como funcción del ángulo polar del camino óptico seguido por los fotnoes llamados señal y como función de la temperatura del cristal, obteniendo un buen acuerdo. Adicionalmente, se estudia la dependencia de las tasas de pares como función de los tamaños de las aperturas detectada. Se presentan algunas aplicaciones de pares de fotones como son la caracterización de la respuesta temporal de los detectores, la determinación de los ángulos de empatamiento de fases en función de la temperatura del cristal, y finalmente se evaluó la homogeneidad del patrón de polarizaición periódico del cristal no-lineal. Tambien se presentan resultados con el láser en un modo de operación con dos frecuencias. Dichos resultados son sorprendentemente distintos a los resultados obtenidos con una sola frecuencia.

Palabras Clave: **Parejas de fotones entrelazados, entrelazamiento, emisión espontánea paramétrica descendente, SPDC.**

Dedicatory

To future students

Agradecimientos

Quiero agradecer a mis padres por haberme formado. A mis hermanos por quererme. A mis abuelos por su visión. Al Dr. Kevin O'Donnell por ayudarme a alcanzar mi potencial y ver siempre por la excelencia en mi trabajo. Al Dr. Eugenio Méndez por su honestidad y por decirme siempre lo que cree que es mejor para mí. A la Dra. Veneranda Garcés por involucrarse de lleno en la totalidad de éste trabajo y por empujar siempre para mejorar. Al Dr. Hector Escamilla por sus valiosos comentarios para corregir el formato de esta tesis y por todo el tiempo que me ha dedicado. Al Dr. Helmut Maske por sus preguntas, esperando haber contestado. A todos mis profesores y compañeros. A mis familiares y amigos.

No hubiese podido realizar éste trabajo sin el apoyo de la beca de maestría por parte del Consejo Nacional de Ciencia y Tecnología (CONACyT) y, por ello, les estoy enormemente agradecido. Agradezco tambien al CICESE por haberme recibido y permitirme ser parte de su comunidad. Es un honor ser estudiante aquí y será mi orgullo por el resto de mi vida.

Por último, quiero agradecer a mi esposa por ser como es, por amarme y por estar junto a mí.

Table of contents

Table of contents (continued)

List of figures

List of figures (continued)

List of figures (continued)

List of figures (continued)

List of figures (continued)

Chapter 1.   Introduction

In this thesis, a theoretical-experimental study is presented of the degenerate entangled photon-pairs produced by spontaneous parametric down-conversion (SPDC) in a periodically-poled KTiOPO$_4$ (PPKTP) nonlinear optical crystal with a single-frequency pump laser. The quantum state of SPDC-produced light is developed from first principles. The rate of coincident photon pair detection is calculated from this state rigorously and compared directly with experimental observations. The coincident detection of photon-pairs is performed using single-photon counting modules (SPCMs) and fast electronic pulse processing.

1.1   SPDC and entangled photon pairs

SPDC is, broadly, a quantum mechanical process in which a pump photon of frequency ω_p is annihilated while an entangled photon-pair, also referred to as a bi-photon, is created [Mandel and Wolf (1995), Malygin *et al.* (1985)]. The photon pair is said to be composed of a photon of frequency ω_s, called the signal photon, and one of frequency ω_i, called the idler photon. The frequencies and wave vectors of the down-converted photons are determined by energy conservation and the so-called phase-matching condition, which are, for interaction in bulk material [Burnham and Weinberg (1970), Friberg *et al.* (1985)]

$$\omega_p = \omega_s + \omega_i, \tag{1}$$

and

$$\mathbf{k}_p = \mathbf{k}_s + \mathbf{k}_i, \tag{2}$$

where $\mathbf{k}_j$ is the wave vector of photon j with $j \in \{p, s, i\}$, and p, s, i refers to the pump, signal, and idler photon, respectively.

Since the prediction [Zel'Dovich and Klyshko (1969)] and observation [Burnham and Weinberg (1970)] of simultaneity of the photon pairs produced by SPDC, the entangled photon-pairs have drawn considerable interest from both theoreticians [Hong and Mandel (1985), Joobeur *et al.* (1994), Klyshko (1988)] and experimentalists [Hong *et al.* (1987),

Sergienko (2001), Hamar *et al.* (2010)]. SPDC is commonly used as a source of entangled photon-pairs [Romero Sánchez (2013)] in experiments which have demonstrated distinctly non-classical, entanglement-based, effects such as ghost imaging and diffraction [Strekalov *et al.* (1995), Barbosa (1996)], violation of Bell-type inequalities [Shih and Alley (1988)], and quantum dispersion cancellation [Franson (1992), O'Donnell (2011)] among many others.

Studies using photon pairs have recently steered towards the development of technological applications such as highly-efficient heralded single-photon sources [Brida *et al.* (2011)], absolute calibration of photon detection efficiency [Klyshko (1980), Brida *et al.* (1998)], highly secure communications through quantum-key-distribution (QKD) [Marcikic *et al.* (2006), Erven *et al.* (2008)], and bi-photon spectroscopy [Yabushita and Kobayashi (2004), Kalachev *et al.* (2007)]. These studies have shown that entangled photon pairs can substantially improve existing metrological techniques, and can also provide revolutionary advances beyond classical approaches, as in the case of QKD.

Thus, SPDC is important not only as an experimentally-available tool which can be used to probe entangled quantum systems and test the fundamentals of quantum theory, but also for the development of quantum-information technology and many other applications. It is this potential which has drawn us to this most interesting field of study.

1.2 Objectives

The main focus of of this work is to experimentally study the properties of the non-classical SPDC quantum state of light. In order to achieve this, we have pursued the following objectives:

- The experimental observation of time-coincident photon pairs produced by SPDC using single photon counting modules.

- The optimization of the rate of coincident-pair detection.

- The experimental study of the angular distribution of the coincidences.

- A comparison of the observed results with the theory.

1.3 Outline

Chapter 2 of this work presents the fundamental theory of SPDC and employs it to derive expressions which are directly comparable with the experimental results. Chapter 3 introduces our experimental systems, which have been used to measure coincident photon pairs for the first time in a CICESE laboratory, along with the angular distribution of the coincidences. In Chapter 4, our main experimental results are presented and compared with the theoretical predictions. Surpassing our initial objectives, we have performed a detailed study of the temperature dependence of the photon-pair detection, the effects of varying the detected apertures, and a study of crystal poling homogeneity in the PPKTP crystal. The conclusions can be found in the Chapter 5. Additionally, Appendix A presents a characterization of our SPCMs which uses the photon-pairs as a coincidence standard which is used for correcting the observed pair rates. Appendix B presents a study of coincidence-detection by chance with a method for monitoring and accurately removing them. The more detailed set of measurements performed with our system is presented in Appendix C.

Chapter 2. Theoretical preliminaries

In this chapter we present the theoretical elements required to understand the SPDC process, design efficient experiments, and compare the measured results with the theory. Section 2.1 presents a derivation for the quantum state of SPDC light. The derivation begins with electromagnetic theory, and introduces the energy conservation and phase-matching conditions. It involves the use of the canonical quantization process, the interaction picture of quantum mechanics, and the operator solution to the quantum harmonic oscillator. Section 2.2 presents the calculation of the coincidence detection rate using the Glauber second order coherence function, with exact numerical integration of the results. These are, to our knowledge, the first calculations of this kind which employ the correct functional form of the SPDC state. Finally, Section 2.3 presents numerical solutions of the quasi-phase matching conditions which aid in the design of pair-detection experiments.

In the laboratory frame of reference the xz plane is parallel to the optical table with the z axis parallel to the optical axis. The crystal axes are oriented such that the xz crystal-axes plane is parallel to the optical table, with the x crystal axis parallel to the table z axis. As all fields of interest are e-rays, little mention is made of tensor components and birefringency effects.

2.1 Quantum theoretical description of SPDC

2.1.1 The electromagnetic Hamiltonian

The energy content U of a classical electromagnetic field in a dielectric, optical media of volume ΔV is given by [Fox (2006)]

$$U = \frac{1}{2} \iiint_{\Delta V} \left[\mathbf{E} \cdot \mathbf{D} + \frac{1}{\mu_0} \mathbf{B} \cdot \mathbf{B} \right] \mathrm{d}^3 \mathbf{r}, \tag{3}$$

where $\mathbf{E}$ is the electric field, $\mathbf{D}$ is the electric displacement, $\mathbf{B}$ is the magnetic field, and μ_0 is the magnetic permeability of the vacuum. By the process of canonical quantization [Dirac (1930)], the energy function may be used to infer the quantum-mechanical Hamiltonian $\hat{H}$. This process involves expressing the energy function in the classical Hamiltonian

form (in terms of the generalized coordinates q_i and momenta p_i) and replacing the canonical variables with operators defined with appropriate commutation relations. After applying this process to Eq. (3) we have [Mandel and Wolf (1995)]

$$\hat{H} = \frac{1}{2} \iiint_{\Delta V} \left[\hat{\mathbf{E}} \cdot \hat{\mathbf{D}} + \frac{1}{\mu_0} \hat{\mathbf{B}} \cdot \hat{\mathbf{B}} \right] \mathrm{d}^3 \mathbf{r}, \tag{4}$$

where the caret over a symbol denotes an operator.

2.1.2 Material response and nonlinear polarization

The classical electric displacement $\mathbf{D}$ may be written as

$$\mathbf{D} = \epsilon_0 \mathbf{E} + \mathbf{P}, \tag{5}$$

where $\mathbf{P}$ is the polarization density of the medium. For anisotropic, nonlinear optical materials (such as KTP), and neglecting terms of order higher than the second in the electric field E_i, the polarization density allows an expansion of the form

$$\mathbf{P} = \epsilon_0 \left\{ \chi_{ij}^{(1)} E_j + \chi_{ijk}^{(2)} E_j E_k \right\} \mathbf{e}_i \tag{6}$$

$$= \mathbf{P}^{\mathrm{L}} + \mathbf{P}^{\mathrm{NL}}, \tag{7}$$

where E_i is the i-th Cartesian component of $\mathbf{E}$ (corresponding to different polarization directions), $\hat{\mathbf{e}}_i$ are the Cartesian unit vectors, $\chi_{ij}^{(1)}$ is the linear susceptibility, $\chi_{ijk}^{(2)}$ is the second-order susceptibility, and summation over repeated indices is understood. Then the linear and second-order nonlinear contributions to the polarization density are given by $\mathbf{P}^{\mathrm{L}} = \epsilon_0 \chi_{ij}^{(1)} E_j \mathbf{e}_i$ and $\mathbf{P}^{\mathrm{NL}} = \epsilon_0 \chi_{ijk}^{(2)} E_j E_k$, respectively. Equation (4) may be used unchanged for nonlinear media as long as the nonlinear effects are small [Mandel and Wolf (1995)]. Thus, after replacing the field variables by field operators in Eqs. (5) and (7) we have that

$$\hat{H} = \frac{1}{2} \iiint_{\Delta V} \mathrm{d}^3 \mathbf{r} \left\{ \hat{\mathbf{E}} \cdot \hat{\mathbf{E}} + \hat{\mathbf{E}} \cdot \hat{\mathbf{P}}^{\mathrm{L}} + \frac{1}{\mu_0} \hat{\mathbf{B}} \cdot \hat{\mathbf{B}} \right\} + \frac{1}{2} \iiint_{\Delta V} \mathrm{d}^3 \mathbf{r} \left\{ \hat{\mathbf{E}} \cdot \hat{\mathbf{P}}^{\mathrm{NL}} \right\}, \tag{8}$$

where the first integration is associated with linear electromagnetic phenomena and the second integral describes nonlinear effects.

2.1.3   Interaction Hamiltonian for SPDC

Since the field dynamics of linear optics are not of interest in this work, the Hamiltonian may be divided in two contributions relating to the linear dynamics $\hat{H}_0$ and the nonlinear interaction $\hat{H}_I$. By use of the interaction picture of quantum mechanics [Sakurai and Tuan (1985)], the interesting dynamics associated with the interaction Hamiltonian $\hat{H}_I$ may be studied in isolation [Hong *et al.* (1987)].

The experimental system uses a PPKTP crystal pumped with a single frequency laser linearly polarized in the direction of the crystal axis z, which is parallel to the optical table. The three-wave nonlinear interaction is dominated by the χ_{333} component for which all interacting waves are polarized along the crystal z axis. The interaction Hamiltonian is then determined by [Ou *et al.* (1989)]

$$\hat{H}_I = \iiint_{\Delta V} \mathrm{d}^3\mathbf{r} \left\{ \hat{\mathbf{E}} \cdot \hat{\mathbf{P}}^{\mathrm{NL}} \right\} = \iiint_{\Delta V} \mathrm{d}^3\mathbf{r} \left\{ d_{\mathrm{eff}} \hat{E}_p^{(+)} \hat{E}_s^{(-)} \hat{E}_i^{(-)} \right\} + \mathrm{H.C.}, \tag{9}$$

where $d_{\mathrm{eff}} = \frac{\epsilon_0 \chi_{333}^{(2)}}{2}$ is the effective nonlinear coefficient for the three-wave interaction of interest, $\hat{E}_p^{(+)}$ is the positive frequency part of the pump field operator, $\hat{E}_s^{(-)}$ is the negative frequency part of the signal field operator, $\hat{E}_i^{(-)}$ is the negative frequency part for the idler field operator, the vector character of the fields has been neglected, and $\mathrm{H.C.}$ denotes the Hermitian conjugate. The pump laser may be treated classically as long as the nonlinear interaction does not significantly deplete this beam [Mandel and Wolf (1995)]. Following the work of Joobeur, Saleh and Teich [Joobeur *et al.* (1996)], we adopt a Gaussian beam expression, with the pump beam waist within the crystal, of the form

$$E_p(\mathbf{r}, t) = \int \mathrm{d}\omega_p \mathcal{A}(\omega_p) f(\mathbf{r}_\perp) \exp\left[i(k_p(\omega_p)z - \omega_p t) \right] + \mathrm{H.C.}, \tag{10}$$

where $\mathbf{r}_\perp$ are the transverse coordinates xy, $f(\mathbf{r}_\perp)$ is the transverse profile of the pump beam (assumed constant for the length of the crystal), $\mathcal{A}(\omega_p)$ is the spectral profile of the pump beam, k_p is the pump wave number within the crystal, and ω_p is the pump frequency.

The signal quantum field is expanded as a linear combination of plane waves of the form

$$\hat{E}_s \propto \iiint \mathrm{d}^3\mathbf{k}_s \left\{ \hat{a}_{\mathbf{k}_s} \exp\left[i(\mathbf{k}_s \cdot \mathbf{r} - \omega_s(\mathbf{k}_s)t)\right] + \hat{a}_{\mathbf{k}_s}^\dagger \exp\left[-i(\mathbf{k}_s \cdot \mathbf{r} - \omega_s(\mathbf{k}_s)t)\right] \right\}, \qquad (11)$$

where $\hat{a}_{\mathbf{k}_s}^\dagger$ and $\hat{a}_{\mathbf{k}_s}$ are the photon creation and annihilation operators for the signal plane wave mode characterized by wave vector $\mathbf{k}_s$, respectively. The factor with the annihilation operator is that which is associated with the positive frequencies $\hat{E}^{(+)}$. The idler quantum field operator is expanded in the same form.

By substitution of the field expansions from Eqs. (10) and (11) into the interaction Hamiltonian of Eq. (9), we have up to a multiplicative factor

$$\begin{aligned}
\hat{H}_I &= \iiint \mathrm{d}^3\mathbf{k}_s \int_0^\infty \mathrm{d}\omega_p \iiint \mathrm{d}^3\mathbf{k}_i \int_{-L/2}^{L/2} \mathrm{d}z \iint_{-\infty}^\infty \mathrm{d}x\mathrm{d}y \\
&\times \left\{ d_{\text{eff}} \mathcal{A}(\omega_p) f(\mathbf{r}_\perp) \hat{a}_{\mathbf{k}_s}^\dagger \hat{a}_{\mathbf{k}_s}^\dagger e^{i(\omega_s + \omega_i - \omega_p)t} e^{i(\mathbf{k}_p(\omega_p) - \mathbf{k}_s - \mathbf{k}_i) \cdot \mathbf{r}} + \text{H.C.} \right\}, \qquad (12)
\end{aligned}$$

where L is the crystal length, and the limits of integration along the x and y directions have been considered infinite as the size of the crystal face is much larger than the transverse profile of the pump beam. Spatial Fourier transforms can be identified due to the complex exponential function with an $\mathbf{r}$ dependence. The integration along the z axis is a one dimensional Fourier transform of a constant function from $-L/2$ to $L/2$ while the integrations along the x and y directions (parallel to the crystal's entrance face) yield the two-dimensional Fourier transform of the pump beam's transverse profile. Then, after performing the spatial integration we have

$$\begin{aligned}
\hat{H}_I &= \int_0^\infty \mathrm{d}\omega_p \iiint \mathrm{d}^3\mathbf{k}_s \iiint \mathrm{d}^3\mathbf{k}_i \\
&\times \left\{ d_{\text{eff}} \mathcal{A}(\omega_p) \mathcal{F}(\Delta\mathbf{k}_\perp) \operatorname{sinc}\left(\frac{L\Delta k_z}{2}\right) e^{i(\omega_s + \omega_i - \omega_p)t} \hat{a}_{\mathbf{k}_s}^\dagger \hat{a}_{\mathbf{k}_i}^\dagger + \text{H.C.} \right\}, \qquad (13)
\end{aligned}$$

where $\mathcal{F}(\mathbf{k}_\perp)$ is the Fourier transform of the pump beam transverse profile, $\operatorname{sinc}(x) \equiv \sin(x)/x$, Δk_z and $\Delta\mathbf{k}_\perp$ are the projections along the optic axis and the plane transverse to the optic axis, respectively, of the wave vector mismatch $\Delta\mathbf{k}$. The wavevector mismatch,

also known as the phase-mismatch is defined as

$$\Delta \mathbf{k} = \mathbf{k}_p - \mathbf{k}_s - \mathbf{k}_i \tag{14}$$

for interactions along a homogeneous crystal. In our PPKTP crystal, the non-linearity χ_{333} presents sign reversals with a spatial periodicity of $\Lambda = 3.425$ along the crystal x axis, which corresponds to the optical z axis. The spatial dependence of the non-linearity introduces an additional spatial Fourier component into Eq. (12). This does not alter the form of subsequent equations as long as the wavevector phase mismatch is redefined as

$$\Delta \mathbf{k}_{\mathrm{qpm}} = \mathbf{k}_p - \mathbf{k}_s - \mathbf{k}_i - \mathbf{k}_g, \tag{15}$$

where $\mathbf{k}_g = \frac{2\pi}{\Lambda} \mathbf{e}_z$ is the wavevector associated with the crystal poling. The quantity on the left hand side of Eq. (15) is known as the quasi phase-mismatch vector and will be used throughout in the remainder of this thesis as $\Delta \mathbf{k}$.

2.1.4 Time evolution of the system

The initial state of the signal and idler quantum fields is assumed as the vacuum state

$$|\psi(t_0)\rangle = |\mathrm{vac}\rangle_s \otimes |\mathrm{vac}\rangle_i, \tag{16}$$

where t_0 is the initial time, $|\rangle_s$ denotes the state of the signal quantum field, $|\rangle_i$ denotes the state of the idler quantum field, and $\otimes$ is the tensor product (direct product). For notational simplicity we shall omit the tensor product in the following by writing $|\rangle_i \otimes |\rangle_s = |\rangle_i|\rangle_s$. The time evolution of the state $|\psi(t)\rangle$ may be approximated by use of a standard result from first-order time-dependent perturbation theory [Holstein (1992)]

$$|\psi(t \to \infty)\rangle = \left\{ \mathbf{1} - \frac{i}{\hbar} \int_{t_0}^{\infty} \hat{H}_I(t_1) \mathrm{d}t_1 \right\} |\psi(t_0)\rangle, \tag{17}$$

where $\mathbf{1}$ is the identity operator.

2.1.5 The quantum state of SPDC

Upon substitution of Eqs. (13) and (16) into Eq. (17), and considering the limit $t_0 \to -\infty$, we find

$$
\begin{aligned}
|\text{SPDC}\rangle &= |\text{vac}\rangle_s |\text{vac}\rangle_i - \frac{i}{\hbar} \int_{-\infty}^{\infty} \mathrm{d}t \int_0^{\infty} \mathrm{d}\omega_p \iiint \mathrm{d}^3\mathbf{k}_s \iiint \mathrm{d}^3\mathbf{k}_i \\
&\times \left\{ d_{\text{eff}} \mathcal{A}(\omega_p)\mathcal{F}(\Delta\mathbf{k}_\perp)\text{sinc}\left(\frac{L\Delta k_z}{2}\right) e^{i(\omega_s + \omega_i - \omega_p)t}\hat{a}_{\mathbf{k}_s}^\dagger \hat{a}_{\mathbf{k}_i}^\dagger + \text{H.C.} \right\} \\
&\times |\text{vac}\rangle_s |\text{vac}\rangle_i,
\end{aligned}
\tag{18}
$$

which is a steady-state solution for the quantum state of down-converted light.

We will now simplify Eq. (18) by considering that the action of the creation operators on the vacuum state yields a state with a single photon in the signal mode (with wave vector $\mathbf{k}_s$) and a single photon in the idler mode (with wavevector $\mathbf{k}_i$) denoted by $|\mathbf{k}_s\rangle_s|\mathbf{k}_i\rangle_i$. Additionally, the Hermitian conjugate part contains annihilation operators whose action on the vacuum state yields zero [Dirac (1930), Pittman *et al.* (1996)]. Finally, as the complex exponential presents the only time dependence of the integrand, time integration yields the delta function $2\pi\delta(\omega_s + \omega_i - \omega_p)$. This implies a frequency entanglement condition between the signal and idler photons with $\omega_p = \omega_s + \omega_i$ [Joobeur *et al.* (1994)]. The result is then

$$
\begin{aligned}
|\text{SPDC}\rangle &= |\text{vac}\rangle_s |\text{vac}\rangle_i + \frac{2\pi i}{\hbar} \iiint \mathrm{d}^3\mathbf{k}_s \iiint \mathrm{d}^3\mathbf{k}_i \\
&\times \left\{ \int_0^{\infty} \mathrm{d}\omega_p \mathcal{A}(\omega_p)\delta(\omega_s + \omega_i - \omega_p) \right\} \\
&\times \left\{ d_{\text{eff}}\mathcal{F}(\Delta\mathbf{k}_\perp)\text{sinc}\left(\frac{L\Delta k_z}{2}\right) \right\} |\mathbf{k}_s\rangle_s|\mathbf{k}_i\rangle_i.
\end{aligned}
\tag{19}
$$

The pump frequency integration then can be performed immediately and yields $\mathcal{A}(\omega_s + \omega_i)$. Although the vacuum state in Eq. (19) represents physical reality in the SPDC quantum field, it does not contribute to the probability of photo-detection and can thus be disregarded [Pittman *et al.* (1996)]. Then, the state of down-converted light may be written as

$$|\text{SPDC}\rangle = \frac{2\pi i}{\hbar} \iiint \mathrm{d}^3 \mathbf{k}_s \iiint \mathrm{d}^3 \mathbf{k}_i \psi(\mathbf{k}_s, \mathbf{k}_i) |\mathbf{k}_s\rangle_s |\mathbf{k}_i\rangle_i, \tag{20}$$

where the so-called photon pair wave function $\psi(\mathbf{k}_s, \mathbf{k}_i)$ is given by

$$\psi(\mathbf{k}_s, \mathbf{k}_i) = d_{\text{eff}} \mathcal{A}\left(\omega_s(\mathbf{k}_s) + \omega_i(\mathbf{k}_i)\right) \mathcal{F}(\Delta \mathbf{k}_\perp) \text{sinc}\left(\frac{L \Delta k_z}{2}\right). \tag{21}$$

Equations (20) and (21) are the desired expressions for the photon-pair state. Given our experimental conditions we consider $\mathcal{A}(\omega) \propto \exp\left(-(\omega - \omega_p)^2/2\sigma_p^2\right)$, where ω_p is the pump central frequency with bandwidth σ_p (measured as the $1/e$ radius in intensity), and $\mathcal{F}(\Delta \mathbf{k}_\perp) \propto \exp\left(-w_o^2 |\Delta \mathbf{k}|^2/4\right)$, where w_o is the $1/e$ radius in amplitude of the pump beam at its waist. Note that the wave function $\psi(\mathbf{k}_s, \mathbf{k}_i)$ of Eq. (21) cannot be factored into a product of two functions $\psi_s(\mathbf{k}_s) \psi_i(\mathbf{k}_i)$ and is, thus, entangled.

2.2 The rate of coincident photo-detection

2.2.1 Second order coherence function

The instantaneous rate of coincident photo-detection is proportional to the second order coherence function $G_{si}^{(2)}$ [Glauber (1963)] which is formally defined by

$$G_{si}^{(2)} = \langle \psi | \hat{E}_s^{(-)} \hat{E}_i^{(-)} \hat{E}_s^{(+)} \hat{E}_i^{(+)} | \psi \rangle. \tag{22}$$

The direct evaluation of this expression yields a function with temporal structure typically at the picosecond range [Hong and Mandel (1985)]. The response from actual detectors is integrated over a time which is many orders of magnitude larger. After performing a time average, the rate of coincident detection is [Joobeur *et al.* (1996)]

$$G_{si}^{(2)} = \iiint_{\Delta \mathbf{k}_s} \mathrm{d}^3 \mathbf{k}_s \iiint_{\Delta \mathbf{k}_i} \mathrm{d}^3 \mathbf{k}_i \, |\psi(\mathbf{k}_s, \mathbf{k}_i)|^2, \tag{23}$$

where $\Delta \mathbf{k}_s$ and $\Delta \mathbf{k}_i$ are the ranges of wave vectors collected in the signal and idler detectors, respectively. The modes which are coupled into the μ detector, $\mu \in \{s, i\}$, are determined essentially by the μ optical filter, which determines the range of k numbers Δk_μ, and the μ limiting aperture of the optical system, which determines the solid an-

gle $\Delta\mathbf{k}_\perp$ that the detection aperture represents in $\mathbf{k}_\mu$-space. It is interesting to note that Eq. (23), valid for detection with long integration times (> 1 ps), is similar to the usual formulation for the measure of probability in time-independent quantum mechanics [Shankar (1994)].

Substituting the wave function of Eq. (21) into Eq. (23), we have

$$
\begin{aligned}
G_{si}^{(2)} &= d_{\text{eff}}^2 \iiint_{\Delta\mathbf{k}_s} \mathrm{d}^3\mathbf{k}_s \iiint_{\Delta\mathbf{k}_i} \mathrm{d}^3\mathbf{k}_i \\
&\times \ |\mathcal{A}\left(\omega_s(\mathbf{k}_s) + \omega_i(\mathbf{k}_i)\right)|^2 \, |\mathcal{F}(\Delta\mathbf{k}_\perp)|^2 \, \mathrm{sinc}^2\left(\frac{L\Delta k_z}{2}\right) \\
&= d_{\text{eff}}^2 \iiint_{\Delta\mathbf{k}_s} \mathrm{d}^3\mathbf{k}_s \iiint_{\Delta\mathbf{k}_i} \mathrm{d}^3\mathbf{k}_i \\
&\times \ \exp\left(-\frac{(\omega_s + \omega_i - \omega_p)^2}{\sigma_p^2} - \frac{w_o^2|\Delta\mathbf{k}_\perp|^2}{2}\right) \mathrm{sinc}^2\left(\frac{L\Delta k_z}{2}\right).
\end{aligned}
\tag{24}
$$

It is interesting to note that this expression is also useful for the determination of the rate of single photon detection for the signal detection aperture if we let the idler integration range cover the whole $\mathbf{k}_i$-space. The fact that the two k-space integrations of the photon-pair state must be used to obtain the single-photon rate of a detector is a consequence of entanglement and manifests the non-local and non-classical nature of the SPDC field.

Numerous approximations have been used elsewhere in this challenging six-dimensional integral such as assuming a monochromatic and/or plane-wave form for the pump beam to reduce the effective number of integrations. In previous studies, the sinc function of Eq. (24) has been modeled as a Gaussian function [Joobeur *et al.* (1996)] and the integration was then approximated using series expansions of the integrand. These methods are ultimately limited in applicability and rigor. We have performed exact numerical integration of Eq. (24) for the cases of experimental interest, which will be described next.

2.2.2 Numerical integration of the pair rate

In order to perform the multidimensional integral of Eq. (24), we implemented a Monte Carlo probabilistic integrator. The Monte Carlo estimator for the integral $I = \int_\Omega f(\mathbf{x})\mathrm{d}^n\mathbf{x}$ is

given by [Fishman (1996)]

$$I = \frac{V}{N} \sum_{j}^{N} f(\mathbf{x}_j),$$ (25)

where $V = \int_{\Omega} \mathrm{d}^n \mathbf{x}$ is the hyper-volume associated with the domain of integration Ω, $\mathbf{x}_j$ ($j \in \{1, 2, \ldots, N\}$) are independent and identically distributed random vectors with uniform probability density function $\rho'(\mathbf{x}) = 1/V$, and N is the number of random samples taken for the estimation. Direct application of this expression for our integration of interest yields

$$I = \frac{V}{N} \sum_{j}^{N} \exp\left(-\frac{\Delta\omega^2(\mathbf{k}_{sj}, \mathbf{k}_{ij})}{\sigma_p^2} - \frac{w_o^2|\Delta\mathbf{k}_\perp(\mathbf{k}_{sj}, \mathbf{k}_{ij})|^2}{2}\right) \mathrm{sinc}^2\left(\frac{L\Delta k_z(\mathbf{k}_{sj}, \mathbf{k}_{ij})}{2}\right),$$ (26)

where the random samples $\mathbf{k}_{sj}$ and $\mathbf{k}_{sj}$ are uniformly distributed over $\Delta\mathbf{k}_s$ and $\Delta\mathbf{k}_i$ (as defined in Eq. (24)), respectively, and $\Delta\omega = \omega_s + \omega_i - \omega_p$. In the limit of $N \to \infty$, this equation can be interpreted as the average value of the integrand over the integration domain $\langle f \rangle$ times the measure (hyper-volume) of the integration domain $I = V\langle f \rangle$.

Evaluation of Eq. (26) for our experimental conditions requires an impractical number of functional evaluations. Specifically, in the integrations with the largest domain considered, convergence was achieved with $N \approx 1 \times 10^8$, which required over 20 hours of computer time for the calculation of an experimentally comparable result. Because the detected bandwidth is $\sim$100 times larger than the pump laser bandwidth, which is 20 pm, then the contribution to the estimator approaches zero for most of the evaluated samples, since $|\Delta\omega(\mathbf{k}_{sj} - \mathbf{k}_{ij})| >> \sigma_p$. In effect, the production of samples for which the integrand is significant is a rare event (one with small probability), and this drastically reduces the effectiveness of the estimator as presented [Denny (2001)]. The convergence of the estimator can be improved by the importance sampling Monte Carlo method, for which the estimator is given by [Rubinstein and Kroese (2011)]

$$I = \frac{1}{N} \sum_{j}^{N} \frac{f(\mathbf{x}_j)}{\rho(\mathbf{x}_j)},$$ (27)

where the random vectors $\mathbf{x}_j$ are sampled from a general probability density function $\rho(\mathbf{x})$. The convergence rate of this estimator depends critically on the chosen distribu-

tion ρ. In fact, Eq. (27) reduces to the usual Monte Carlo method of Eq. (26) in the case $\rho(\mathbf{x}) = \rho'(\mathbf{x}) = 1/V$. Intuitively, the importance sampling method works by drawing random samples from the regions where the integrand is more likely to be significant, and then adjusting the average with appropriate weighting.

The pump spectral profile is now approximated in terms of wave numbers by writing

$$\exp\left(\frac{-(\omega_s + \omega_i - \omega_p)^2}{\sigma_p^2}\right) \approx \exp\left(\frac{-(k_s + k_i - k_p)^2}{(\sigma_p^k)^2}\right), \tag{28}$$

where the expression $\sigma_p^k \approx n\sigma_p/c$ is the (wave number) spectral width. By considering the probability density $\rho(\mathbf{k}_s, \mathbf{k_i}) = \rho_s(\mathbf{k}_s)\rho_i(\mathbf{k}_i|\mathbf{k}_s)$ where ρ_s is a uniform distribution and $\rho_i(\mathbf{k}_i|\mathbf{k}_s) = C(k_s)\exp\left(\frac{-(k_i + k_s - k_p)^2}{(\sigma_p^k)^2}\right)$ is a conditional density with respect to $k_s = |\mathbf{k}_s|$ (which is uniform in its other degrees of freedom), and $C(k_s)$ is a normalization factor, we have

$$
\begin{aligned}
I &= \frac{1}{N}\sum_i^N \exp\left(-\frac{w_0^2|\Delta\mathbf{k}(\mathbf{k}_{sj}, \mathbf{k}_{ij})|^2}{2}\right) \\
&\times \operatorname{sinc}^2\left(\frac{L\Delta k_z(\mathbf{k}_{sj}, \mathbf{k}_{ij})}{2}\right) \frac{\exp\left(\frac{-(k_s + k_i - k_p)^2}{(\sigma_p^k)^2}\right)}{\rho(\mathbf{k}_{sj}, \mathbf{k}_{ij}))}.
\end{aligned}
\tag{29}
$$

This expression converges approximately 100 times faster than Eq. (26) and only requires a Gaussian random number generator in addition to the generator of uniform samples. All of the numerical results of this thesis have been calculated with this estimator using $N = 4 \times 10^6$ samples; they are presented in comparison with the experimental results in Section 4.2.

In summary, the present approach has considered the frequency entanglement condition for the generation of random samples. The generation of the samples then occurs conditionally, according to a nonuniform probability density which efficiently covers the important regions the integration domain. The importance of the region is considered in terms of the performance of the estimator as measured by the convergence rate. We note that the convergence rate can be further improved by considering the quasi-phase-matching condition in the distribution of the random samples.

2.3 The quasi phase-matching condition

Quasi phase-mismatch from Eq. (15) is known from classical optics to be required for efficient nonlinear interactions in a periodically poled crystal [Fejer *et al.* (1992)]. In our case we can see that the integrand in Eq. (24) is maximized when $\Delta \mathbf{k} = 0$ and $\omega_s + \omega_i = \omega_p$, so the photon pairs are expected to be found near these conditions. Considering the degenerate case where $\lambda_s = \lambda_i$, the quasi phase-mismatch can be cast into the form

$$\Delta \mathbf{k} = 2\pi \left\{ \frac{n_z(\lambda_p)}{\lambda_p} \mathbf{e}_z - \frac{1}{\Lambda} \mathbf{e}_z - \frac{n_z(\lambda_s)}{\lambda_s} \left(\mathbf{e}_s + \mathbf{e}_i \right), \right\} \tag{30}$$

where $\mathbf{e}_s$ and $\mathbf{e}_i$ are the emission directions of the signal and idler photons, internal to the crystal (assumed to lie in the zx plane), and the wave vectors associated with the pump beam and the periodic poling are both assumed to be in a direction parallel to the z axis. The projection along the x axis yields the transverse quasi phase-mismatch equation

$$\frac{\Delta k_x}{2\pi} = -\frac{n_z(\lambda_s)}{\lambda_s} \left(\sin(\theta_i') + \sin(\theta_s') \right), \tag{31}$$

where the primed polar angular variables θ' are internal to the crystal. From Snell's law, the external angle is calculated by the relationship $\theta_s = n_z(\lambda_s)\theta_s' \approx (1.8445)\theta_s$ within the small angle approximation. It can be seen immediately that, for the case of degenerate SPDC, exact transverse phase-matching ($\Delta \mathbf{k}_\perp = 0$) is attained with both observation points at exactly opposite polar angles $\theta_s = -\theta_i$. Taking the projection of this equation along the z axis and assuming the perfect transverse quasi phase-matching condition $\Delta k_z = 0$, we have the longitudinal quasi phase-mismatch equation

$$\frac{\Delta k_z}{2\pi} = \frac{2}{\lambda_s} \left\{ n_z(\lambda_s/2) - n_z(\lambda_s) \cos(\theta_s') \right\} - \frac{1}{\Lambda}, \tag{32}$$

where the substitution $\lambda_p = \lambda_s/2$ has been made and the primed polar angular variables $\theta\prime$ are internal to the crystal. This expression can be solved analytically to give the phase-matching angle for observation of frequency-degenerate photon pairs as

$$\theta_{s,i}' = \cos^{-1}\left(\frac{n_z(\lambda_s/2) - \frac{\lambda_s}{2\Lambda}}{n_z(\lambda_s)} \right). \tag{33}$$

The more general case which considers an inclination angle θ_g between the poling normal and the optic z axis, and non-degenerate signal and idler wavelengths $\lambda_s = r\lambda_i$ (which implies $\lambda_s = (1+r)\lambda_p$) has been similarly solved and yields the condition

$$\frac{n_z(\lambda_p)\cos(\theta'_s)}{\lambda_p} - \frac{\cos(\theta_g - \theta'_s)}{\Lambda} = \frac{\lambda_s \left(\frac{n_z^2(\lambda_p)}{\lambda_p^2} + \frac{n_z^2(\lambda_s)}{\lambda_s^2} - \frac{r^2 n_z^2(\lambda_s/r)}{\lambda_s^2} + \frac{1}{\Lambda^2} - 2\frac{n_z(\lambda_p)}{\Lambda\lambda_p}\cos(\theta_g) \right)}{2n_z(\lambda_s)}, \quad (34)$$

which can be solved numerically for θ_s. The corresponding idler polar angle θ_i is given by

$$\theta_i = \mathrm{asin}\left(-\frac{\lambda_s \sin(\theta_g)}{\Lambda r n_z(\lambda_s/r)} - \frac{n_z(\lambda_s)\sin(\theta_s)}{r n_z(\lambda_s/r)} \right). \quad (35)$$

2.3.1 Temperature dependent tuning curves

The wavelength and temperature dependent refractive index $n_z(\lambda, T)$ [Fradkin *et al.* (1999), Emanueli and Arie (2003)] was introduced into Eqs. (33) and (34). Solutions were found as a function of crystal temperature T for three cases. The first case considers the degenerate wavelengths $\lambda_s = \lambda_b = 812.236$ nm, and is shown in Fig. 1. The second case is a non-degenerate photon pairs for which $\lambda_s = \left(\frac{10}{9}\right)\lambda_i = 857.36$ nm, which is shown in Fig. 2. The third case considers a strongly non-degenerate pair for which $\lambda_s = \left(\frac{6}{5}\right)\lambda_i = 893.45$ nm, which is shown in Fig. 3. We have used $\lambda_p = 406.118$ nm, $\Lambda' = 3436$ nm, and $\theta_g = 0$ for all cases. The assumed periodicity of the poling Λ' is chosen such that collinear phase-matching occurs at $T = 65°$C; as was experimentally observed with our pump-crystal system [Romero Sánchez (2013)], the actual poling period in the PPKTP is $\Lambda = 3425$ nm.

As can be seen, for any given angle of observation, the degenerate SPDC light ($\lambda_s = 812.236$ nm) achieves the phase-matching condition at a lower temperature than any of the non-degenerate pairs. Thus, collinear phase-matching of non-degenerate pairs requires temperatures greater than $T = 65°$C. For observation of degenerate photon pairs at angles between $\theta = 1°$ and $\theta = 3°$, the crystal temperature must be set to the range $35°$C $< T < 60°$C. For non-degenerate pairs, the pair member with the longer wavelength (here considered as the signal) is emitted at a larger polar angle, and the difference in signal and idler polar angle of emission increases for the more strongly non-degenerate pairs.
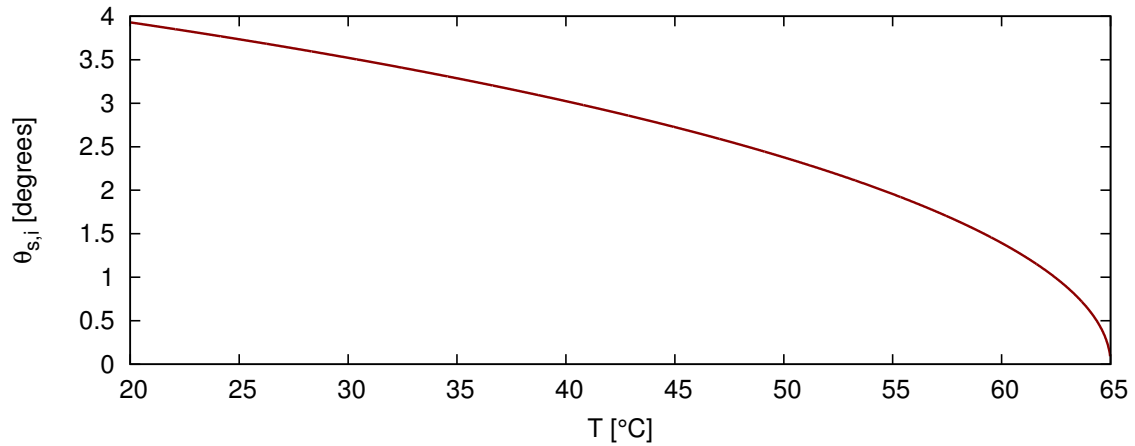
Figure 1: Quasi phase-matching signal and idler polar angles $\theta_{s,i}$ as a function of crystal temperature T for $\lambda_s = \lambda_i$. In this degenerate interaction the signal and idler angles are identical.
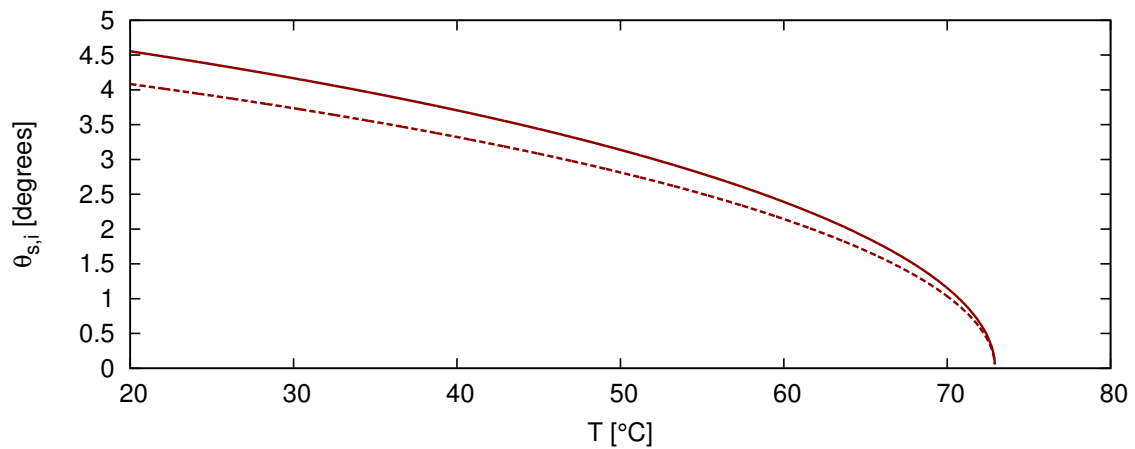
Figure 2: Quasi phase-matching signal (solid line) and idler (dashed line) polar angles $\theta_{s,i}$ as a function of crystal temperature T for $\lambda_s = (10/9)\lambda_i$.
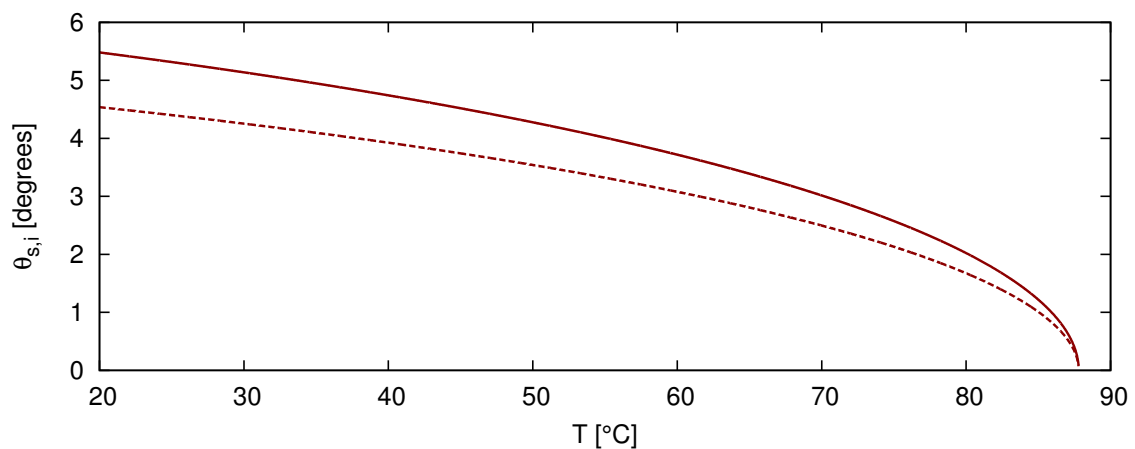
Figure 3: Quasi phase-matching signal (solid line) and idler (dashed line) polar angles $\theta_{s,i}$ as a function of crystal temperature T for $\lambda_s = (6/5)\lambda_i$.
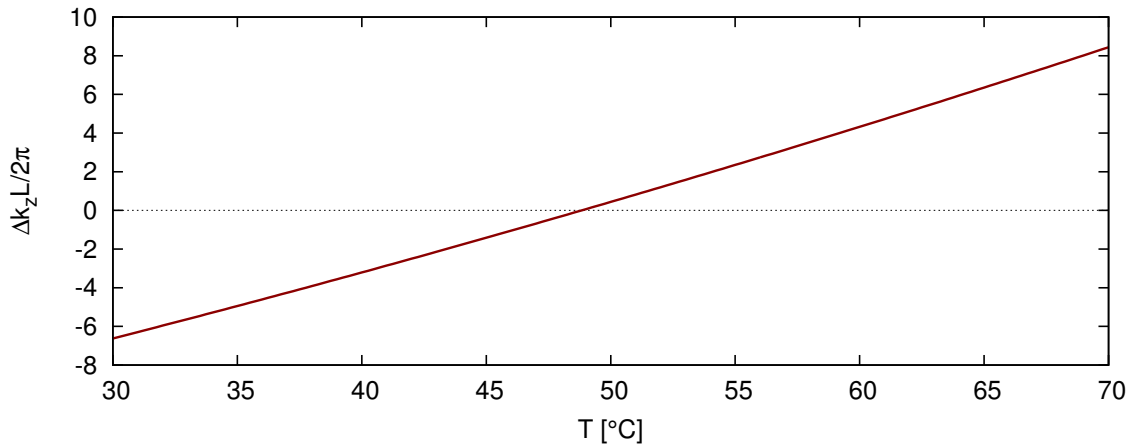
Figure 4: $\Delta k_z L/2\pi$ as a function of crystal temperature T for degenerate photon pairs $\lambda_s = \lambda_i$ at $\theta_{s,i} = 2.5°$C.

It can be seen, from Eqs. (23) and (24), that for the case of equal signal and idler polar angles $\theta_{s,i} = 2.5°$ with degenerate frequencies $\omega_s = \omega_i$, the photon pair wave function is proportional to the phase-matching function, or $\psi = d_{\text{eff}}\text{sinc}\left(\frac{L\Delta k_z}{2}\right)$. Thus, the rationalized argument of the sinc function $\frac{\Delta k_z L}{2\pi}$ is a quantity of experimental interest. This quantity has been calculated as a function of crystal temperature T, and the result is shown in Fig. 4. The monotonic dependence of the longitudinal phase-mismatch indicates that crystal temperature scans can be used to map the phase-matching function, as has been shown in other works using second harmonic generation in PPTKP [Wang *et al.* (1999)].

Chapter 3.   Experimental method

In this chapter, we present the design and construction of two closely-related experiments which were performed in the quantum optics laboratory at CICESE. In particular, single-photon counting modules (SPCMs) have been used to detect the non-local correlation of the field in the form of coincident photon-pair detection from an SPDC source.

The two experiments share the same general layout presented in Section 3.1 and are primarily distinguished by the geometry of the fiber coupling method. In the first experiment, described in Subsection 3.4.1, the light is coupled simply by placing the prepared fiber tips in free space at carefully selected angular positions pointed towards the source, thus serving as a quasi-point detector. In the second experiment, which is described in Section 3.4.2, a lens and iris were installed in front of each fiber providing higher signal levels and allowing control of angular integration.

The optical system that was used is composed of three parts: the pump system, the PPKTP crystal, and the fiber-coupling system. The pump system is described in Section 3.2. Its most important characteristic is that the pump laser runs in single-frequency mode, providing a beam with a narrow bandwidth. Section 3.3 describes both the PPKTP nonlinear crystal and the optical mount in which it is housed. This mount incorporates a temperature controlled oven and a translation stage for accurate transverse positioning of the crystal. The fiber-coupling systems are described in Section 3.4.

A brief description of the the single-photon counting modules (SPCMs) that were used in these experiments is found on Section 3.4.4. The main discussion regarding the SPCMs has been deferred to Appendix A. Appendix A includes a detailed characterization of the detectors' counting and timing resolution that exploits the close synchronization of the photon-pairs and marks one of the applications that have been explored in our work.

The electronic part of the system is comprised of a set of NIM electronic modules which are described in Section 3.5 and a computer system for interfacing and automation of data collection which is described in Section 3.6. The system allows for real-time monitoring of randomly-coincident detection events, which permits an accurate removal of these so-called *accidentals*.
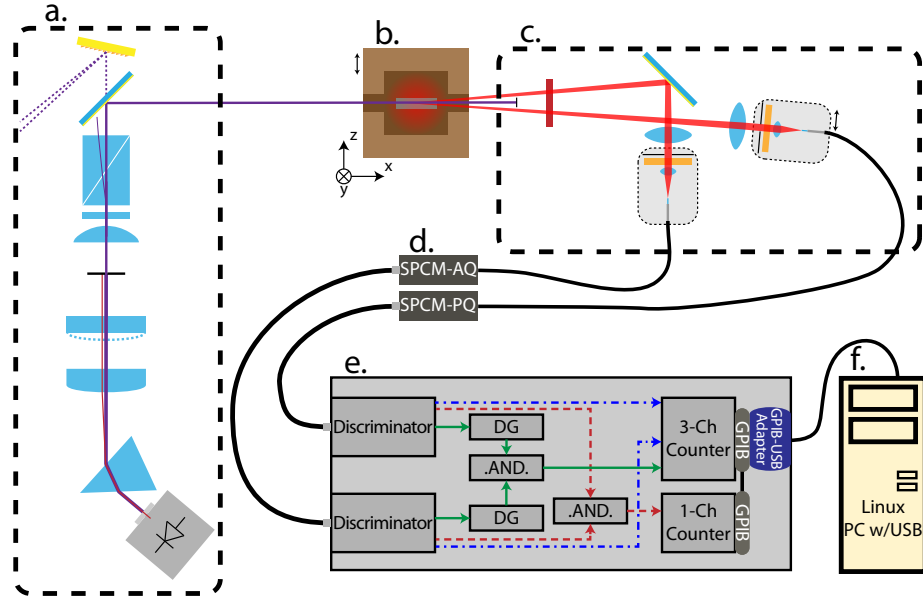
Figure 5: Experimental arrangement for the photon-pair detection experiments.

A theoretical model for the accidentals is described in detail in Appendix B. The results from this theory are compared with experimental data. Furthermore, results from the accidental correction system are presented.

All of these experiments have been performed in the configuration we refer to as near-degenerate quasi-phase-matching by means of narrow interference filters centered at the degeneracy frequency (in which $\omega_s \approx \omega_i$). The specific characteristics of the filters will be discussed in Subsection 3.4.3, but it is sufficient for now to mention that their non-negligible transmission bandwidths introduce a small effect due to frequency integration as will be seen from numerical calculations, to be presented in Chapter 4.

3.1 Schematic for coincident pair detection experiments

The general layout of the experiments for coincident photon-pair detection is shown in Fig. 5. It is seen that the experiment is made up of five main parts:

a. Temperature and current stabilized single-frequency pump laser ($\lambda_p = 406.118$ nm) with attenuator ($P_{\max} = 22$ mW).

b. Periodically-poled KTP nonlinear crystal (PPKTP) with a poling period of $\Lambda = 3.425$
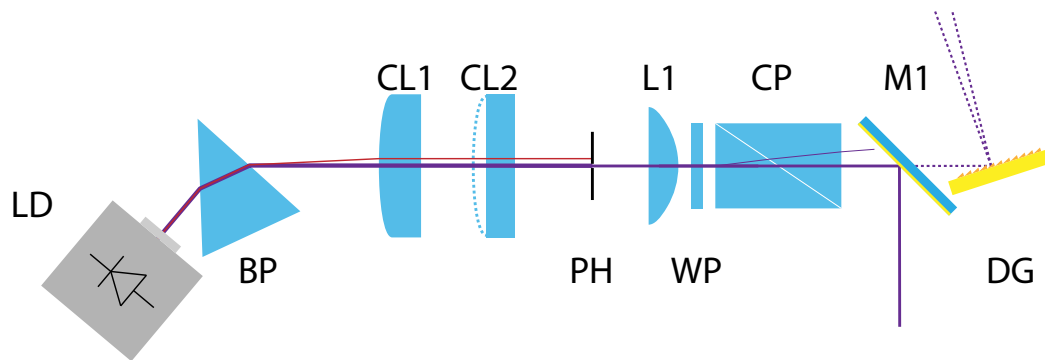
Figure 6: Schematic for the pump laser system.

μm in temperature-stabilized oven.

c. Two optical fiber-coupling systems.

d. Two Single Photon Counting Modules, with different characteristics (see Appendix A for details).

e. Electronic pulse processing for photon coincidence detection and rate measurement.

f. Computer control and automated data acquisition through GPIB interface and software.

Figure 5 also shows the fiber coupling system (c) which corresponds to the experiment with collection optics. The experiment with free-space fiber coupling replaces this with the system described in Subsection 3.4.1.

3.2 Single-frequency source of pump photons

Our pump beam is part of a previously-developed photon-pair system [Romero Sánchez (2013)] that was modified to include an attenuator and to easily allow for monitoring of spectral characteristics of the output beam. The design can be seen in Fig. 6 which includes the following components:

LD. Ondax single-frequency laser diode ($P_o \approx 30$ mW, $\lambda_o = 406.118$ nm, $\Delta\lambda \approx 0.07$ nm).

BP. Dispersive Brewster prism.

CL. (1 & 2) Cylindrical lenses used for correcting the ellipticity in the source's output mode and to focus the beam on the spatial-mode filter.

PH. Pinhole for spatial-mode filtering (50μm).

L1. Positive lens for weak focusing on crystal (f=100 mm).

WP. Zero-order half-wave plate mounted on a rotation stage.

CP. MgF_2 Rochon crystal polarizer.

M1. Dielectric mirror in flipping mount.

DG. Diffraction grating for pump-beam spectral analysis (out of main path).

The Ondax laser diode is wavelength stabilized and is controlled with a Stanford Research Systems LDC501 (not shown on diagram) at a constant current of 66.03 mA and working temperatures spanning $22°$C to $27°$C. An alternative optical path is available by flipping the mirror (M1) out of the optical path. In this configuration the beam is incident on a diffraction grating. The second diffracted order is observed on a screen. The working temperature must then be carefully selected to achieve actual single-mode operation.

The wavelength of the laser is temperature dependent. The mode of operation usually jumps to a neighboring mode when a change in temperature of $\sim 1°$C is introduced. The device may also work as a two-mode source by careful selection of the working temperature. In addition, we have seen that the emission bandwidth varies for different laser operation modes.

The source can provide a maximum power or 22 mW after the mirror (M1). A crystal polarizer and half-wave plate are used to attenuate the output. The attenuation would prove indispensable in the experimental determination of accurate correction factors for photon-pair detection.

Using the knife-edge method [Khosrofian and Garetz (1983)], we measured the beam waist in the x and y directions, corresponding to scans that were parallel and perpendicular to the optical table, respectively. The results are shown on Fig. 7. The $1/e$ radius in
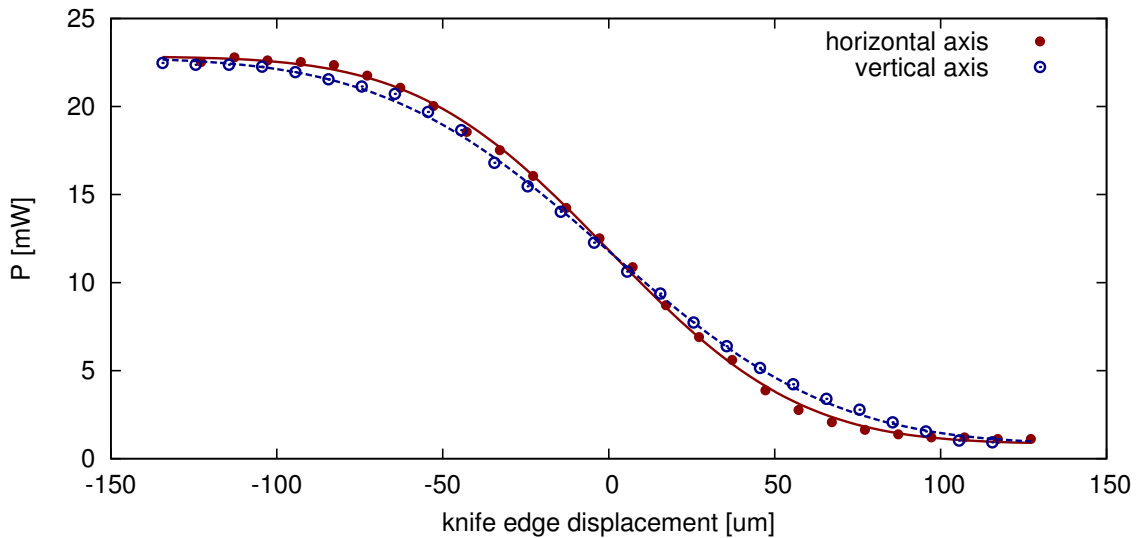
Figure 7: Transmitted power of the pump beam as a function of knife-edge position. The continuous lines are error function fits. The good agreement indicates that the transverse profile is mostly in fundamental Gaussian mode.

intensity (averaged over the two directions) was found to be $\hat{r} = 69.72 \mu$m and a ratio $\frac{r_x}{r_y} = 0.85$. Given the near-circular symmetry that was found, we ignore the ellipticity in what follows.

3.3 Oven-mount, temperature controls and the PPKTP crystal

The nonlinear crystal is a 5 mm long piece of PPKTP cut for propagation along the x axis and is periodically poled with a poling period of $\Lambda \approx 3.425$ μm. It is mounted in a temperature-stabilized oven which is controlled with a Thor Labs TC200 temperature controller (not depicted in the diagram). The crystal axes are oriented such that the xz plane is parallel to the optical table. The entrance face of the crystal is 1 mm across the z axis and 1.5 mm across the y axis.

As has been shown in Section 2.3.1, quasi-phase-matching in PPKTP is highly dependent on crystal temperature. The experimental study of this temperature dependence represents one of the main results of this work.

The oven is shown on Fig. 8. There are two openings on opposing sides at the height of the crystal which are used as entrance and output apertures. The oven is mounted on a stage with two degrees of freedom for angular positioning. This control is useful in minimizing back-reflections which may destabilize the laser. Adjusting the position of
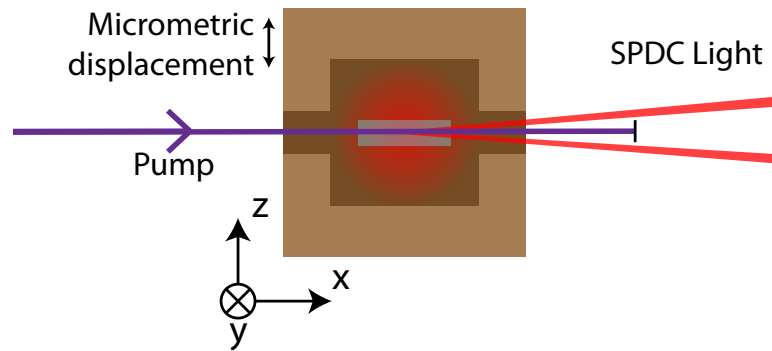
Figure 8: Diagram of oven mount for the PPKTP crystal. The oven is depicted without its top cover and the axes shown are those of the crystal.

the oven along the optical axis is a simple task, requiring only minimal re-alignment. A micrometer enables fine positioning along the crystal's z axis.

3.4 Optical systems for SPDC coupling into optical fibers

We will describe two optical systems which are intended to couple the photon pairs into optical fibers. The first coupling system is part of an experiment known as *Mark One* or Mk-I. This experiment serves as a *proof of concept* in which a relatively simple system is used to demonstrate the detection of coincident photon-pairs. This experiment yielded measurements of correlation angle and temperature tolerance of the distribution of pair detection. The second coupling system is part of our main experiment, called *Mark Two* or Mk-II, which improves on the first experiment achieving higher signal levels. This is made possible by collecting a solid angle of SPDC flux into the optical fibers with a lens and iris system in each of the two detection channels. These correspond to the signal and idler photons. We have used multimode fibers with 50μm core diameters that are protected from stray light by an opaque cover throughout their lengths.

In both systems, the output aperture of the oven is followed by a beam block which has been installed to prevent the pump beam from propagating along the optical axis of the system while transmitting the photon pairs which emerge at an angle of over $0.25°$. This is followed in turn by an RG665 glass filter which removes any stray light from the pump while transmitting about 80% of the IR light containing the photon-pairs.

It is important to note that these systems are aligned at a particular polar phase-
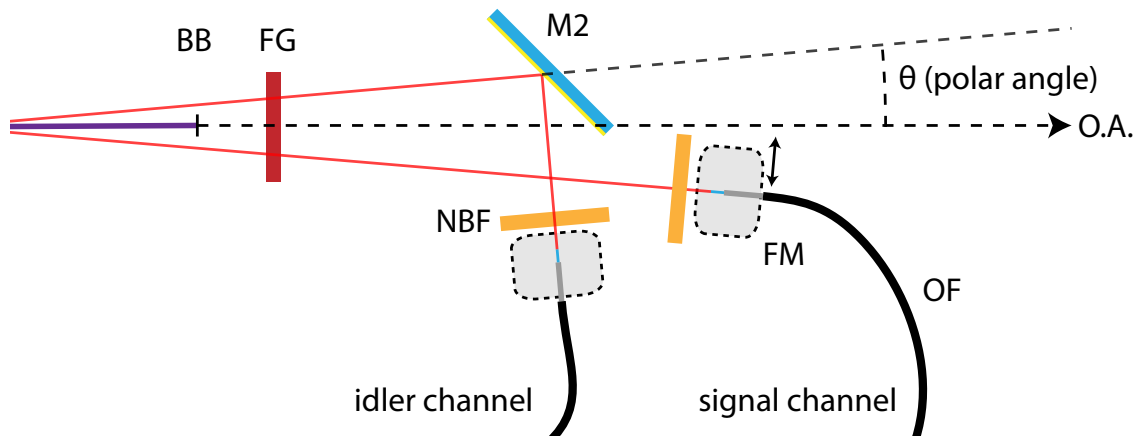
Figure 9: Schematic of the optical arrangement for free-space fiber coupling. The two channels are identical in capabilities and components, repeated components are listed only once.

matching angle and the use of a different angle requires the re-positioning and realignment of the fiber mounts as well as temperature tuning of the crystal. The crystal dimensions allow for unobstructed observations at polar angles of up to $10°$.

3.4.1 Free-Space fiber coupling

The case of free space fiber coupling has a simple diagram for the optical system as seen in Fig. 9. Narrow-bandwidth filters are placed in front of the fiber tips, which are held in place using optical fiber mounts which allow for moving the transverse position of the fiber. The idler path is reflected by a flat silver mirror for reasons of space. The fibers are placed at opposing sides of the SPDC emission ring which has its center on the optical axis. The fiber tips are pointing directly towards the crystal.

The experiment was first built with a distance from the crystal to the fiber tips of 30cm. This was reduced to a 15cm distance in each arm after some early experiments showed that any improvement of signal levels would help in finding time correlated photon-pairs. After aligning the system with this improved design, we were able to measure a rate of 19 photon-pairs per second in what was the first observation of photon-pairs by coincidence detection made in CICESE (on the 24th of November, 2013).
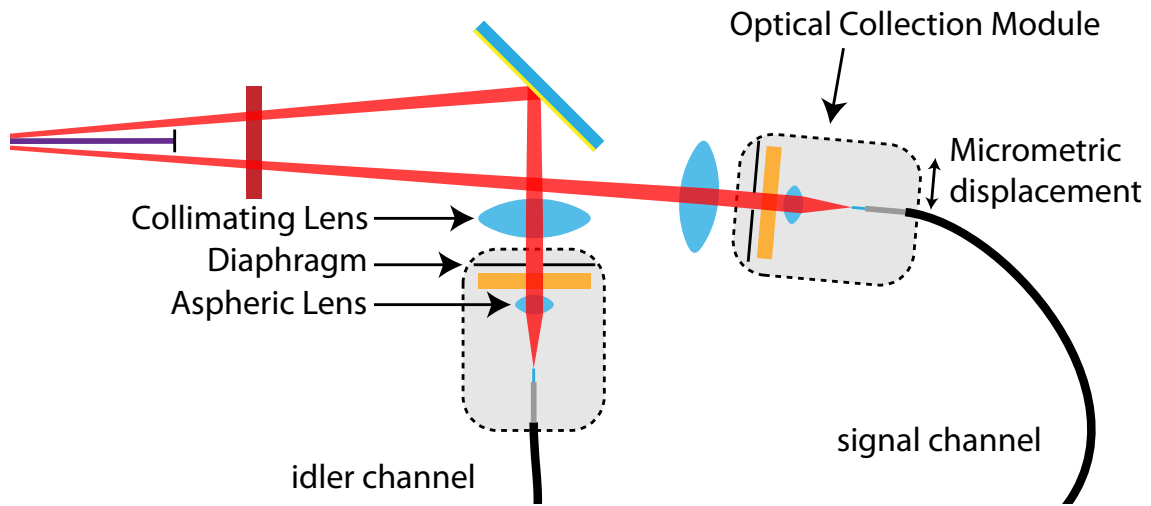
Figure 10: Schematic of the optical arrangement for fiber coupling through a collection-optics system. The two channels differ only in the lack of a translation stage on the idler channel. Those components already present on figure 9 are not labeled here.

3.4.2   Fiber coupling with collection optics

An iris and lens were introduced in each of the detection paths along with the narrow-band filters as shown in Fig. 10. The signal channel's optical collection module (OCM) was mounted on a linear translation stage that is positioned with a micrometer. This module holds the fiber mount for accurate fiber tip positioning, an aspherical lens used for efficient focusing of the light on the fiber, a narrow-band filter, and a diaphragm that is the limiting aperture. A lens in front of the OCM collimates the SPDC flux from the crystal. The OCM on the idler channel is similar, but has no translation stage.

The distance from the crystal to the collimating lens is 50 cm. The aspherical lens' clear aperture is 5 mm. This is the system's maximum aperture and implies an acceptance polar angle of $\Delta\theta = 0.57°$. The diaphragm allows adjustment of the angle to as little as $\Delta\theta = 0.03°$.

Alignment of the optical system represents a challenge as the photon pairs to be coupled into the optical fibers are in the infrared spectral region and are emitted with a total power of a only few nW over a wide spectral and angular range (the collected power per detector is, for all of our experiments, under 1 pW). To align both of the modules a tracer

beam was employed. This beam was from a Helium-Neon laser with a power output of a few mW. The beam was expanded and focused on the center of the crystal such that its divergence angle matched that of the actual photon pairs. The optical fibers were then disconnected from the SPCM modules and the alignment was achieved by adjusting the fiber position while visually monitoring the fiber output at the connector end with maximum aperture setting. As coupling was found, the aperture was closed in steps, correcting the fiber positioning in all three axes at each step. To test the alignment of the photon pairs, the tracer beam was then removed from the optical path with the flip-out mirror mounts.

A correction of 0.2 mm was introduced to the longitudinal position of the fiber tip. The correction was calculated as the difference in focal lengths of the aspherical lenses at the wavelengths $\lambda_{\mathrm{HeNe}} = 633$ nm and $\lambda_{\mathrm{Pairs}} \approx 812$ nm due to chromatic dispersion. The SPDC signal was observable immediately after this longitudinal correction was introduced. Fine transverse position adjustment (on the order of the fiber core width) was introduced to achieve optimal coupling conditions.

The use of large apertures and high levels of pump power produces single photon counting rates over 500,000 photons/s in our most sensitive detector and over 250,000 photons/s in the other, with pair rates over 60,000 pairs/s. Since such levels of photon flux are known to produce a saturation effect, we have made efforts to understand and to correct the behavior of these detectors. This discussion is presented in Appendix A.

3.4.2.1 Polar angle control (signal channel)

The fiber mount and coupling optical elements of the signal channel are mounted on a linear translation stage that allows for transverse motion in the plane of detection. In our geometry, this amounts to scanning the polar angle of detection θ. Fine control is essential when placing two detectors at exactly opposite polar angles with respect to the optic axis.

The translation stage is fitted with a micrometer having a range of 25 mm and a resolution of 10 μm which, at a working distance of 50 cm, correspond to a polar angular span of $2.8°$ and resolution of $0.001°$. A spacing of $0.01°$ was most commonly used for the sampling interval in the angular scans. The useful angular range is limited by the area of the collimating lens and the diaphragm setting. At maximum aperture, the range of angles
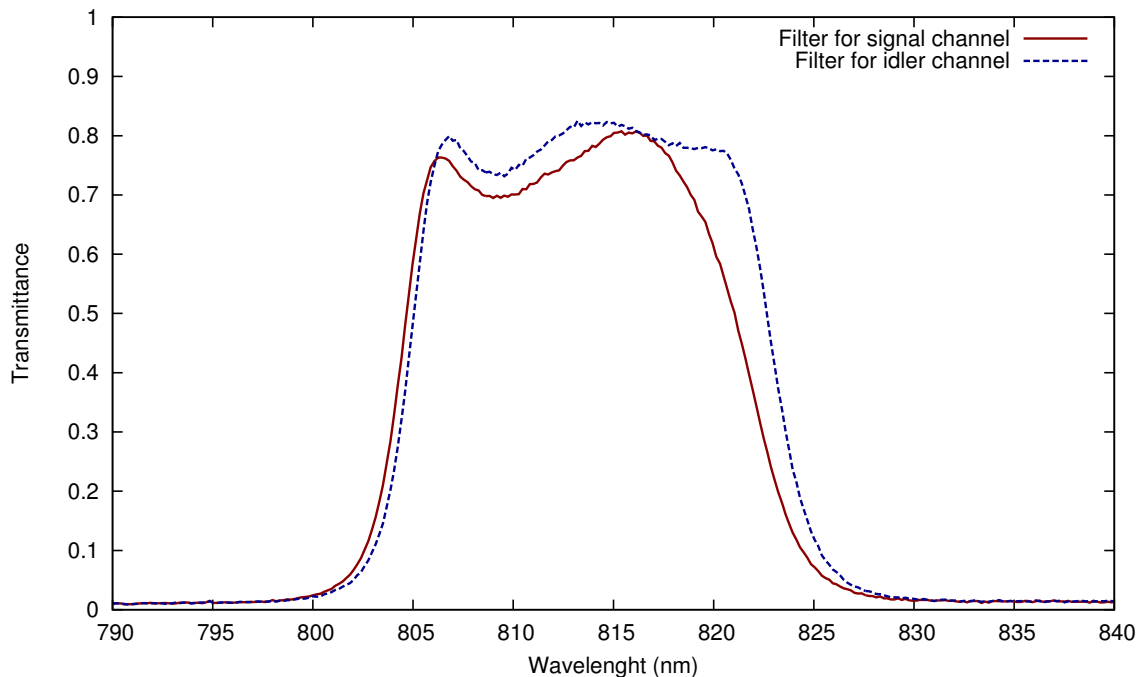
Figure 11: Transmission spectra for the narrow-band interference filters used in the photon-pair detection experiments. The transmission band is centered at the degenerate wavelength $\lambda_\mathrm{s} = \lambda_\mathrm{i} = 812$ nm.

that may be used is approximately $1.8°$.

3.4.3 Bandwidth and quasi-degeneracy

Our experiments study the quasi-degenerate regime of SPDC. This regime is defined by the condition $\omega_s \approx \omega_i$. This is achieved with narrow-band interference filters centered about the degeneracy frequency.

In order to characterize the filters, we measured their transmission spectra with a tungsten source and an Ocean Optics USB spectrometer. The resulting transmission plots can be seen in Fig. 11. The transmission band of the signal path is 17.4 nm wide (FWHM) and centered at 813nm. The transmission band for the idler path is 18.4 nm wide and is centered at 813.8 nm. The degenerate pairs have a wavelength of 812.236 nm, which is transmitted with efficiencies of 75% and 80% by the signal and idler filters, respectively.

The most strongly non-degenerate pairs which are transmitted efficiently ($\lambda_s = 804$ nm and $\lambda_i = 820$ nm) have a frequency (or energy) ratio that is 2% away from unity. Given that experiments are tuned for quasi-degenerate photon pairs, our experimental design

is highly symmetrical in both the signal and idler paths, aside from mirrors and mounting differences.

3.4.4   Available SPCMs

We have employed two SPCMs that have somewhat different designs. One of them has passive quenching (EG&G SPCM-200-PQ-F450, hereafter referred to as PQ) while the other has active quenching (Perkin-Elmer SPCM-AQR-13-FC, referred to as AQ). These are well-suited for detection around 812 nm as their efficiencies are about 30% and 15%, respectively, for the AQ and PQ detectors.

The differences between these two detectors go far beyond their quantum efficiencies. PQ detectors are known to present saturation effects which are observable in the timing resolution of the pulses with counting rates as low as 100,000 photons/s, while the AQ detectors behave well at count rates up to 5×10^6 (at the cost of some additional jitter and a delay at the output, of about 25 ns, at all count rates when compared to the best PQ detectors). The dark count performance also differs and is below 150 s^{-1} for the AQ detector and below 450 s^{-1} for the PQ detector. This is not significant in coincidence detection and produces negligible effects as shall be seen when discussing the effect of randomly coincident pulses.

A detailed characterization of the SPCMs was performed using the photon-pairs and is presented in Appendix A. This work provided valuable information regarding the counting linearity and timing accuracy, thus exposing the main differences of the two devices.

3.5   Electronics for pulse counting and coincident-pair discrimination

The processing of the pulses produced by the SPCMs occurs in electronic modules that follow the NIM (National Instrumentation Modules) standard. This modular system provides all of the facilities required for fast pulse logic, pulse counting, and computer interfacing. The design went through several revisions after which we settled on the configuration shown in Fig. 12. This system has a large degree of symmetry and flexibility for testing at internal points of the signal path.
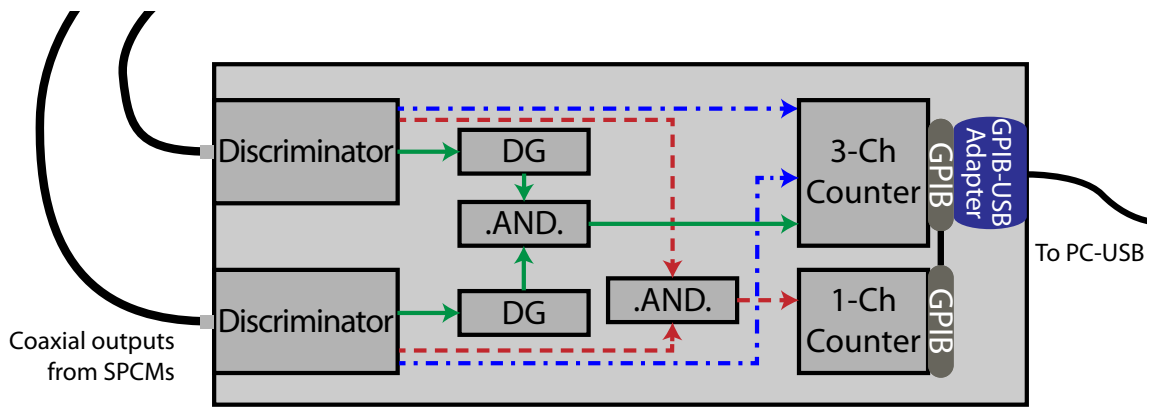
Figure 12: Schematic for the electronic coincidence detection and counting system. The blue paths (dot-dashed) represent the single-photon counts from the signal and idler channels. The green paths (solid) are used for synchronized coincidence detection while the red paths (dashed) are used for desynchronized coincidence detection.

Five NIM modules are used in our experiment, along with a computer interface, these are:

Discriminator: LeCroy 821 Quad Discriminator. When an input pulse reaches a user-set voltage value, it sends an output pulse on up to three lines per channel.

Delay Module: Phillips Scientific 792 Dual Delay Module. Provides up to 64 ns of delay of two channels, independently, at 0.5 ns increments.

.AND.: Phillips Scientific Quad Four-Fold Logic Unit. A fast logic (300 MHz) module that determines when pulses are coincident.

Counter 1: Ortec 974 four channel counter-timer with GPIB interface. This programmable counter provides three channels for monitoring count rates along with one channel that serves as a timer.

Counter 2: Ortec 994 two channel counter-timer with GPIB interface. This unit provides an additional counting channel, with the second used for controlling the counting period.

GPIB/USB: National Instruments GPIB-USB-HS. A computer interface that bridges the GPIB interface of the programmable counters to the USB port available in the usual desktop computer systems.

The pulses from the SPCMs are fed using two coaxial cables of equal length into the inputs of two different channels of the LeCroy 821 using pulse inverters and attenuators. The pulse inverter is required to match the positive voltage pulse (TTL) of the SPCM output to the negative current pulse (NIM) of the discriminator's input. The attenuator is required to match the output pulse amplitude to the discriminator's dynamic range.

The discriminator works as a filter for the input signal. As the input voltage exceeds a controllable threshold it produces a standard output NIM pulse of adjustable width on all of its three output channels. Its multiplexed output provides two signal outputs for use in the two (synchronized and desynchronized) coincidence-detection logic units, while leaving an additional output which can be used for probing with an oscilloscope. The voltage threshold for the output of a pulse was set to approximately 75% of the pulse height and the width of the pulse was set to the minimum of 6 ns.

The delay module is a simple device which houses two independent variable delay lines that are used for manipulating the synchronization of the two detection channels. The two channels were used in the signal path corresponding to the synchronized coincidence detection system. One was for the signal channel (PQ detector), set to zero delay and the other for the idler channel (AQ detector), set to 30ns of delay. This simplifies the design by providing the channels with fully symmetrical paths.

The fast logic module is a 4 channel unit that can work at up to 300 MHz. It has 4 inputs and 4 outputs per channel and can be configured for a variety of operations; 2 of these channels used for detecting synchronized and desynchronized coincidences. Both channels are configured for the AND operation, which outputs a pulse when two of its inputs share a high voltage level (due to a pulse) and overlap for at least 750 ps. The large differences in the output delay of both SPCMs already provide desynchronized channels at the output of the discriminators, thus the inputs for the desynchronized coincidence detection channel are directly taken from the discriminator outputs.

The two counters are configured through the National Instruments GPIB computer interface to use one channel as a timer set for 1 s of operation when the counting trigger is read; this timer uses an internal oscillator of high stability and feeds the timed pulses to a

counting channel, thus leaving the 974 module with three usable counters. These are used for counting the single photons from the signal and idler channels, and the synchronized coincidence discrimination stage. The 994 module's counting channel is used for counting the desynchronized coincidence detection channel.

A simpler arrangement (not shown) was used successfully for the Mk-I experiment. In this setup, the discriminator was replaced with a Fan-In/Fan-Out (FIFO) unit. The output pulse-width of this FIFO could not be set under 10 ns. Since the experiment produced moderate count rates, no significant amount of random coincidences were observed and the accidentals were not monitored. As the Mk-II experiment progressed, it became clear that this was insufficient for our needs. The solution would require a hardware component in the form of additional monitoring of accidental coincidences, and a software component in the form of linearity correction factors for the timing of the PQ detector.

Finally, the GPIB/USB interface allows us to use a computing system in controlling the counters through the use of GPIB-Linux set of drivers, which have been used to develop automation software in the C language.

3.5.1 Coincidence-detection logic gate evaluation

In order to test the time-delay tolerance and performance of our coincidence detection system, two cloned pulse trains from a pulse generator were fed into a channel of the coincidence-detection logic unit. These pulse-trains contained 1 ns long pulses at a frequency of 1 kHz. The coincidence detection count rate was monitored while a delay was introduced in the idler channels. Figure 13 shows the result of this measurement.

The coincidence detection was seen to behave as expected. Notice that there are no half-way data points, all observations measured either 1000 coincidences per second or 0 coincidences per second. This is evidence that the coincidence logic gate jitter is under 0.5 ns. Since different channels of the discriminator unit present different amounts of output lag, the distribution is not zero-centered.
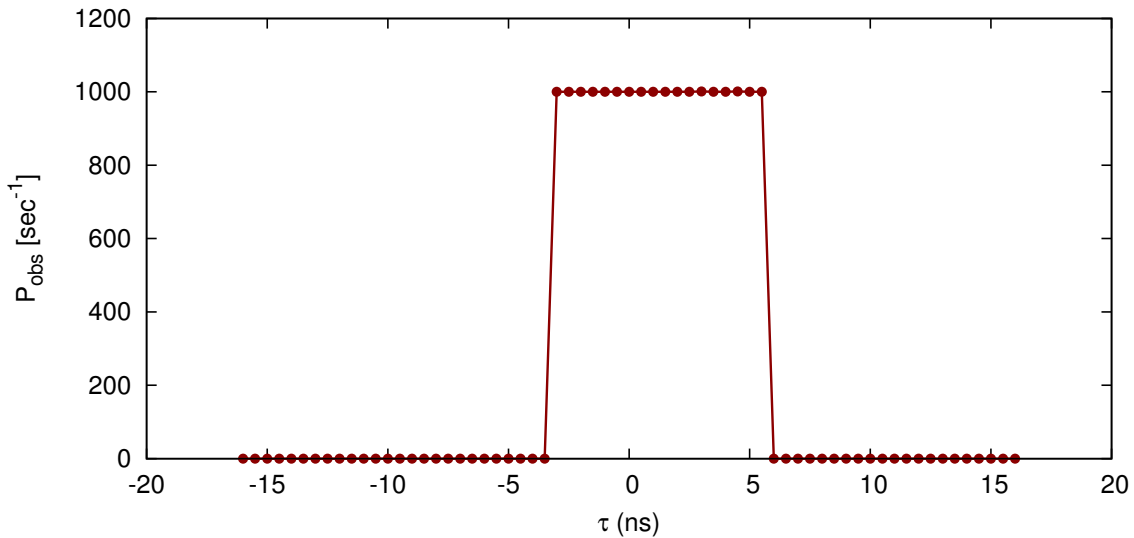
Figure 13: Experimental delay response for the coincidence detection system.

3.5.2 Coincidence discrimination and random coincidences

For ideal coincidence detection, the electronic pulses should be much narrower than the mean time between arrivals. Under these conditions there is a negligible chance for coincidence of photon pulses which do not arise from the coincident detection of entangled photon-pairs. The experiment with the free-space fiber coupling lies within this regime since the signal and idler detection channels measure a rate of 3000 photons/s and 6000 photons/s, respectively, and the temporal length of the pulses at the coincidence detection logic unit is 7 ns. With these conditions, the *duty-cycles* (fraction of time the voltage line is *high*) of the signal and idler's detection channels are less than 0.005% and 0.0025%, respectively. From these quantities it can be seen, even intuitively, that a source of uncorrelated photons with the same power levels would produce a negligible amount of coincidences per second due to random chance and that basically all of the coincidences detected in the free-space fiber coupling experiment are due to entangled photon-pairs.

In the case of the Mk-II experiment, it has been observed experimentally that the rate of photon detection is high enough to produce a non-negligible amount of randomly-coincident pairs. A quantitative description of this effect has been performed and is presented in Appendix B along with the methods that have been implemented to correct this spurious signal.
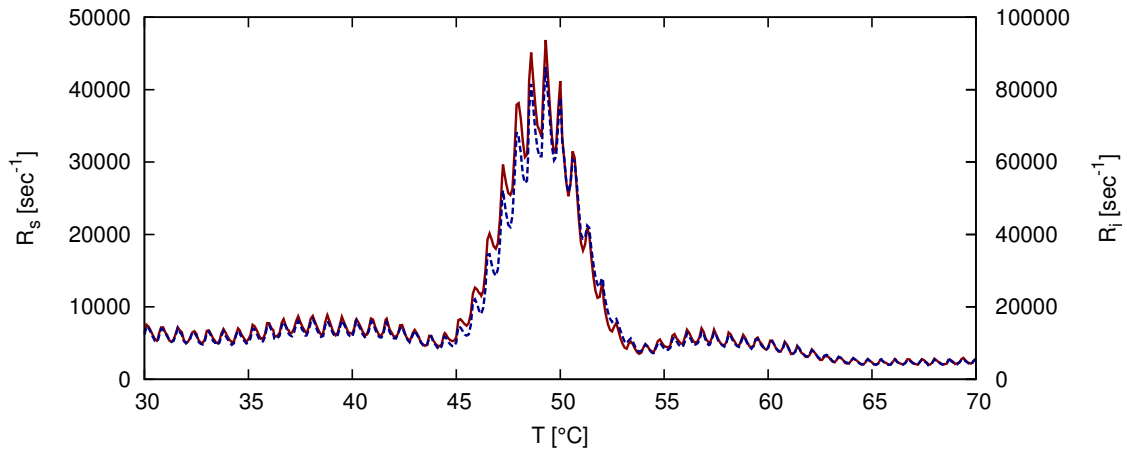
Figure 14: Signal rate R_s (solid line) and idler rate R_i (dashed line) of photo-detection as a function of crystal temperature. The high similarity between the curves indicates the channels are well aligned for coincidence detection since the maximum of the SPDC distribution occurs at essentially the same temperature in both detectors.

3.5.3 Pulse-train synchronization for coincidence detection

The observation of coincident photon-pairs requires many degrees of freedom to be set to well-defined parameters with high accuracy. These parameters include the optical alignment of two paths, the temperature of the crystal and the synchronization of the pulse-trains. The last of these parameters to be adjusted is the synchronization of the signal and idler pulse-trains. The methodology to follow can be challenging if the output lag of the detectors (from incidence of the photon to output of the pulse's leading edge) are unknown, as was our case. Some comments will be made here on the steps that were taken to achieve this condition.

Before attempting to synchronize the detectors, the distribution of light as a function of temperature must be measured in order to determine if the signal and idler channels are actually aligned. The two distributions should only differ in scale and not in the temperature at which the maximum is attained or the shape of the distribution. Adjustment of the signal polar angle must then be made until the temperature at which the photon counts are maximized is the same for both channels and this determines the working temperature. Figure 14 shows an example of two simultaneously measured distributions of single photons that exemplifies the close similarity that is achieved with a well aligned optical system.

Using the output-pulse width controls on the discriminator, the operator may set the width of the pulses to a width of over 50ns. The use of long pulses increases the synchronization tolerance of the coincidence detection module and signals from photon pairs will be immediately observed in the rate of coincidence detection. Notice that using long pulses also increases the chances for random coincidences and one must be careful when interpreting results since a background may develop. Our analysis of randomly coincident pulses, shown in Appendix B, includes some insight regarding techniques for identifying and removing this spurious signal.

The process is then finished by reducing the pulse length progressively, correcting the delay conditions on one of the channels as necessary and repeating this process until the minimal pulse length that can be set in the discriminator is reached.

3.6   Computer automation and interfacing through GPIB-Linux

The National Instruments GPIB-USB-HS computer interface allows computer automation for control and data collection of our counters. This interface is compatible with the GPIB-Linux driver package (which is available from `http://linux-gpib.sourceforge.net/`). This driver allows communication between a personal computer running an up-to-date GNU/Linux OS (Linux Mint 15) and the programmable counters through library bindings to several general-purpose programming languages such as C, Python, Perl, and others.

The C language binding was chosen for the development. Extensive documentation was written regarding the installation and testing of the GPIB interface. A series of single-purpose tools were built which serve as real-time monitors and alignment aides. Also, tools for automating data-collection of temperature and angular scans were developed.

All of the code and documentation has been published as open-source-software with a permissive license (BSD style) that allows commercial and non-commercial use. The repository may be found at `https://github.com/danieljg/ortec-gpib`.

Chapter 4.   Results and discussion

This chapter presents a selection of experimental results from our work and compares some of them with numerical calculations. The results from the MK-I experiment are shown in Section 4.1 while the measurements from the Mk-II experiment are shown in Section 4.2. These results include both crystal temperature and polar-angle (θ) scans. Two results from the crystal temperature scans with reduced apertures are also presented as a function of the longitudinal phase-mismatch using the relationship calculated in Subsection 2.3.1. In Section 4.3 we present results of the appearance of rate oscillations of classical origin as a function of crystal temperature variations, the comparison of theoretical and experimental phase-matching tuning curves, measurements from a two-mode pump, evaluation of crystal poling homogeneity, and experiments with the crystal center displaced along the optic axis from the beam waist.

4.1   Measurements with free-space fiber coupling

The Mk-I experiment, shown in Fig. 9, was aligned for fiber coupling at a polar angle of $\theta = 3°$ with a distance of 300 mm from the crystal to the fiber tips on both optical paths. Figure 15 shows the measured distribution of single-photon counts as the crystal temperature was varied. A well-defined distribution was found with an emission maximum at a crystal temperature of $T = 40°$C. This is consistent with the tuning curve presented in Fig. 1. The distribution has a FWHM of $\Delta T = 5°$C. The rates show a peak of over 2000 photons per second with a background of about 800 photons per second. With a detection efficiency of $\eta_i \approx 30\%$, this implies a signal power of $P = \frac{N\hbar\omega}{t} \approx 1 \times 10^{15}$ W $= 1$ fW on the detector.

The fibers were then set to a polar angle of $\theta = 1°$. Figure 16 shows the measured photon rates as a function of crystal temperature. We can see an increased amount of background and over twice the width when compared to the result of Fig. 15 which is due to the proximity to the optic axis. A maximum is found at $T = 62°$C with a narrower maximum centered at $T = 69°$C. The origin of the second maximum may be due to laser instabilities which, at the time of this measurement, had not yet been identified and monitored.

We attempted to observe photon pairs, but no signal was observed in the coincidence
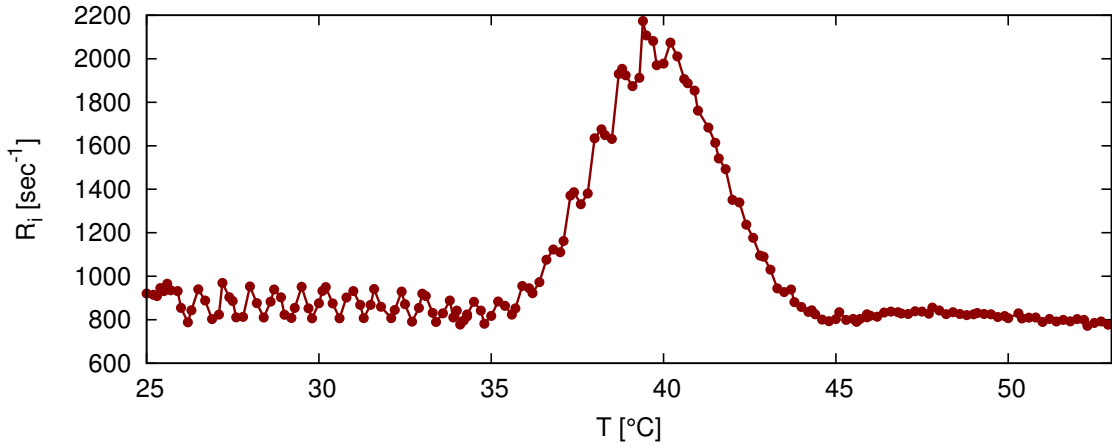
Figure 15: Measured idler photon rate R_i as a function of crystal temperature with the Mk-I experiment. The idler fiber is set to $\theta = 3°$ at a distance of 300 mm from the crystal.
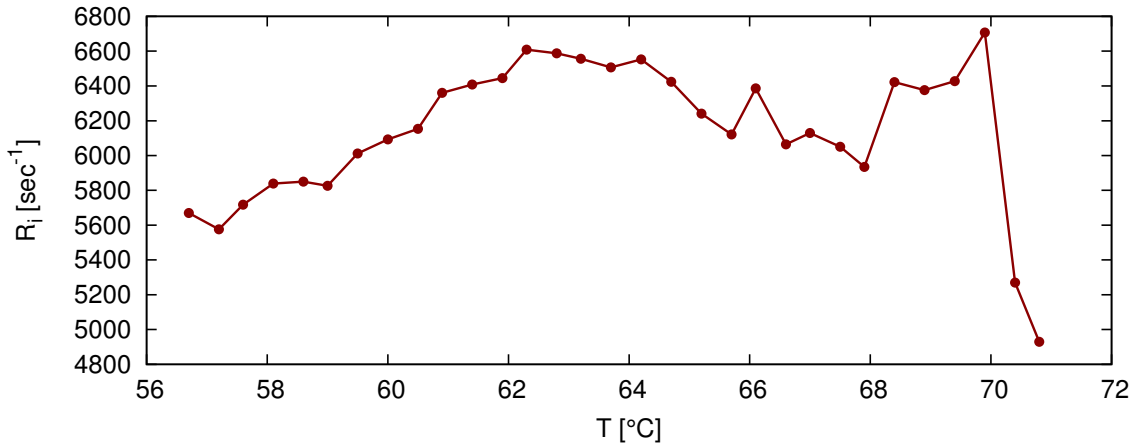
Figure 16: Measured idler photon rate R_i as a function of crystal temperature with the Mk-I experiment. The idler fiber is set to $\theta = 1°$ at a distance of 300 mm from the crystal.
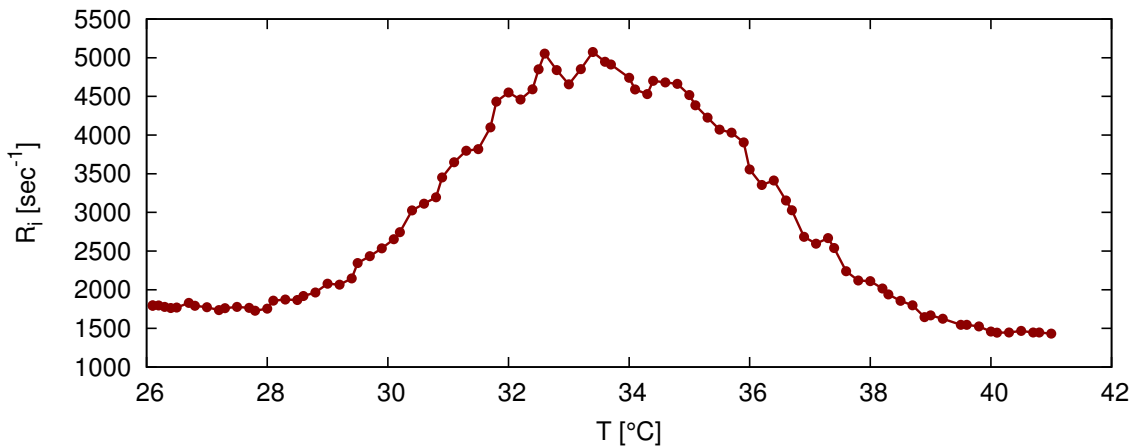
Figure 17: Measured idler photon rate R_i as a function of crystal temperature with the Mk-I experiment. The idler fiber is set to $\theta = 3°$ at a distance of 150 mm from the crystal.

detection system. In an attempt to increase the coupled power, the lengths from the fiber tips to the crystal were reduced to 150 mm and the system was aligned at a polar angle of $\theta = 3.3°$. Figure 17 shows the measured distribution. The emission maximum was found at a crystal temperature of $35.5°$C.

4.1.1 Distribution of photon pairs as a function of crystal temperature

The crystal temperature was brought to $34°$C and the electronic signal paths were synchronized by following the process described in Section 3.5.3. Detection of coincident photon pairs was observed. This coincident signal was then used to optimize the alignment for pair detection. Figure 18 shows the measured photon-pair distribution as a function of crystal temperature. The observed distribution presents a FWHM of $\Delta T = 5°$C.

4.1.2 Angular distribution of photon pairs

After setting the crystal temperature to the pair-detection maximum (34°C) the signal detection fiber was scanned along the polar angle (θ) and azimuthal angle (ϕ). The measured angular pair rate distributions are shown in Fig. 19 and 20 for the polar and azimuthal scans, respectively. The FWHM is $\Delta\theta_c = 0.145°$ for the polar angle and $\Delta\phi_c = 0.16°$ for the azimuthal angle.

These measurements determine the uncertainty in the emission direction of a (band-limited) photon pair which is the so-called coherence cell. $\Delta\theta_c$ and $\Delta\phi_c$ are known as
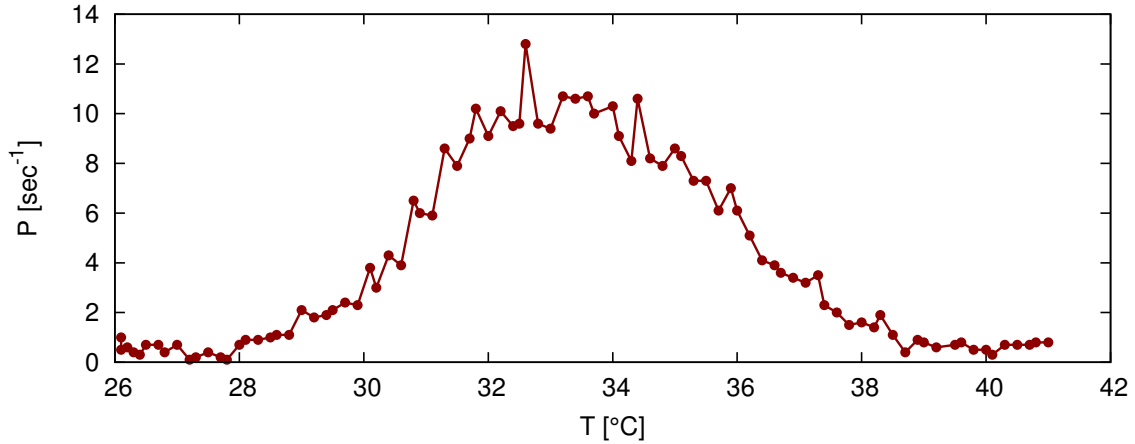
Figure 18: Measured pair rate P **as a function of crystal temperature with the Mk-I experiment. The fibers are set to** $\theta_{s,i} = 3.3°$ **at a distance of 150 mm from the crystal.**
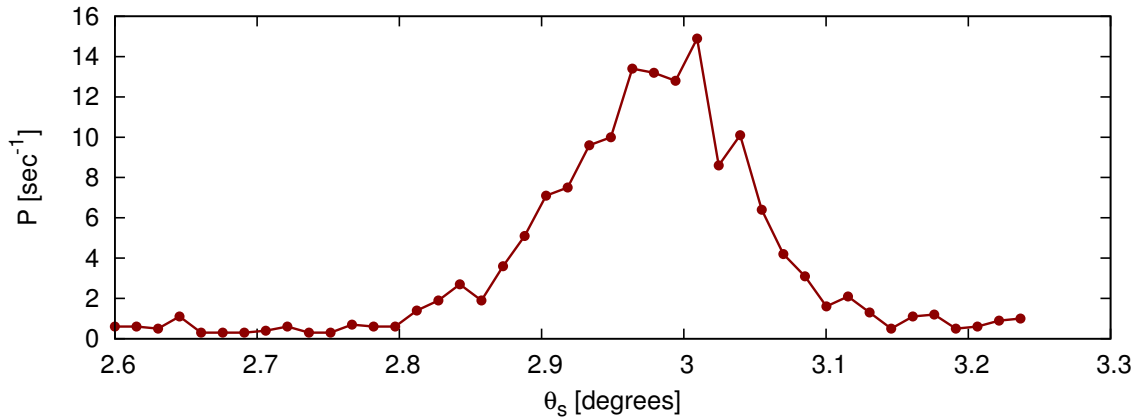
Figure 19: Measured pair rate P **as a function of signal polar angle with the Mk-I experiment. The idler detector remains fixed at** $\theta_i = 3°$ **and** $\phi_i = \pi$. **The crystal temperature is** $T = 40°C$.
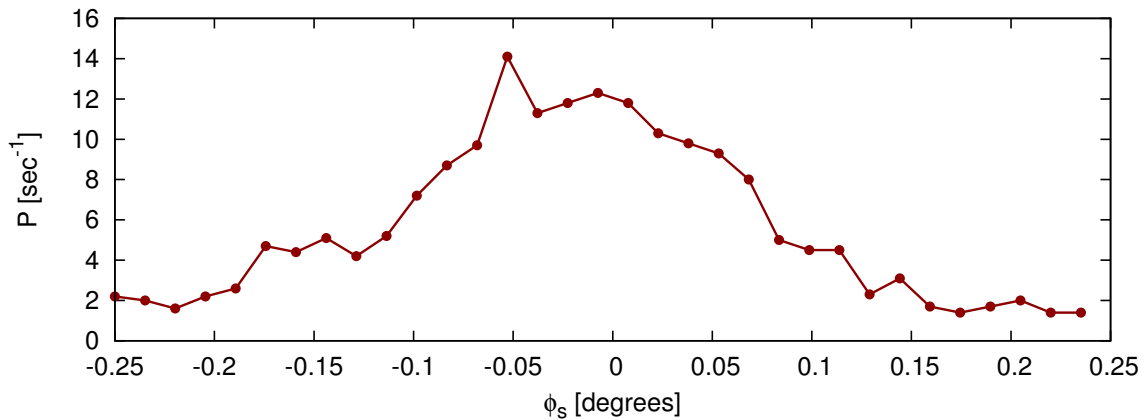
Figure 20: Measured pair rate P **as a function of signal azimuthal angle with the Mk-I experiment. The idler detector remains fixed at** $\theta_i = 3°$ **and** $\phi_i = \pi$. **The crystal temperature is** $T = 40°C$.

the polar and azimuthal coherence angles, respectively. Knowledge of these parameters is crucial in the design of efficient photon-pair detection experiments. In their influential work, Joobeur and coworkers [Joobeur *et al.* (1996)] derived approximate expressions for these coherence angles using a Gaussian expression for the phase-matching function. Evaluation of this function yields the estimation of $\Delta\theta_c = 0.141$ which is in good agreement with our experimental value.

4.2   Measurements with lenses and irises

The Mk-II experiment, shown in Fig. 10, uses a lens and iris system in front of each of the optical fibers to couple the contribution within a solid angle to the detectors to achieve higher rates. This section presents a selection of measurements which were performed using this experiment and the photon-pair distributions are compared with numerical integrations. The integrations correspond to the experimental cited conditions as described on Subsection 2.2.2. Aperture sizes are reported as diameters and are accurate to ± 0.5 mm. The complete set of measurements can be found in Appendix C.

The optical detection system was aligned for photon pair detection at a polar angle of approximately $\theta = 2.5°$. Calculations show that this observation angle presents a phase-matching temperature of $T_{\mathrm{pm}} = 49.1°$C, while the experimental maximum was found at $T_{\mathrm{pm}} \approx 48.8°$C. The angular and crystal temperature distributions of the photon pairs were measured with different aperture settings to probe the effect of integration angle. The computed $G^{(2)}$ values were scaled with a linear factor γ to compare them with the experimental rates using $P = \gamma G^{(2)}$. The corresponding γ factor is reported for each comparison.

4.2.1   Angular distribution of photon pairs and integration angle effects

Figure 21 shows the result of a polar angular scan on the signal detection arm θ_s. The signal and idler apertures were set to less than 1 mm. The results are compared with two distributions from numerical calculations corresponding to apertures of 0.5 mm ($\gamma = 3.67 \times 10^{-4}$) and 1 mm ($\gamma = 2.82 \times 10^{-5}$). Aside from the amplitude difference, the two computed distributions are similar with small effects due to integration angles. The experimental distribution is noticeably narrower with a FWHM of $\Delta\theta = 0.18°$ while the numerical distributions present widths of $\Delta\theta = 0.18°$ and $\Delta\theta = 0.19°$ for the cases with 0.5 mm
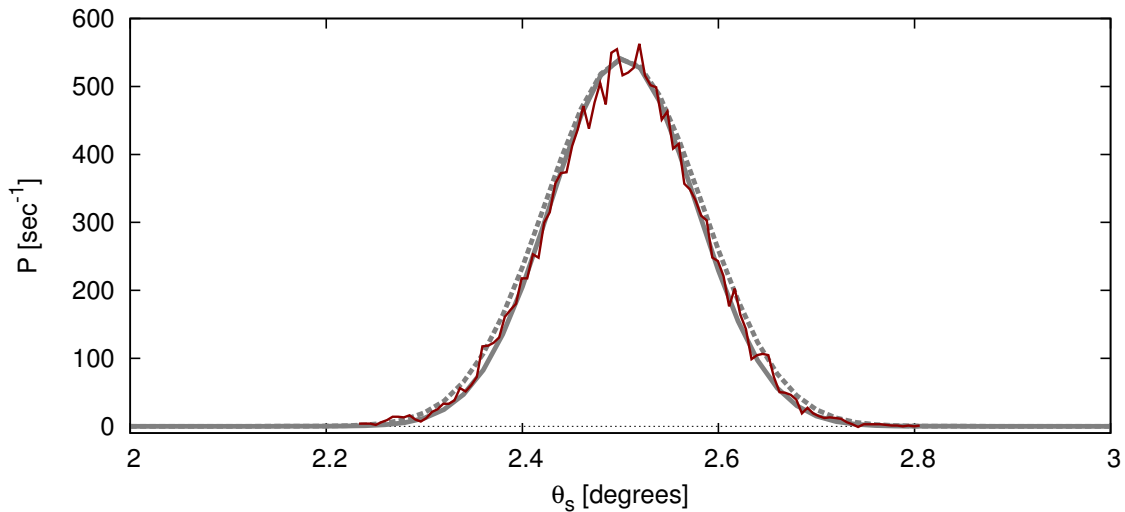
Figure 21: Measured pair rate (solid line) P as a function of signal polar angle. The apertures are less than 1 mm. Numerical calculations are shown for comparison with apertures of 0.5 mm (gray solid line) and 1 mm (dashed line).

and 1 mm apertures, respectively. The close similarity between the calculated results for apertures of 0.5 mm and 1 mm shows that an experimental uncertainty on aperture sizes below 1 mm is not significant in terms of comparing the results, apart from the expected scaling due to difference in coupled power.

Figure 22 shows the experimental and numerical results ($\gamma = 1.56 \times 10^{-4}$) of polar angular scans with the signal aperture set to 0.5 mm and the idler aperture set to 5 mm. The experimental distribution has a width of $\Delta\theta = 0.24°$, while the calculated distribution has a width of $\Delta\theta = 0.23°$. This figure also includes a comparison with $|\psi|^2$, evaluated at the center of the detection apertures and at signal and idler frequencies of $\omega_s = \omega_i = \omega_p/2$, which presents a width of $\Delta\theta = 0.17°$. The squared wave function $|\psi|^2$ is proportional to the differential pair-rate measured by point detectors with infinitely-narrow detection bandwidths and is included to evaluate the integration effects from increasing the idler detection aperture. It can be seen that the experimental and theoretical results are in good agreement with both of these significantly wider than $|\psi|^2$. Additionally, $|\psi|^2$ is similar to the result of Fig. 21, which is consistent with our observation that small apertures (under 1 mm) do not significantly alter the pair-rate distribution shape.

Figure 23 shows the experimental and numerical results ($\gamma = 6.67 \times 10^{-5}$) of polar angular scans with the signal and idler apertures at 5 mm. Integration angle effects lead
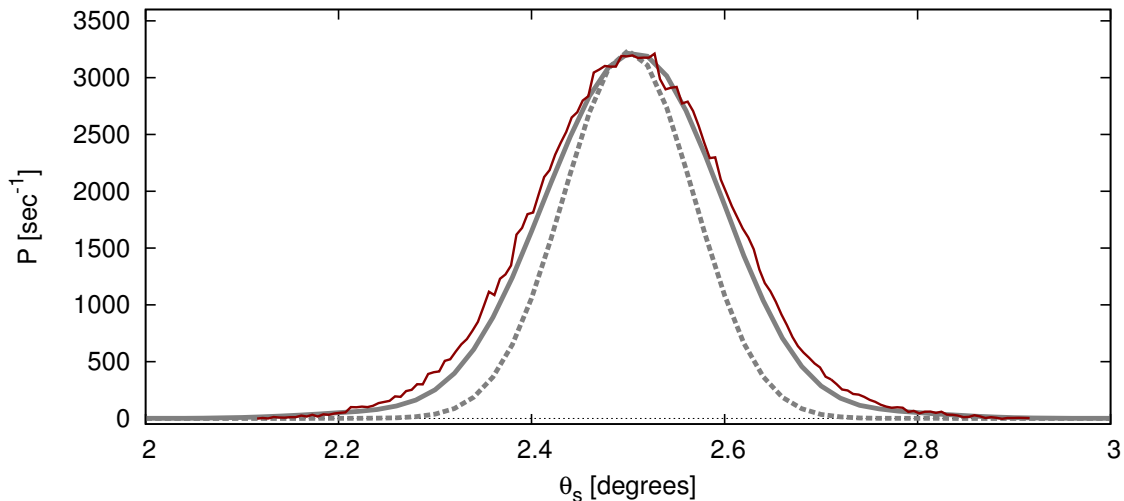
Figure 22: Measured pair rate (solid line) P as a function of signal polar angle. The signal aperture is less than 1 mm, the idler aperture is 5 mm. A numerical calculation is shown with a 0.5 mm signal aperture and a 5 mm idler aperture (gray solid line) along with $|\psi|^2$ (dashed line) to evaluate integration effects.

to an increased pair rate and a wider, flatter distribution of pairs. The measured widths are $\Delta\theta = 0.485°$ and $\Delta\theta = 0.49°$ for the experimental and calculated distributions, respectively, in excellent agreement.

These results show that the width of the photon-pair distribution increases for aperture diameters over 1.0 mm. The integration angle effect is stronger when both apertures are set to large values, as can be seen from Figs. 22 and 23. Thus, the use of asymmetric apertures may significantly improve the observed pair rates without a large increase in the observed width of the distribution.

4.2.2 Crystal temperature dependence of the pair rate and integration angle effects

Figure 24 shows the observed rate of pair detection P as the crystal temperature was varied with the apertures set to less than 1 mm at equal angles of $\theta = 2.5°$. These are the same conditions as used for the angular scans of Subsection 4.2.1. The distribution is compared with a numerical calculation ($\gamma = 3.6 \times 10^{-4}$) with 0.5 mm apertures. The experiment presents a FWHM of $\Delta T = 2.8°C$, while the numerical distribution has a FWHM of $\Delta T = 2.7°C$. Secondary and tertiary lobes are present in the experiment and the calculations, as are the minima between them. For purposes of evaluating integration angle effects, the figure also shows the plot of $|\psi|^2$ evaluated at the center of the apertures
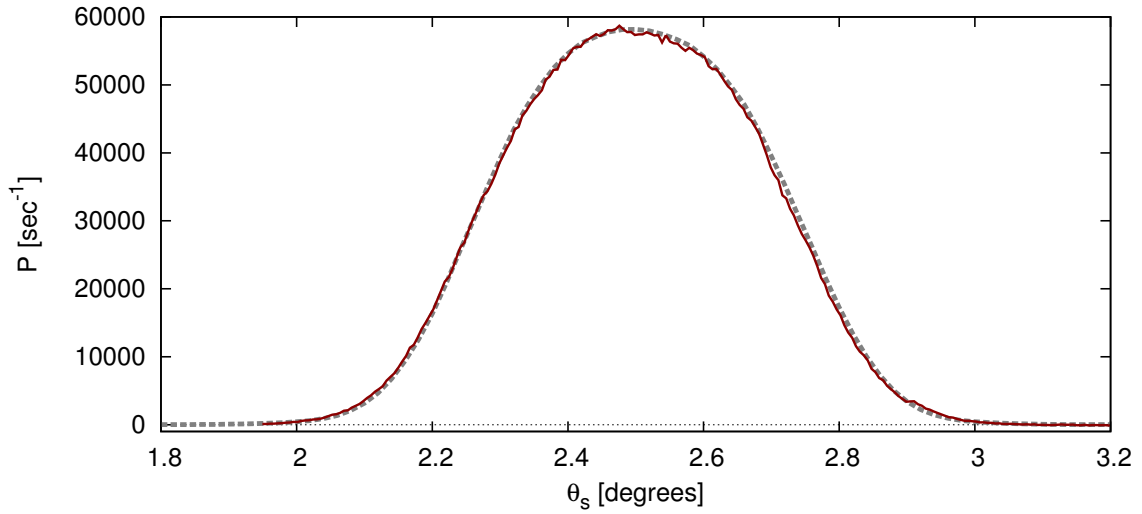
Figure 23: Measured pair rate (solid line) P as a function of signal polar angle. The apertures are set to 5 mm. A numerical calculation is shown with 5 mm apertures (dashed line).
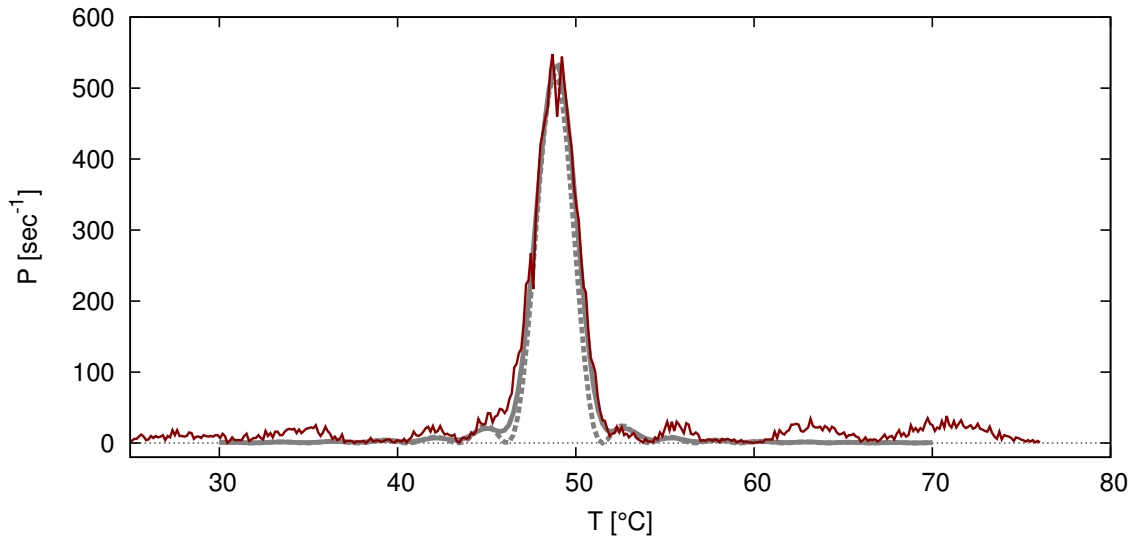
Figure 24: Measured pair rate (solid line) P as a function of crystal temperature with apertures set to less than 1 mm. The signal and idler polar angles are $\theta = 2.5°$. A numerical calculation (gray solid line) is shown with 0.5 mm apertures along with $|\psi|^2$ (dashed line) to evaluate integration effects.
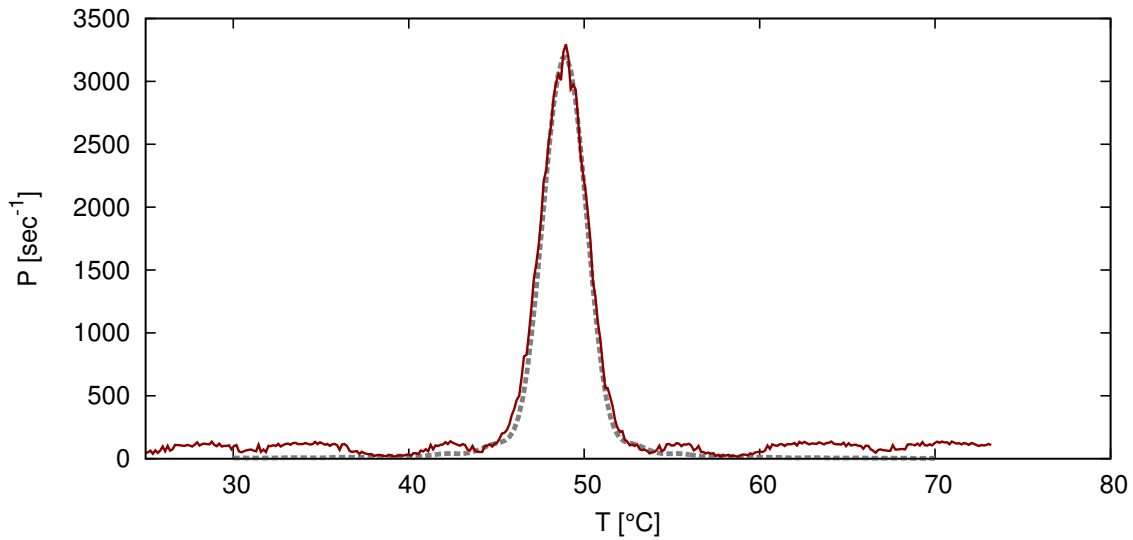
Figure 25: Measured pair rate (solid line) P as a function of crystal temperature with the signal aperture set to less than 1 mm and the idler aperture set to 5 mm. The signal and idler polar angles are $\theta = 2.5°$. A numerical calculation (dashed line) is shown with 0.5 mm signal aperture and 5 mm idler aperture.

and at the signal and idler frequencies of $\omega_s = \omega_i = \omega_p/2$. A non-negligible amount of pairs is found at crystal temperatures under $40°$C and over $60°$C, where the theory predicts no significant amount of pairs. Since the measurements are corrected for accidental coincidences, these are valid observations of entangled photon pairs. The origin of this structure may be due to imperfections in the poling structure of the crystal introducing additional contributions to the phase-matching function.

Figure 25 shows the measured pair rate P as a function of crystal temperature with the signal aperture set to less than 1 mm and the idler aperture set to 5 mm. This distribution is compared with a numerical calculation ($\gamma = 1.55 \times 10^{-4}$) with a signal aperture of 0.5 mm and an idler aperture of 5 mm. The experimental distribution has a width of $\Delta T = 3.2°$C, while the calculated distribution has a width of $\Delta T = 3.1°$C. Compared to figure 24, the photon pairs outside the main distribution present their maxima and minima at similar crystal temperatures, but the relative contrast is diminished from the increased integration angle in the idler aperture, as can be seen from the measurements at crystal temperatures over $T = 60°$C.

Figure 26 shows the measured pair rate P as a function of crystal temperature with apertures set to 5 mm and compares it with a numerical calculation ($\gamma = 2.09 \times 10^{-5}$) with
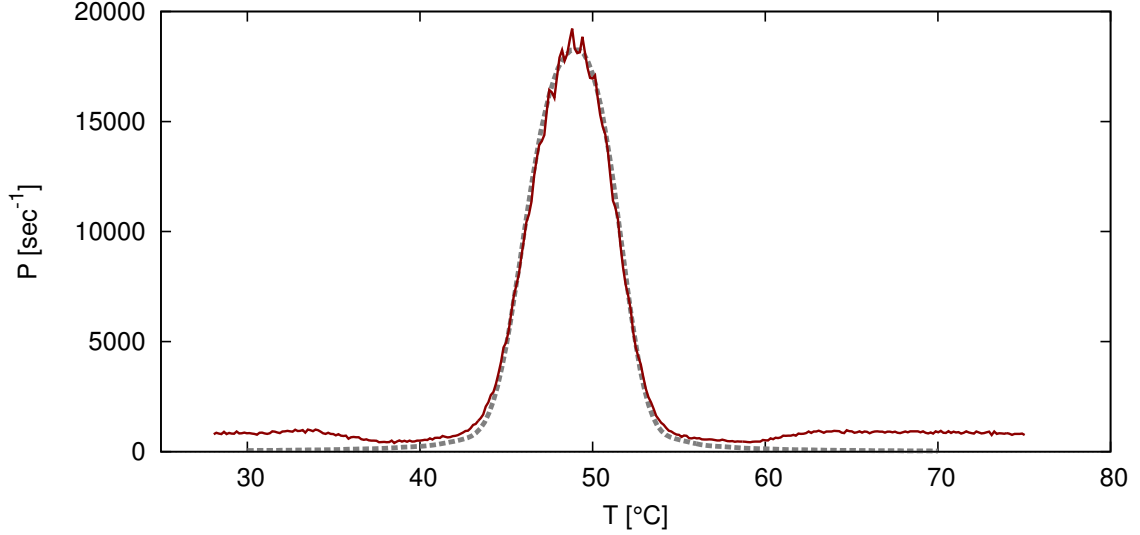
Figure 26: Measured pair rate (solid line) P as a function of crystal temperature with 5 mm apertures and a corresponding numerical calculation (dashed line). The signal and idler polar angles are $\theta = 2.5°$.

the same apertures. The experimental result was measured with approximately 25% of the available pump power to reduce the amount of corrections due to pair-rate saturation, as described in Section A.3. The two distributions are remarkably similar in shape and width aside from the entangled photon pair background far from the phase-matching crystal temperature (most noticeable at crystal temperatures under $T = 35°$C and over $T = 60°$C). The experimental and numerical distributions have widths of $\Delta T = 5.7°$C.

4.2.3 Longitudinal phase-mismatch dependence

As has been shown in Subsection 2.3.1, for observation of degenerate pairs at equal signal and idler polar angles $\theta_s = \theta_i$, a one-to-one relationship can be made between crystal temperature T and the rationalized sinc function argument $\frac{\Delta k_z L}{2\pi}$ which is largely due to the variations in the longitudinal phase-mismatch Δk_z. Thus, the measurements from a crystal temperature scan can be transformed to be a function of the sinc function argument and observations of the phase-matching function can be made, assuming integration effects from detected bandwidth and observation apertures are small.

In figure 27 we show the result of two crystal-temperature scans, with apertures set to 0.25 mm for one case and 0.5 mm for the other, at polar observation angles of $\theta_s = \theta_i = 2.5°$, as a function of the estimated rationalized sinc function argument $\frac{\Delta k_z L}{2\pi}$, along
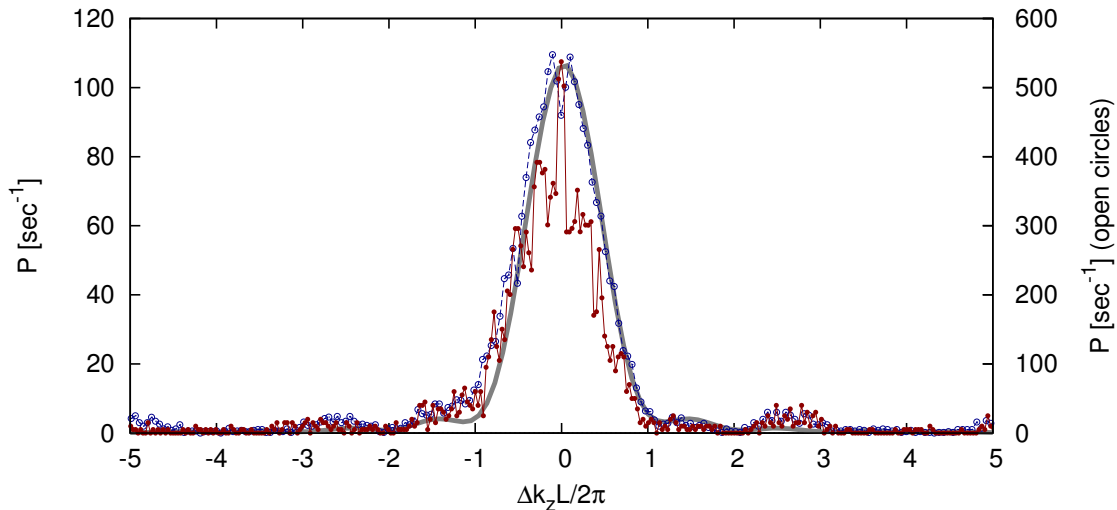
Figure 27: Measured pair rate P as a function of the rationalized sinc function argument $\frac{\Delta k_z L}{2\pi}$. The result with solid circles corresponds to the observation with 0.25 mm and the result with open circles corresponds to the observation with 0.5 mm (using the y scale on the right hand side) with 5 mm apertures and a numerical calculation with apertures set to 0.5 mm (gray solid line). The signal and idler polar angles are $\theta = 2.5°$ for both results.

with a theoretical curve (using 0.5 mm apertures) for comparison. As can be seen, the two experimental results are in excellent agreement. The pair-rate structure around the phase-matching peak is seen to be mostly identical in the two observations, even though the Poisson noise is quite strong in the measurement with smaller apertures due to the lower observed rates.

4.3 Results of applied interest

This section presents results which have been observed during the development of this work that are of interest towards applications. They have all been measured using the Mk-II experiment, except for the crystal-temperature dependent oscillations, which can be seen in both the Mk-I and the Mk-II systems. The idler detection aperture is kept at a polar angle of $\theta = 2.5°$. Another applied result of our work is presented in Appendix A which is the detailed characterization of SPCMs using photon pairs for use in the correction of pair-rate saturation.

4.3.1 Crystal-temperature dependent rate oscillations

In some of our observations the photon rates present oscillations as the crystal temperature is varied. The oscillations are also present in the pair rate and are, when present,

more noticeable. This effect has a classical origin due to multiple beam interference of the pump beam within the crystal. The fringe periodicity may be calculated by considering the required temperature change ΔT that would increase the phase ϕ of the pump wave over a round trip through the crystal by $\Delta\phi = 2\pi$. This phase change accounts for the difference in optical path due to the variations in refractive index [Emanueli and Arie (2003)] and elongation of the crystal [Gurzadyan *et al.* (1991)] with temperature T. The calculation yields (at $30°$) $\Delta T_{\text{fringe}} = 0.727°$ while the experimentally determined period for the fringes at this temperature is $\Delta T_{\text{fringe}} = 0.73°$, in good agreement.

The appearance of the fringes is expected since our PPKTP crystal does not have optical coatings for anti-reflection. The fringe visibility can be estimated by using the Fresnel coefficients and the geometric series, as is usually done in calculating transmittance of a single thin film by classical interference [Born and Wolf (1999)]. The evaluation of this expression yields a visibility of 20% for single photon detection which implies a visibility of 40% for pair observation. This result assumes that the optic axis is exactly orthogonal to the crystal's face. However, the actual experiment is intentionally brought slightly out of this condition in order to prevent back-reflected photons reaching the pump diode and destabilizing the laser operation. When the crystal is not normal to the crystal face, the overlap between the pump beam and its internal reflections is reduced and, thus, the visibility of the experimental fringes may be reduced from the values just mentioned.

The fringes significantly reduce the tolerance for temperature changes in the PPKTP crystal. It is possible that applied experiments using photon pairs which require high pair-rate stability are affected by these fringes, since the temperature stability requirements of the system are effectively increased to a fraction of the fringe period. The use of anti-reflective coatings may yield true benefits to such work as the tolerance would then be determined by the fundamental features of the pair distribution, which are broader and may present a tolerance of $\sim 1°$C or larger (depending on aperture diameters).

4.3.2 Comparison with phase-matching temperature-tuning curve

Figure 28 shows the rate of single photon detection of three polar angle scans using the signal detector at 0.5 mm apertures. The plot shows that the polar angle of emission of
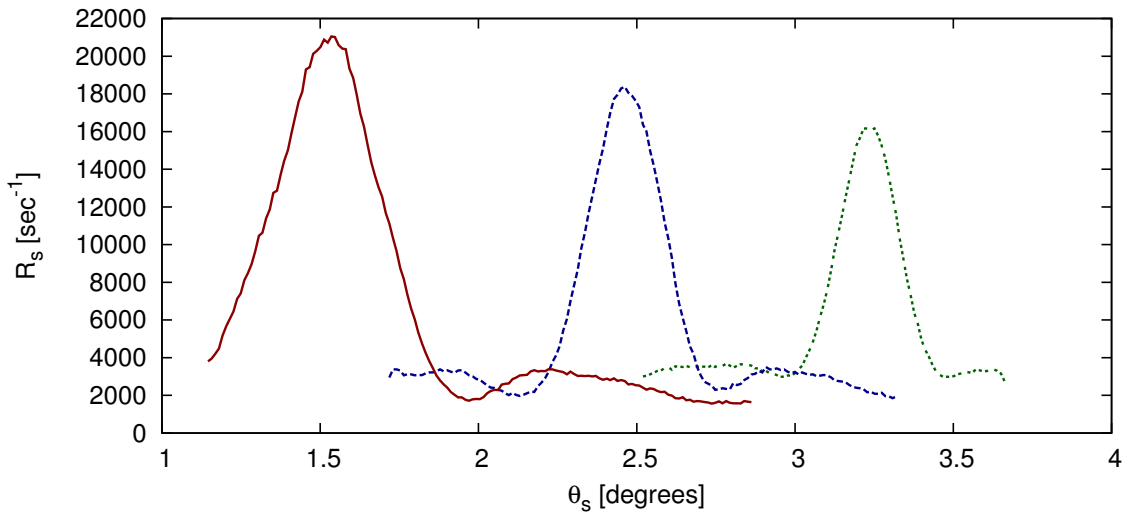
Figure 28: Measured signal photon rate R_s as a function of signal polar angle for crystal temperatures of $T = 60.0°$C (solid line), $T = 48.7°$C (long-dashed line), and $T = 34.9°$C. The aperture is set to 1 mm.

the rings of light produced in degenerate SPDC is decreased as the temperature of the crystal is lowered. Additionally, the distribution is widened as it approaches the optical axis, as had been observed previously with the Mk-I experiment in Subsection 4.1.2.

We extracted the polar angle of peak emission from a total of nine angular scans at different crystal temperatures, which include those of Fig. 28. Figure 29 shows the resulting angle of peak emission as a function of crystal temperature and compares it with the phase-matching temperature-tuning curve of Fig. 1. The experimental result is in good agreement with the theoretical curve. It must be said that the theoretical angular position of peak emission is not exactly the same as the phase-matching angle which may account for the small discrepancies at measurements over $T = 60°$C. Since these results depend strongly on the dispersion relations [Fradkin *et al.* (1999)] and temperature dependence [Emanueli and Arie (2003)] of the refractive index $n_z(\lambda, T)$ of KTP, this may be seen as a verification of the models that were used in our calculations. Performing this experiment for non-degenerate configurations could be used for further testing of the reported models.

4.3.3 Measurements with two-mode laser operation

The operation of the stabilized laser diode requires a careful selection of the diode temperature while monitoring the emission spectra to insure single-frequency operation. With
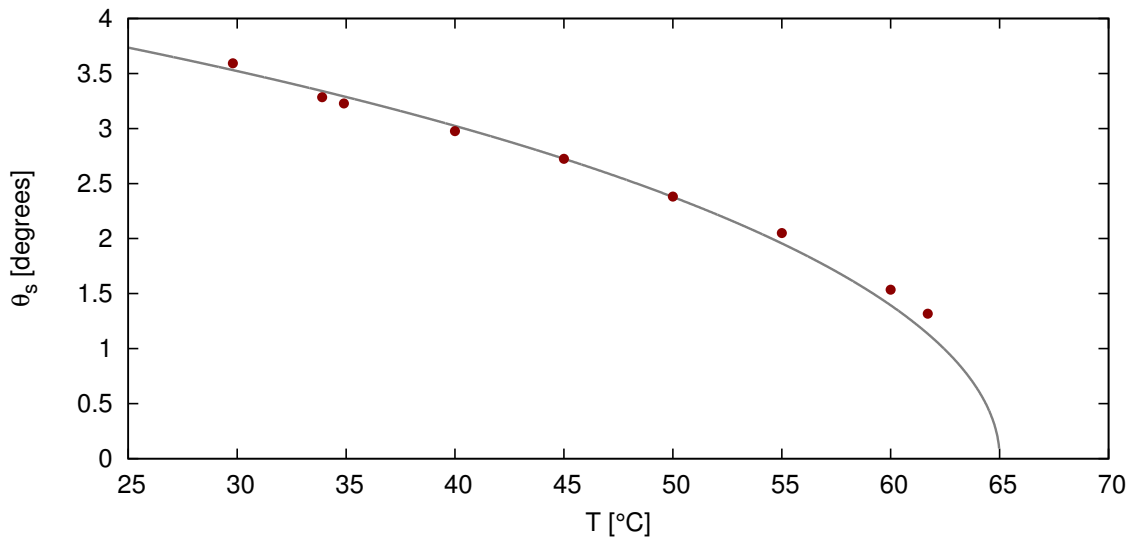
Figure 29: Signal polar angle θ_s of maximum collected power as a function of crystal temperature (solid circles) compared to the temperature tuning curve derived from the quasi-phase-matching condition (solid line).

careful choice of a working diode temperature, it has been possible to induce two-mode operation in the laser diode for extended periods of time. Figure 30 shows an observation under two mode laser operation of the rate of single photons in the signal detector as a function of the polar angle of observation θ_s. Evidence of unstable laser behavior may be seen in the discontinuity at $\theta_s = 2.6°$. The angular separation of the two peaks is $\Delta\theta = 0.55°$. Numerical calculations have shown that this implies a wavelength spacing of $\Delta\lambda_p = 0.22$ nm between the two modes. Figure 31 shows the corresponding pair rates. As the idler polar angle is $\theta = 2.5°$, the pairs emitted around $\theta = 2.6°$ have a higher coincidence rate than those emitted around $\theta = 2.05°$.

Figure 32 shows the pair rate P as a function of crystal temperature with the laser in two mode operation and 0.5 mm apertures. The two modes are similar in width and are separated by $\Delta T = 9°$C. The width of these distributions is $\sim 30\%$ larger than those seen in Fig. 24, which were observed with comparable aperture sizes. A corresponding measurement with 5 mm apertures is shown in Fig. 33. The crystal temperature separation between the two peaks is again $\Delta T = 9°$C. Numerical calculations show that this is consistent with a wavelength separation between modes of $\Delta\lambda_p = 0.25$ nm. The distribution centered at the lower temperature has a width which is consistent with that of Fig. 26 which has been calculated with a pump bandwidth of 20 pm (as all the numerical calculations of
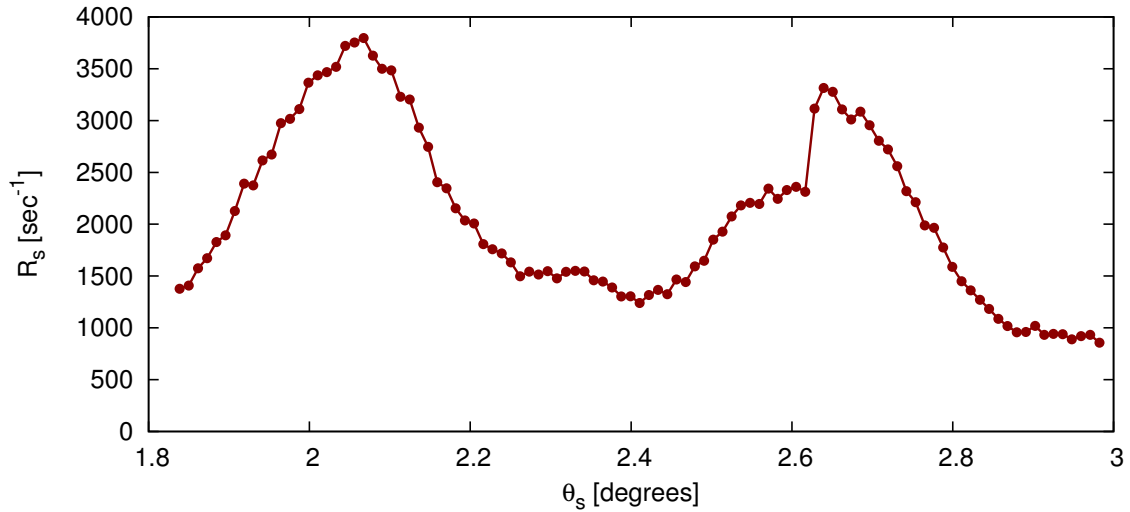
Figure 30: Measured signal photon rate R_s as a function of signal polar angle with the pump laser in two-mode operation. Crystal temperature is $T = 51°C$.
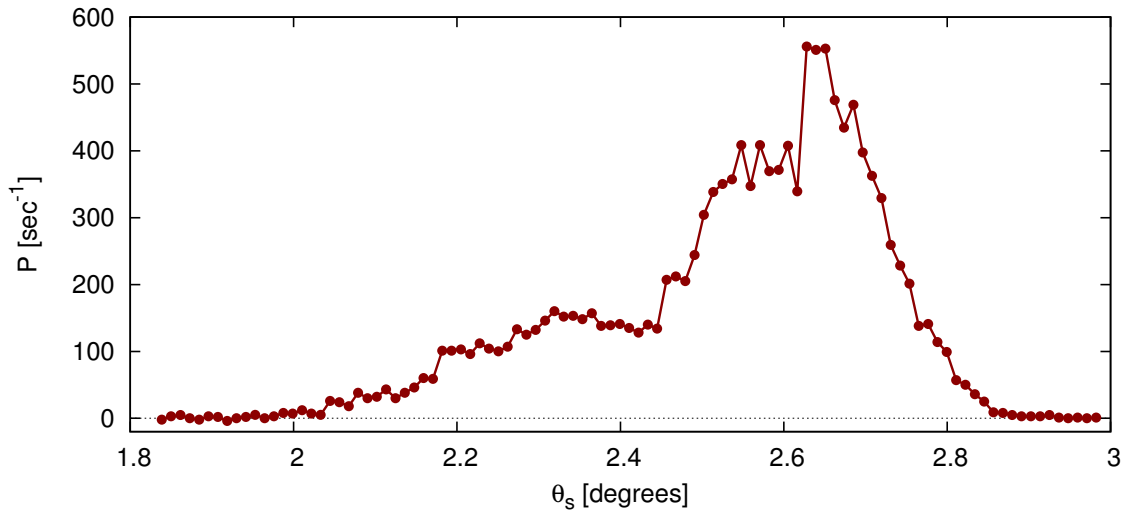
Figure 31: Measured pair rate P as a function of signal polar angle with the pump laser in two-mode operation. The signal aperture is 0.5 mm, the idler aperture is 5 mm, and the crystal temperature is $T = 51°C$.
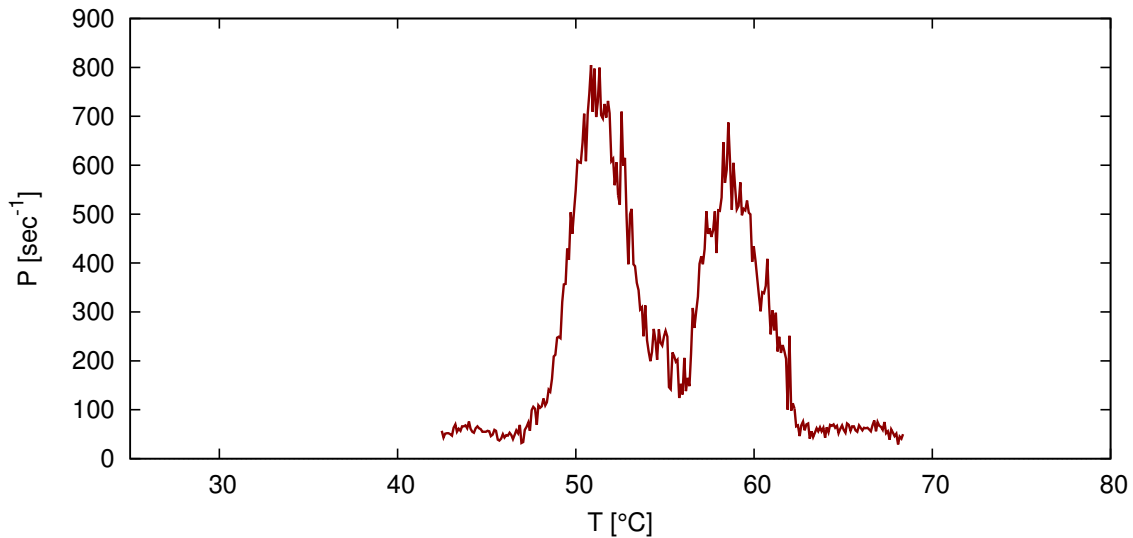
Figure 32: Measured pair rate P as a function of crystal temperature with the pump laser in two mode operation. The apertures are set to 0.5 mm at signal and idler polar angles of $\theta = 2.5°$.

this work), while the distribution centered at the higher temperature is clearly wider. This width of the distribution observed at a higher temperature is consistent with numerical calculations for which the pump bandwidth is 100 pm, indicating that the bandwidth of each of the laser modes of operation may vary significantly. The manufacturer of the laser diode reports a bandwidth of 70 pm in the data sheet.

4.3.4 Evaluation of crystal poling homogeneity

Previous theoretical studies [Fejer *et al.* (1992)] of second-harmonic generation in PPKTP have shown that manufacturing imperfections on the ferroelectric domain structure may affect the phase-matching function. The introduced changes can include a reduction of the expected output power, an increased width of the principal phase-matching lobe, and the appearance of additional components in the phase-matching function, among others. Figures 24, 25 and 26 have shown evidence of additional components in the phase-matching function in the form of a non-negligible pair rate at crystal temperatures that are far from the theoretical quasi-phase-matching distribution's maximum.

The quality of the domain structure may be evaluated experimentally by displacing the crystal along the poling direction of the poling and comparing the measured pair rates and phase-matching distributions [Wang *et al.* (1999)]. For our sample of PPKTP, the poling direction corresponds to the crystal's z axis which is transverse to the optic axis and is
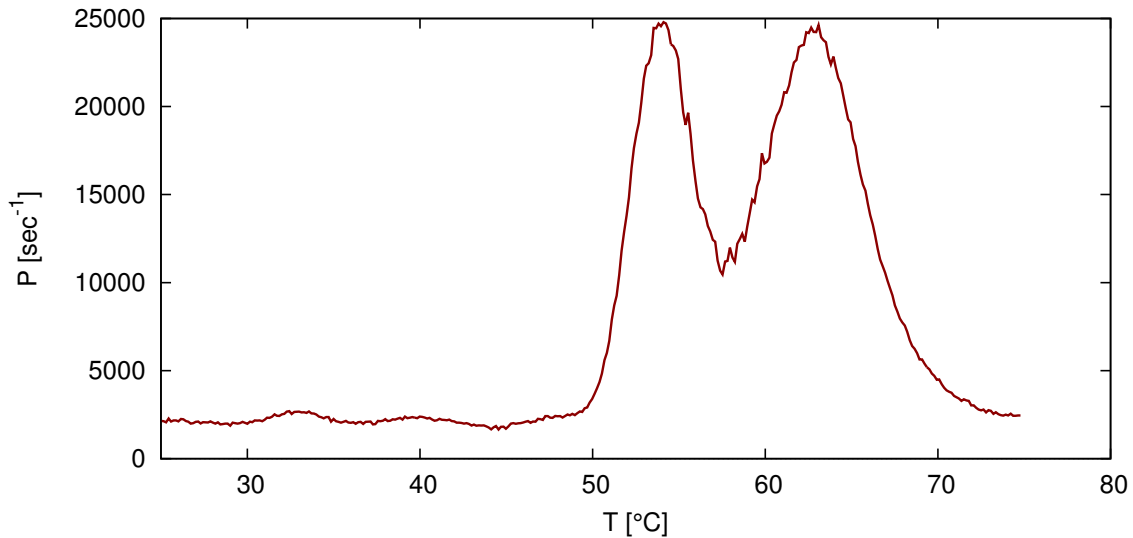
Figure 33: Measured pair rate P as a function of crystal temperature with the pump laser in two mode operation. The apertures are set to 5 mm at signal and idler polar angles of $\theta = 2.5°$.

accessible through micrometer displacement as shown in Fig. 8. The face of the crystal is 1 mm wide along the crystal axis z. The position of the pump beam along this direction is denoted by z_{pump} in the following.

Figure 34 shows the pair rate as a function of crystal temperature at two pump beam positions along the z crystal axis $z_{\mathrm{pump}} = 0.48$ mm and $z_{\mathrm{pump}} = 0.95$ mm. This comparison shows that as the position along the crystal's z axis increases, the width ΔT_c of the distribution increases while the peak pair decreases. Although only two measurements are shown here for clarity, the rest of the measurements along the z axis follow this same tendency. Figure 35 shows the measured pair rate as a function of the pump beam position z_{pump} along the crystal axis z (transverse to the optic axis z). Given that a perfectly poled crystal would present equal power near the two sides of the crystal (as well as equal distribution widths), the slope of the curve suggests that a side of the crystal presents higher domain quality than the other. The measurements presented elsewhere in this work were performed with the pump beam at $z_{\mathrm{pump}} = 0.25$ mm.

Previous demonstrations of this technique had used SHG in PPKTP [Wang *et al.* (1999)], showing a result of marked similarity to that of Fig. 35 for a case with poling periodicity $\Lambda = 2.95$ μm, which is close to our $\Lambda = 3.425$ μm. The main advantage of using entangled photon pairs for this application is that the process of coincidence detection and accidental
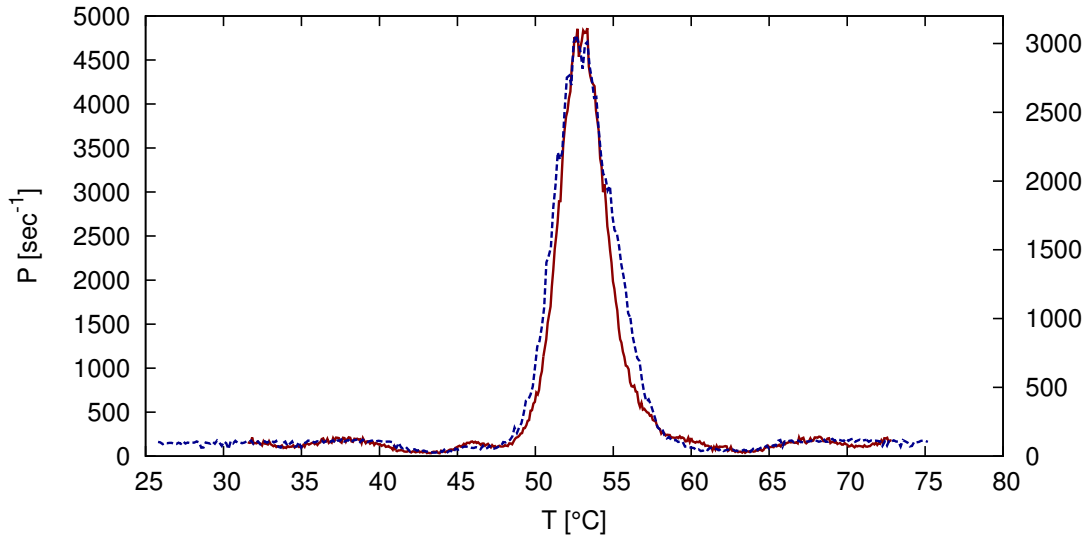
Figure 34: Rate of photon pair detection P as a function of crystal temperature at two positions of the pump beam along the crystal z axis. The solid line was measured at $z_{pump} = 0.48$ mm and the dashed line was measured at $z_{pump} = 0.95$ mm (using the y axis on the RHS). The signal aperture is 0.5 mm, the idler aperture is 5 mm and the polar angles of observation are both $\theta = 2.5°$.
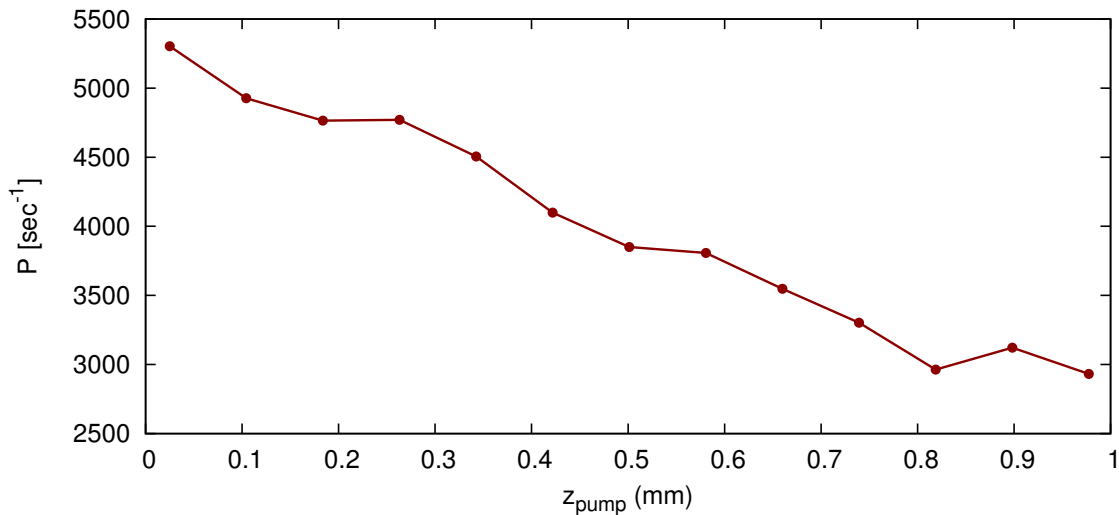
Figure 35: Rate of photon pair detection P as a function of the pump beam position z_{pump} along the crystal axis z (transverse to the pump beam direction). Signal aperture is set to 0.5 mm, idler aperture is set to 5 mm, the crystal temperature is $T = 51°C$, and $\theta = 2.5°$.
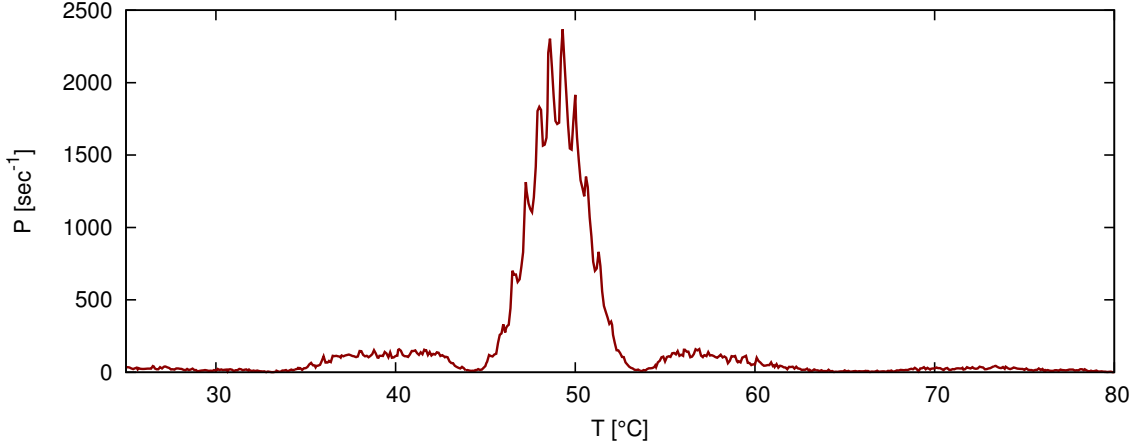
Figure 36: Rate of pair detection P as a function of crystal temperature with the crystal displaced 7 mm along the optic axis towards the pump. The apertures are 1 mm and the observation angle is $\theta = 2.5°$.

removal produces a detected signal with no background. This allows observation of the fine structure in the phase-matching function with accuracy.

4.3.5 Observations with crystal displaced from the beam waist

Figure 36 shows the measured pair rate P as a function of crystal temperature T with the crystal displaced along the optic axis by 7 mm towards the pump. At this position, considering our crystal is 5 mm long, the beam waist is not located inside the crystal. Both apertures are set to 1 mm at an observation angle of $\theta = 2.5°$. The result shows the appearance of secondary and tertiary lobes with well defined minima between them at crystal temperatures that are significantly different from the phase-matching condition.

Although the displacement of the crystal position is considerably smaller than the Rayleigh length for the pump beam ($z_R = 77$ mm), the phase curvature of the Gaussian beam as it focuses drastically affects the output characteristics of SPDC. Within the thin-crystal approximation the two-photon wave function may be written as [Pittman *et al.* (1996)]

$$\psi(\mathbf{k}_s, \mathbf{k}_i) = \mathcal{A}\left[\omega_s(\mathbf{k}_s) + \omega_i(\mathbf{k}_i)\right] \int_{z_0-L/2}^{z_0+L/2} \mathrm{d}z \left\{ e^{i(\Delta k_z z)} e^{\frac{q(z)^2}{2\Delta \mathbf{k}_\perp}} \right\} \tag{36}$$

where z_0 is the central crystal position along the optic axis, $q(z) = \dfrac{1}{1/R(z) - i\lambda_p/\pi n_z(\lambda_p)w^2(z)}$ is the complex beam parameter, $R(z) = z\left[1 + (z_R/z)^2\right]$ is the Gaussian beam curvature, and $w(z) = w_0\sqrt{1 + (z/z_R)^2}$ is the z-dependent beam radius. It is possible to incorporate

this expression into our numerical integrator, but it requires additional computational time due to the additional integration along the z axis. This calculation will be attempted in the future.

It has been previously shown [Pittman *et al.* (1996)] that focused beams can be used to significantly alter the phase-matching conditions. This have seen to produce a spatial focusing of the pair-rate which is of interest for two-photon imaging and may be relevant for other applications.

Chapter 5.   Conclusions

The principal objectives of this thesis have been the experimental detection and rate optimization of coincident photon pairs, the experimental study of the angular distribution of the coincidences, and a comparison of the observations with the theory. We have been successful in completing these main objectives. In addition to this, we have studied the crystal temperature dependence of the pair rates, the effects on the observed distributions from collecting the light with apertures of different sizes, and have presented applied results such as the characterization of SPCM time-response and the determination of the crystal poling homogeneity, among other results.

We now briefly summarize the contents of this thesis. Chapter 1 presents a broad introduction to the field of SPDC and entangled photon pairs, while Chapter 2 develops the theory which is required for our work. The theoretical discussion includes a derivation of the quantum state of SPDC from first principles. An expression for the rate of coincident detection was presented and calculated with numerical integrations, thus obtaining results that were compared directly with the experiments. This work is original in calculating the pair rate rigorously for actual experimental conditions, without relying on Gaussian approximations in the phase-matching function, or other simplifying assumptions (paper in preparation). The quasi phase-matching conditions have been studied and the temperature dependence of the emission angles of photon pairs has been found, which is of primary importance in experimental design.

In Chapter 3, the designs for our two main experiments are presented. These were used to observe, for the first time in CICESE, the coincident detection of entangled photon pairs. The two experiments were similar in objective, but differed in complexity. The first arrangement used a fiber tip in free-space to couple the photon-pairs into the detectors, while the second arrangement used lenses and irises to increase the observed rates and evaluate solid-angle integration effects. The second system has produced observed pair-rates of over 80,000 pairs per second. Coincidence logic and pulse counting is performed with NIM modules that are controlled through computer interfacing. The accidental coincidences are monitored to be subsequently removed from the observation. These experiments are notable in that they were performed with a single-frequency laser.

This allowed observation of the underlying phase-matching function. PPKTP was used as the nonlinear optical crystal, which produces photon-pairs with high efficiency.

Chapter 4 presents the main results and discussion of this thesis. Single-photon and two-photon distributions are shown as a function of crystal temperature and signal detector polar angle. The comparison of these results with the numerical calculations showed excellent agreement in all cases. The observation of crystal-temperature dependent oscillations in the rates was discussed and was seen to originate in a classical interference effect of the pump beam. A comparison of the angular position of peak emission with the quasi phase-matching temperature tuning curves was performed and good agreement was found. Measurements with the pump laser in two-frequency operation were presented, where the results are seen to be markedly different from those observed with the laser in single-frequency operation. An application to test the homogeneity of the crystal poling structure was presented. This is achieved by monitoring pair rates as the crystal is displaced transverse to the pump beam. Finally, a measurement with the crystal displaced from the beam waist along the optic axis was shown, which allowed for clear observation of second and third-order phase-matching lobes.

Appendix A contains an analysis of the single-photon counting modules. The analysis experimentally compares the performance of our two detectors, and presents techniques which are useful in their characterization. A saturation of the rate of coincident detection was identified as an effect due to the rate-dependent timing accuracy of the passively quenched detector and a correction method for this pair-rate saturation was presented with test results that demonstrated its performance.

Appendix B is concerned with the characterization and accurate removal of accidental coincidences. An analytic model from probability theory was derived which reproduced the main features of the observations and provides justification for our method of removal of accidentals. Two experimental methods for monitoring of the accidentals are discussed and results are presented for the two methods.

Appendix C contains a detailed collection of pair-detection results which have been observed with the Mk-II experiment.

Regarding the outlook and future work, we note that the availability of entangled quantum systems presents a variety of possibilities for applications that come with great challenges for the experimentalist. One of the possibilities that could be performed with suitable modifications in our optical system is bi-photon spectroscopy [Yabushita and Kobayashi (2004), Kalachev *et al.* (2007)]. Further possibilities include security-related applications, where the field correlations can be used to test the identity or authenticity of a sample.

Of theoretical interest is the detailed study of the coherence properties of the SPDC field with the pump laser in two-frequency operation. Also, the distributions for non-degenerate photon pairs can be theoretically studied with small modifications to our numerical integrator, while the experimental observations can be readily performed with our system with adequate filtering.

In conclusion, this work represents one of several steps that the Quantum Optics Laboratory has recently taken for moving towards the local development of SPDC-based quantum-technology. Continuity of this work is necessary for the development of applications of general interest.

Bibliographical References

Barbosa, G. (1996). Quantum images in double-slit experiments with spontaneous down-conversion light. *Physical Review A*, **54**(5): 4473.

Born, M. and Wolf, E. (1999). Principles of Optics (7th ed). *Cambridge University*. 985 pp.

Brida, G., Castelletto, S., Novero, C., and Rastello, M. (1998). Measurement of the quantum efficiency of photodetectors by parametric fluorescence. *Metrologia*, **35**(4): 397.

Brida, G., Degiovanni, I., Genovese, M., Migdall, A., Piacentini, F., Polyakov, S., and Ruo Berchera, I. (2011). Experimental realization of a low-noise heralded single-photon source. *Optics express*, **19**(2): 1484–1492.

Brooks, R. A., Sank, V. J., Di Chiro, G., Friauf, W. S., and Leighton, S. B. (1980). Design of a high resolution positron emission tomograph: the neuro-pet. *Journal of computer assisted tomography*, **4**(1): 5–13.

Burnham, D. C. and Weinberg, D. L. (1970). Observation of simultaneity in parametric production of optical photon pairs. *Physical Review Letters*, **25**(2): 84.

Cova, S., Ghioni, M., Lacaita, A., Samori, C., and Zappa, F. (1996). Avalanche photodiodes and quenching circuits for single-photon detection. *Applied optics*, **35**(12): 1956–1976.

Denny, M. (2001). Introduction to importance sampling in rare-event simulations. *European Journal of Physics*, **22**(4): 403.

Dirac, P. A. M. (1930). *The principles of quantum mechanics*. Oxford University Press. 300 pp.

Emanueli, S. and Arie, A. (2003). Temperature-dependent dispersion equations for $KTiOPO_4$ and $KTiOAsO_4$. *Applied optics*, **42**(33): 6661–6665.

Erven, C., Couteau, C., Laflamme, R., and Weihs, G. (2008). Entangled quantum key distribution over two free-space optical links. *Optics express*, **16**(21): 16840–16853.

Fejer, M. M., Magel, G., Jundt, D. H., and Byer, R. L. (1992). Quasi-phase-matched second harmonic generation: tuning and tolerances. *Quantum Electronics, IEEE Journal of*, **28**(11): 2631–2654.

Feller, W. (1950). *An Introduction to Probability Theory and Its Applications: Volume One*. John Wiley & Sons. 461 pp.

Fishman, G. S. (1996). *Monte Carlo: Concepts, Algorithms, and Applications*. Springer. 698 pp.

Fox, M. (2006). *Quantum Optics: An Introduction*. Oxford University Press. 400 pp.

Fradkin, K., Arie, A., Skliar, A., and Rosenman, G. (1999). Tunable midinfrared source by difference frequency generation in bulk periodically poled ktiopo4. *Applied physics letters*, **74**(7): 914–916.

Franson, J. (1992). Nonlocal cancellation of dispersion. *Physical Review A*, **45**(5): 3126.

Friberg, S., Hong, C., and Mandel, L. (1985). Measurement of time delays in the parametric production of photon pairs. *Physical review letters*, **54**(18): 2011.

Glauber, R. J. (1963). The quantum theory of optical coherence. *Physical Review*, **130**(6): 2529.

Gurzadyan, G. G., Dmitriev, V. G., and Nikogosyan, D. N. (1991). *Handbook of Nonlinear Optical Crystals*. Springer-Verlag. 414 pp.

Hamar, M., Peřina Jr, J., Haderka, O., and Michálek, V. (2010). Transverse coherence of photon pairs generated in spontaneous parametric down-conversion. *Physical Review A*, **81**(4): 043827.

Holstein, B. R. (1992). *Topics in Advanced Quantum Mechanics*. Addison Wesley. 436 pp.

Hong, C. and Mandel, L. (1985). Theory of parametric frequency down conversion of light. *Physical Review A*, **31**(4): 2409.

Hong, C., Ou, Z., and Mandel, L. (1987). Measurement of subpicosecond time intervals between two photons by interference. *Physical Review Letters*, **59**(18): 2044.

Joobeur, A., Saleh, B. E., and Teich, M. C. (1994). Spatiotemporal coherence properties of entangled light beams generated by parametric down-conversion. *Physical Review A*, **50**(4): 3349.

Joobeur, A., Saleh, B. E., Larchuk, T. S., and Teich, M. C. (1996). Coherence properties of entangled light beams generated by parametric down-conversion: Theory and experiment. *Physical Review A*, **53**(6): 4360.

Kalachev, A., Kalashnikov, D., Kalinkin, A., Mitrofanova, T., Shkalikov, A., and Samartsev, V. (2007). Biphoton spectroscopy of yag: Er3+ crystal. *Laser Physics Letters*, **4**(10): 722–725.

Khosrofian, J. M. and Garetz, B. A. (1983). Measurement of a gaussian laser beam diameter through the direct inversion of knife-edge data. *Applied Optics*, **22**(21): 3406–3410.

Klyshko, D. (1980). Use of two-photon light for absolute calibration of photoelectric detectors. *Soviet Journal of Quantum Electronics*, **10**(9): 1112.

Klyshko, D. (1988). Combine epr and two-slit experiments: Interference of advanced waves. *Physics Letters A*, **132**(6): 299–304.

Malygin, A., Penin, A., and Sergienko, A. (1985). Spatiotemporal grouping of photons in spontaneous parametric scattering of light. In: *Sov. Phys. Dokl*. Vol. 30, pages 227–229.

Mandel, L. and Wolf, E. (1995). *Optical coherence and quantum optics*. Cambridge university press.1166 pp.

Marcikic, I., Lamas-Linares, A., and Kurtsiefer, C. (2006). Free-space quantum key distribution with entangled photons. *Applied Physics Letters*, **89**(10): 101122.

Ou, Z., Wang, L., and Mandel, L. (1989). Vacuum effects on interference in two-photon down conversion. *Physical Review A*, **40**(3): 1428.

O'Donnell, K. A. (2011). Observations of dispersion cancellation of entangled photon pairs. *Physical Review Letters*, **106**(6): 063601.

Pittman, T., Strekalov, D., Klyshko, D., Rubin, M., Sergienko, A., and Shih, Y. (1996). Two-photon geometric optics. *Physical Review A*, **53**(4): 2804.

Renker, D. (2006). Geiger-mode avalanche photodiodes, history, properties and problems. *Nuclear Instruments and Methods in Physics Research Section A: Accelerators, Spectrometers, Detectors and Associated Equipment*, **567**(1): 48–56.

Römer, H. (2006). *Theoretical optics*. John Wiley & Sons. 375 pp.

Romero Sánchez, E. R. (2013). *Desarrollo de una nueva fuente altamente eficiente de parejas de fotones entrelazados*. Masters thesis, Centro de Investigación Científica y de Educación Superior de Ensenada.

Rubinstein, R. Y. and Kroese, D. P. (2011). *Simulation and the Monte Carlo method*, Vol. 707. John Wiley & Sons.

Sakurai, J. J. and Tuan, S. F. (1985). *Modern Quantum Mechanics*, Vol. 1. Addison-Wesley Reading, Massachusetts. 500 pp.

Sergienko, A. (2001). Quantum metrology with entangled photons. In: *Recent Advances in Metrology and Fundamental Constants*. Vol. 1, page 715.

Shankar, R. (1994). *Principles of quantum mechanics*, Vol. 233. Plenum Press New York. 612 pp.

Shih, Y. and Alley, C. O. (1988). New type of einstein-podolsky-rosen-bohm experiment using pairs of light quanta produced by optical parametric down conversion. *Physical Review Letters*, **61**(26): 2921.

Strekalov, D., Sergienko, A., Klyshko, D., and Shih, Y. (1995). Observation of two-photon "ghost" interference and diffraction. *Physical Review Letters*, **74**(18): 3600.

Wang, S., Pasiskevicius, V., Laurell, F., Karlsson, H., *et al.* (1999). First-order type ii quasi-phase-matched uv generation in periodically poled ktp. *Optics letters*, **24**(14): 978–980.

Yabushita, A. and Kobayashi, T. (2004). Spectroscopy by frequency-entangled photon pairs. *Physical Review A*, **69**(1): 013806.

Zel'Dovich, B. Y. and Klyshko, D. (1969). Field statistics in parametric luminescence. *ZhETF Pisma Redaktsiiu*, **9**: 69.

Appendix A. On the behavior and characterization of SPCMs

In this appendix, we present a discussion of the single-photon counting modules (SPCMs) with a focus on how coincident photon pairs can be used in their characterization. Basic aspects of photon counting are introduced in Section A.1. The two most common designs for the so-called quenching of the SPCMs are introduced in Subsection A.1.1. Section A.2 presents the method for the characterization that was performed, as well as the results. The single-photon counting linearity evaluation is shown on Subsection A.2.1, while the evaluation of pair rate linearity is presented on Subsection A.2.2. Finally, a method for correcting pair rate saturation along with an evaluation of this method is presented in Section A.3.

A.1 SPCMs: Photon-Counting and timing accuracy

Most photo-detection methods obscure the quantum nature of light to the point where no evidence of a single-photon impulse response can be observed. Photon counting is different since it deals with signals composed of pulses, each of which is the record of a photon arrival with a temporal resolution of fractions of a nanosecond.

The development of vacuum photo-diodes and photo-multipliers provided the first means of detecting single photons with efficiencies of approximately 10%. These detectors produce an electric pulse that is associated with the annihilation of a single quantum of light. The development of SPCMs and the laser have led to the study of the statistical properties of light and thus have opened the door to the study of what is now known as quantum optics.

A.1.1 Avalanche diodes for photo-detection: Passive and active quenching

Research on semiconductor devices for light detection during the 1990s produced the Geiger-mode avalanche photo-diode, also known as the Single-Photon Avalanche Diode (SPAD). This device is the state of the art for performing light detection at extremely low levels [Cova *et al.* (1996)]. It consists of a reverse-biased avalanche photo-diode well

above the breakdown voltage (Geiger-mode). In this condition, transport of a single charge carrier from the valence to conduction band of the crystal structure will trigger a charge-carrier avalanche. This macroscopic discharge triggers electronic comparators to produce a standard output pulse that is used in later circuits.

Once the avalanche has occurred, there is a characteristic amount of time during which the charge carriers are replenished, and only later may the device respond to an incoming photon. If the circuit provides no means for accelerating this charge-carrier replenishment, then the circuit is called *passively quenched* (PQ). If, however, there are components within the electronic circuit designed to inject charge carriers back into the APD, then the circuit is said to be *actively quenched* (AQ).

Modern SPADs are used in the construction of Single-Photon Counting Modules (SPCM) that have nanosecond or sub-nanosecond timing resolution, counting efficiencies of over 80%, a maximum detection rate of over 10^7 photons per second and a dark count rate of less than 10 photons per second [Renker (2006)].

The sub-nanosecond timing accuracy of the detectors is not enough to resolve the temporal structure of the photon-pair wave function. Recent experiments [O'Donnell (2011)] have observed this fine structure through the use of up-conversion of the entangled photon-pairs, producing temporal resolution at the femtosecond level. This method, however, requires a much larger flux of pairs.

A.2   SPCM characterization with photon pairs

Depending on their design characteristics and individual quality, SPCMs can suffer from different undesired effects. They may present saturation effects which include a rate-dependent timing accuracy and a non-linearity in the rate of photon detection. It is important to know the characteristics of the SPCMs that are available, as these will help identify some limitations on their use along with the performance that can be expected. A complete understanding of the detectors' response to varying power levels can also be used to provide methods for correcting undesired effects accurately, as will be shown in Section A.3.
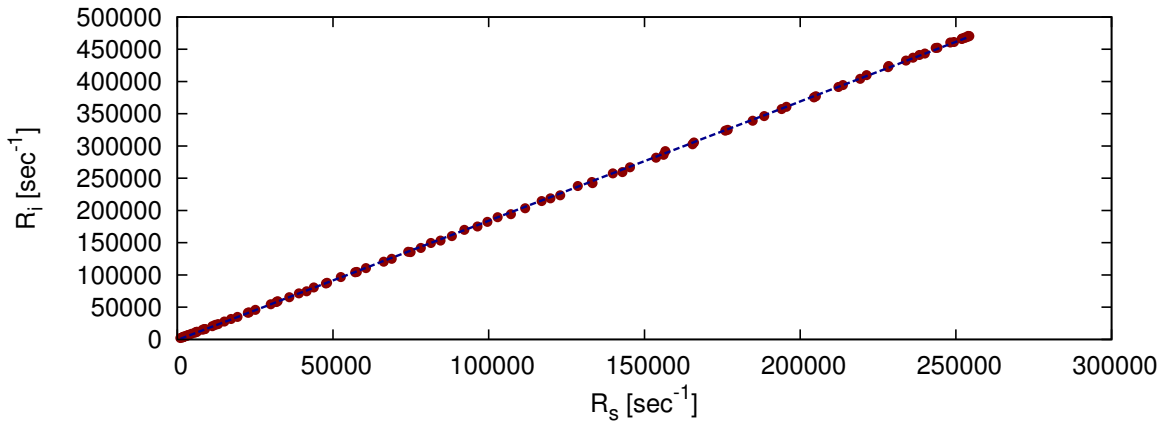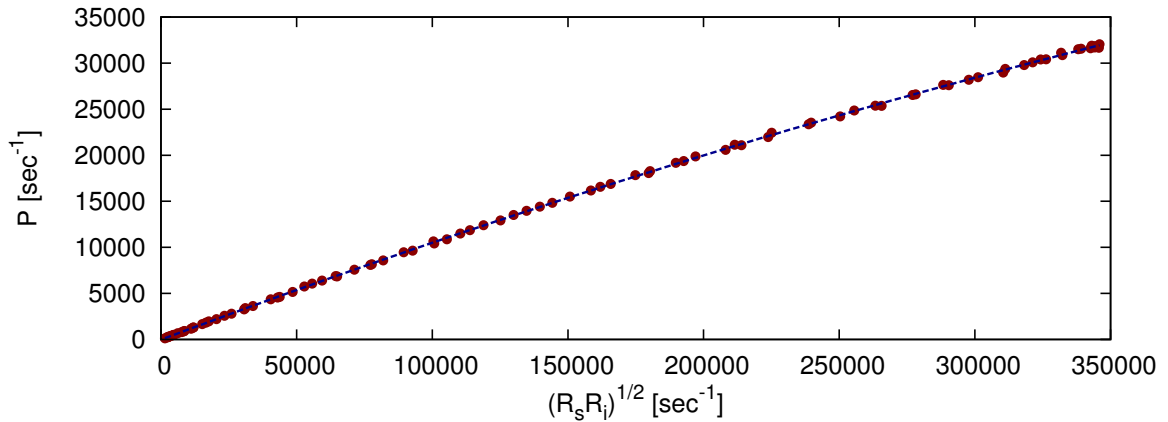
Figure 37: Measured rate of idler photons R_i (filled circles) as a function of the signal photon rate R_s. The observations are approximated by a least squares fit of a linear function (dashed line).

A.2.1 Single-photon counting linearity

The detectors were tested to compare their performance and achieve accurate measurements. The availability of a source of time-correlated entangled photon pairs and the electronic delayed-coincidence detection facilities were used for an evaluation of the timing accuracy of the detectors. The power control on the pump source and the aperture controls on the fiber-coupling input were used to control the amount of saturation in each detector.

With the Mk-II experiment (described in Section 3.4.2) aligned at a polar angle of $2.5°$, the pump power was varied while measuring the photon rates of both detectors, the rate of coincidences and the accidental live correction channel (a desynchronized coincidence detection logic unit, described in Appendix B).

We compared the photon-count rates from the two SPCMs with the apertures fully open and set the pump to maximum power to produce the highest photon rates available. The result from this test can be seen in Fig. 37. The linear relationship between the two rates is consistent with both two unsaturated detectors and two equally saturated detectors. This last possibility is discarded since AQ and PQ detection circuits are known to present significantly different rates of saturation from the manufacturer's specification. Thus, no corrections where deemed necessary in the determination of the singles at these signal levels.

Figure 38: Measured rate of pair detection P (filled circles) as a function of the geometric mean of the signal and idler photon rates $(\mathrm{R_iR_s})^{1/2}$. The observations are well approximated by a quadratic polynomial (dashed line).

A.2.2   Photon-pair detection and timing accuracy

Figure 38 shows the dependence of the rate of photon pair detection as a function of the geometric mean of detected signal and idler photons $(R_sR_i)^{1/2}$. This plot uses data from the same measurement which provided Fig. 37, with both apertures at 5 mm diameter.

As it is seen, this measurement presents a downward deviation from linearity which is well approximated with a quadratic term. The following is a description of a series of tests designed to reveal just how the two detectors can have a completely linear relationship in their rates of photon detections while producing a strongly nonlinear behavior in the rate of pair detection.

A.2.2.1   Isolating the saturation with asymmetric apertures

From the first observation of the pair rate saturation, its origin was suspected to lay in the rate-dependent timing accuracy which has been observed in PQ detectors [Cova *et al.* (1996)]. The following experiment was designed to determine if this was the case, i.e. whether the pair rate saturation was the sole effect of a single detector and, more specifically, whether the PQ detector's count rate could be used to correct this non-linearity. To induce saturation in only one of the detectors, the aperture diameters on the signal and idler channels were set unequally (with equal polar angle on both arms).

In the first asymmetric configuration, the transmission aperture on the signal channel
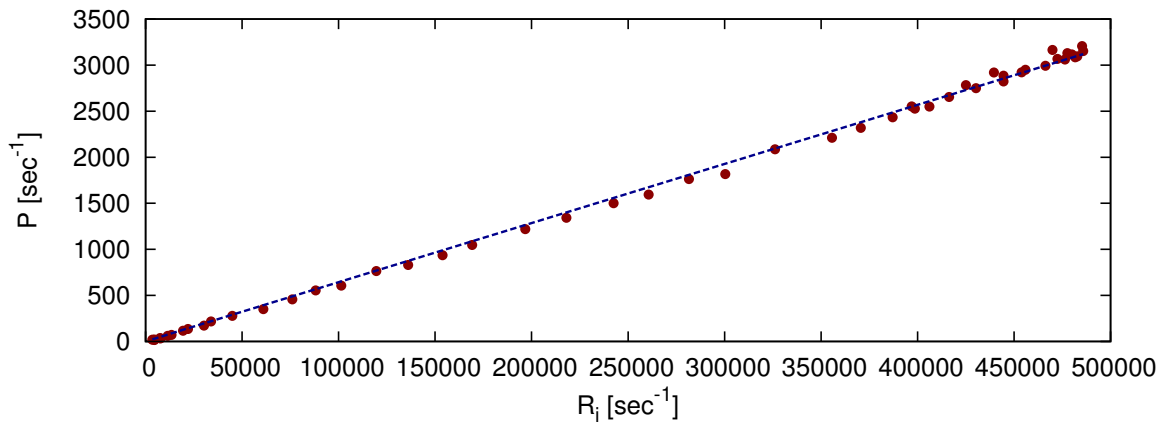
Figure 39: Measured rate of pair detection P (filled circles) as a function of the idler photon rate R_i. The idler aperture has a 5 mm diameter and the signal aperture has a 1 mm diameter. The dashed line is a least squares fit of a linear function.

was reduced to less than 1 mm diameter, while the aperture of the idler channel was set to 5 mm. The rate of photon detection in the signal detector was a 16th (16400 s^{-1}) of its value under maximum power, preventing the slower PQ detector (on the signal arm) from introducing any significant non-linearities in the result.

As Fig. 39 shows, there is a linear relationship between the accidental-corrected pairs (see Appendix B) with respect to the number of detected photons in the idler detector. We conclude that the AQ detector is not the cause of the pair rate saturation and is well-suited to work as a high-photon-rate detector.

The aperture settings were then inverted (leaving the signal aperture completely open, and reducing the idler aperture to less than 1 mm diameter). In this case the observed relationship is, to a good approximation, a quadratic polynomial as shown in Fig. 40. This is the same general nonlinear behavior as observed in Fig. 38. This result confirms that the pair rate saturation is caused by the PQ detector and allows us to consider only the rate of photon detection in the signal channel in correcting the saturation of the pair rates, as will be shown in Section A.3.

A.2.2.2 Timing accuracy

With the experimental conditions described above, the rate of coincidences was observed while varying the delay of the idler channel τ. This allows us to study the timing accuracy
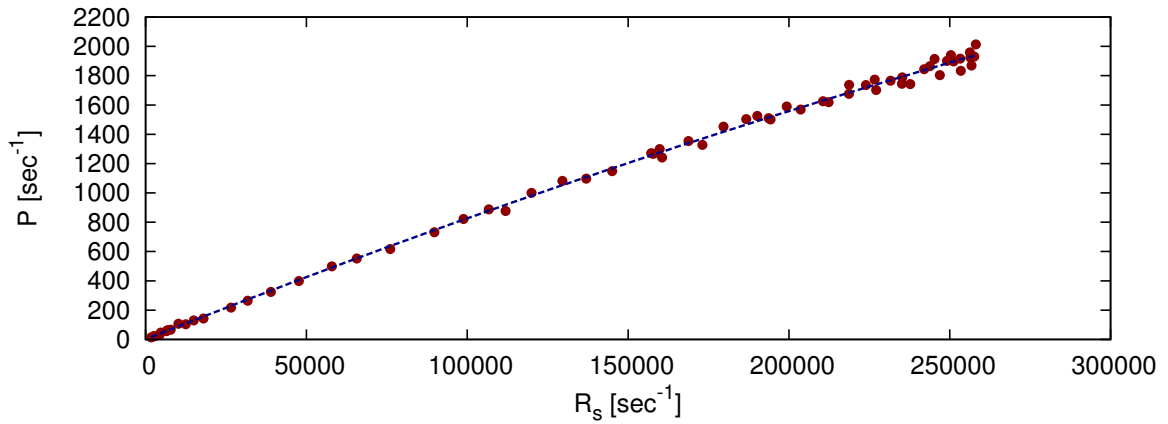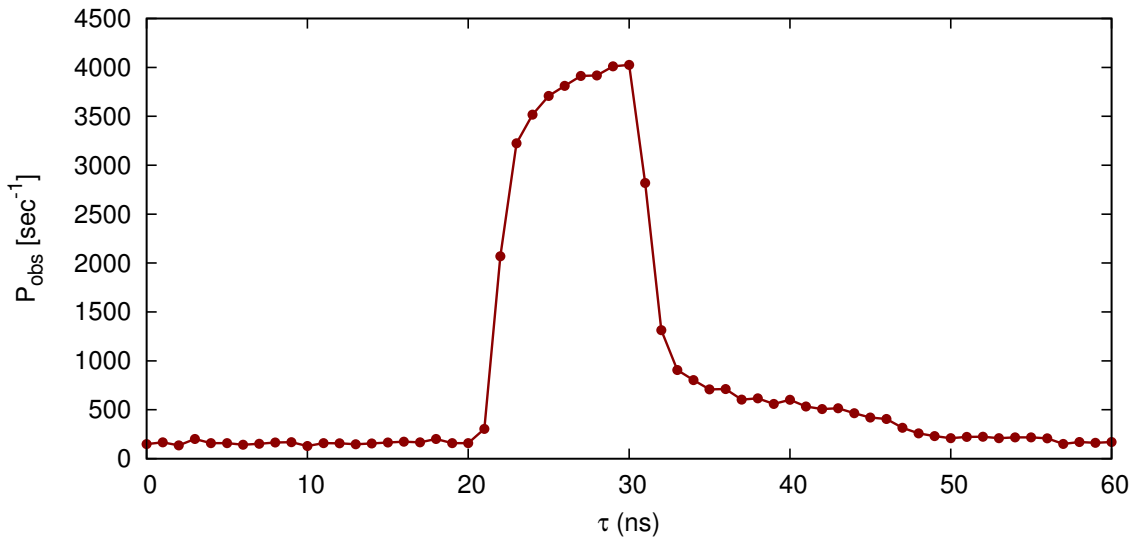
Figure 40: Measured pair rate P **as a function of the rate of single photon detection in the signal channel** R_s**. The signal aperture has a 5 mm diameter, the idler aperture has a 1 mm diameter.**
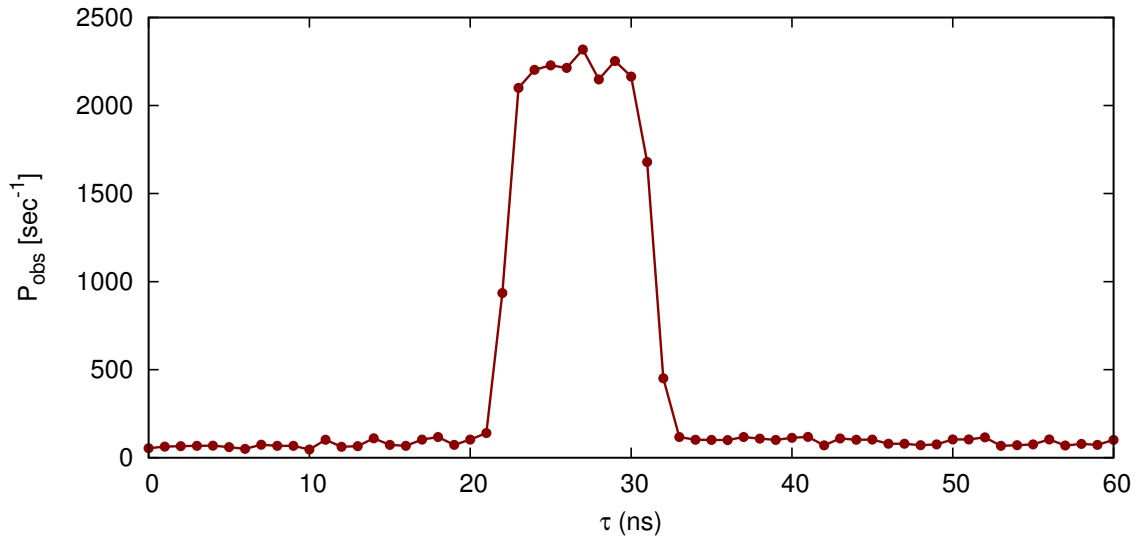
Figure 41: Measured rate of coincidences P_{obs} **as a function of idler delay** τ**. The signal aperture has a 1 mm diameter, the idler aperture has a 5 mm diameter.**

of the photo-detection process and how it affects the rate of coincidences.

We first used a 5 mm aperture in the idler channel and a 1 mm aperture for the signal channel. Figure 41 shows that, as τ is varied, the pairs present a symmetric boxcar distribution on top of a constant noise-floor made up of randomly coincident events. As can be seen, there are some data points which are halfway between the background and the maximum, producing a rise time of about 1 ns around the boxcar distribution. This is an indication that the timing accuracy of the system is close to 0.5 ns with these conditions.

Figure 42: Measured rate of coincidences $\mathrm{P_{obs}}$ as a function of idler channel delay τ. The idler aperture has a 1 mm diameter and the signal aperture has a 5 mm diameter.

We then used a 5 mm aperture in the signal channel and a 1 mm aperture for the idler channel. The result, shown in Fig. 42, is strikingly different from both the idler-saturated delayed-coincidence detection, and the response from the coincidence detection system that was previously shown in Fig. 13. The time-distribution of the photon pairs does not present a flat region, it is non-symmetric and, in fact, presents a long tail which is observable at delays of over 50 ns. The tail of the distribution presents a step-like tail with noticeable drops at 46 ns and 56 ns.

With this observation, the nature of the saturation that the PQ detector experiences becomes clear. As the rate of photo-detection is increased, the probability that two photons will be detected in close succession increases. In PQ devices, the charge-carrier replenishment process may take over 50 ns [Cova *et al.* (1996)]. During the replenishment period, the SPCM may be triggered again, but this will produce a pulse of reduced intensity (as only a fraction of the charge carriers are available for the avalanche). The weak pulse may trigger the comparator with a random delay as compared with a pulse of regular intensity. This delay can be easily understood if one considers that two identically-shaped pulses will trigger the comparator at different heights relative to the maximum intensity of the pulse (the weak pulse will trigger at a higher relative height) and this height-difference corresponds to the delay.

A.3   Correcting the pair rate saturation

The experimental result of Fig. 40 approximates a second order polynomial. This can be used to recover the correct pair rates. The observed rate of coincident detection P_{obs} is written as an explicit function of the observed rate of signal photon detection R_s as

$$P_{\mathrm{obs}}(R_s) = aR_s + bR_s^2, \tag{37}$$

where a and b are constants relating to the experimental conditions. Equation (37) can be formally derived by considering the Poissonian statistics of the photo-detection process. The calculation is similar to that which is described in Section B.1.2. The rate of entangled photon-pairs is given by $P = aR_s$. Having determined empirically the quotient $\frac{b}{a}$, the entangled pair rate can be obtained from the observed pairs by the relationship

$$P(R_s) = \frac{P_{\mathrm{obs}}}{1 + \frac{b}{a}R_s}, \tag{38}$$

which can be derived from Eq. (37) by factorization.

In order to test the performance of this correction, the Mk-II experiment was aligned for coincidence detection at a polar angle of $2.3°$ and two temperature scans were measured at different levels of pump power. The first scan used the maximum power, while in the second scan the pump power was reduced to about a fourth of the maximum.

To compare the two measurements fairly, the measured rates of pairs P_{obs} were divided by the maximum rate of signal photons in the signal channel for each scan R_i^{max}. Figure 43 shows the results after this linear scaling has been applied. It is seen that the temperature scan with full power presents a clear saturation in the regions of high flux when compared with the scan at a quarter of full power. Figure 44 shows the results after introducing the correction defined by Eq. (38). Agreement is found between these two curves and we conclude that the correction method works as intended.
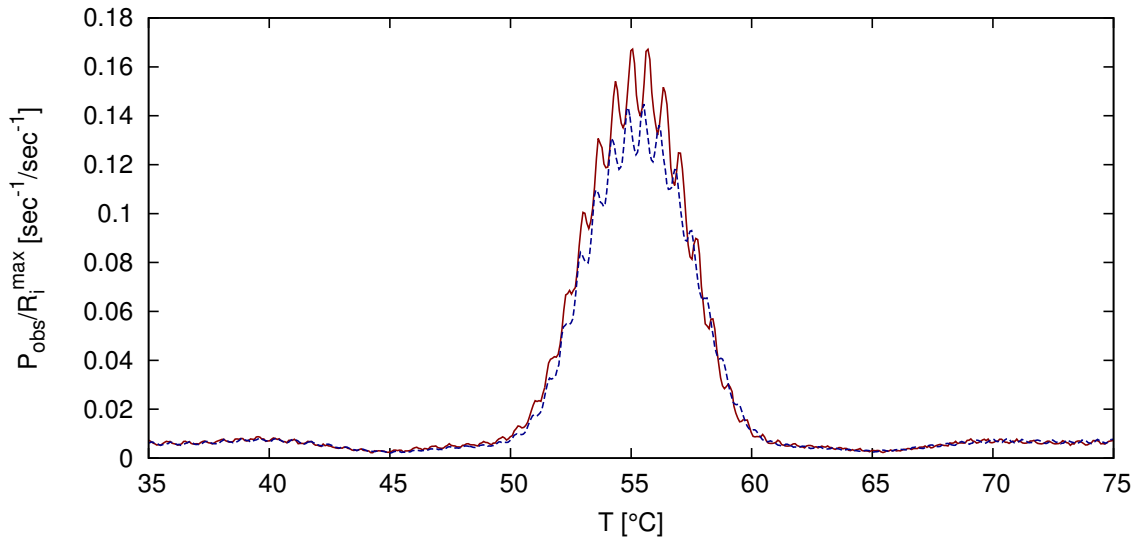
Figure 43: Normalized observed rate of pair detection $\mathrm{P_{obs}}/\mathrm{R_i^{max}}$ at full pump power (22 mW, dashed line) and one quarter pump power (5.5 mW, solid line). The individual data points are not shown, for clarity. Both apertures are set to 5 mm.
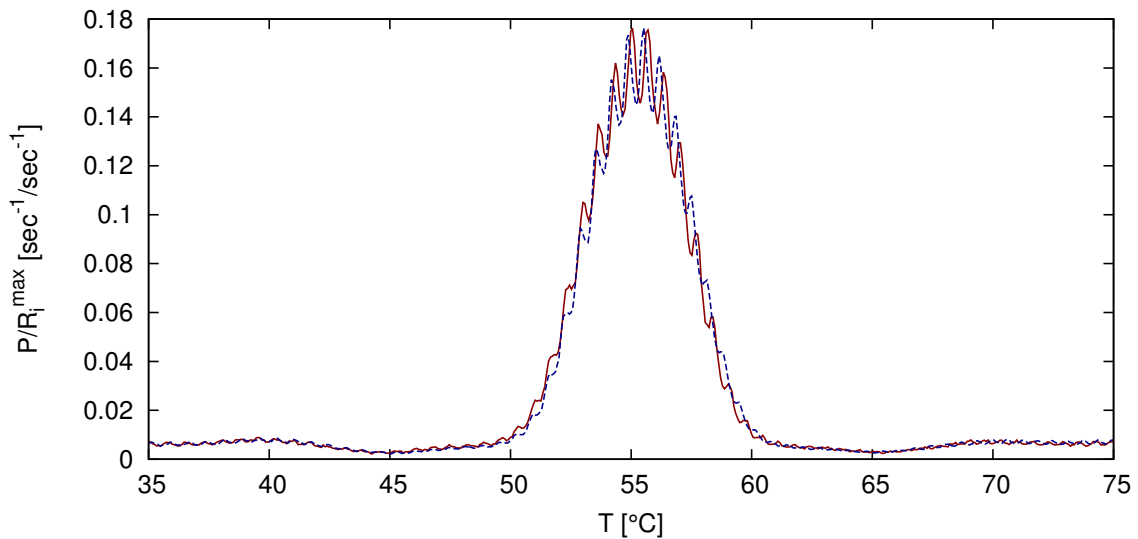
Figure 44: Normalized corrected rate of pair detection $\mathrm{P}/\mathrm{R_i^{max}}$ as a function of temperature T at full pump power (22 mW, dashed line) and one quarter pump power (5.5 mW, solid line). The individual data points are not shown, for clarity. Both apertures are set to 5 mm.

Equation (37) shows that the contribution bR_s^2 to the pair rate from a loss of timing accuracy is proportional to the square of the photo-detection rate in the signal detector. A reduction in the pump power by a factor of 4 will reduce the rate of photon-pair detection by the same factor, increase the expected measurement error by a factor of 2 (from the Poisson distribution of the pair rate), and reduce the amount of correction due to loss of timing accuracy by a factor of 16. Then, the use of a lower pump power may yield an actual benefit in that the required corrections can be reduced by a large amount with relatively little increase in measurement error due to the underlying Poisson process.

Appendix B. Removal of false-pair detection events

This appendix is concerned with the accidental coincident detection of photons that are not members of the same photon-pair. This effect can seen at high signal levels such as those found in the Mk-II experiment. A description of these randomly-coincident photo-detections is presented in Section B.1. This includes a quantitative description of these events, and a comparison of numerical simulations based on these results with experimental observations. Finally, Section B.2 presents two methods for the removal of this undesired effect.

B.1 The origin and nature of the accidentals

B.1.1 Poisson processes in photo-detection

Considering the response time limitations of modern SPCMs, the photo-detection events from SPDC light occur randomly in time [Mandel and Wolf (1995)]. This is, the pulses that are emitted due to the incidence of photon pair members in the detectors are independent and identically distributed in time (IID). Random counting processes which are i.i.d. are known as Poisson processes [Feller (1950)]. The probability $P(n,t)$ of counting n photons in a measuring time t is then given by the Poisson distribution

$$P(n,t) = \frac{e^{-\alpha t}(\alpha t)^n}{n!},\tag{39}$$

where α is the photon rate. It is straightforward to prove that $\langle n \rangle = \alpha t$.

In the case of our experiments, the rate of incident photons on detector j is $\alpha_j = R_j^{\mathrm{inc}}$. This rate may be written as $R_j^{\mathrm{inc}} = S_j + P_j$ where $(S_j + P_j)$ is equal to the total rate of incident photons. A member of a photon pair incident on the s detector contributes to P_s only if its corresponding pair member is coupled into detector i. All other coupled photons are considered to contribute to S_j. Of course, this distinction is only possible in thought experiments or numerical calculations. This is to avoid introducing the optical coupling efficiency into our expressions. Thus, we have that $P_s = P_i = P$ and the rate of incident

photons on detector j may be written in general as

$$R_j^{\text{inc}} = S_j + P. \tag{40}$$

When the detectors are aligned to equal angles and aperture sizes, as is the case for the temperature scans presented in Chapter 4, then the rate of incident photons is the same on both arms $R_s^{\text{inc}} = R_i^{\text{inc}} = R$ and, from Eq. (40), $S_s = S_i = S$. Then for these conditions we have that

$$R = S + P \tag{41}$$

for both of the signal and idler channels. Other configurations of detector angles and apertures require the values of S_j and P to be computed numerically or estimated by other means.

B.1.2 Synchronized and desynchronized coincidence detection rates

Consider the case of equal detection angles and apertures so that Eq. (41) holds. The two detectors are independent and the probability for detecting an incident photon on the j-th detector is its efficiency η_j. Then, the probability that the two members of a single photon pair are detected by our arrangement is the product of the two detection efficiencies $\eta_s \eta_i$ and the observed rate of photon pairs P^{obs} must include a contribution from actual time-correlated photons that is equal to $\eta_s \eta_i P$. This linear response in the coincidence detection system to the rate of entangled photon pairs corresponds to the ideal behavior.

For a Poisson process, the probability distribution for the waiting time τ is given by an exponential distribution of the form [Feller (1950)]

$$\rho(t) = \alpha e^{-\alpha t}. \tag{42}$$

It can be shown that the mean time between arrivals is given by $\tau = \frac{1}{\alpha}$. Because the mean waiting time τ for a detection event is inversely proportional to the rate of detection R and the pulses have a finite width Δt, then at high rates there will be a probability of coincidence detection for photons which do not come from the same pair. In the literature these false-pair detection events are called accidentals. This contribution will be observed

in addition to the events from actual detection of the coincident photon pairs.

The contribution to P^{obs} from accidentals may be calculated as follows. Given that a detection event on the signal arm is statistically independent from a detection event in the idler arm, then the rate of random coincidence detection is the product of the the signal detection rate $R_s = \eta_s R = \eta_s(S + P)$ times the probability that a photon is detected in a measurement of time $2\Delta t$ on the idler detector (or vice versa), where $\Delta t = \Delta t_{\mathrm{pulse}} + \Delta t_{\mathrm{min}}$ is the sum of the pulse width plus the minimum overlap required by the coincidence detection logic unit. This last probability is calculated by integrating the waiting time distribution of Eq. (42) and considering the detection efficiency as

$$
\begin{align}
P(-\Delta < t < \Delta t) &= \eta_i \int_{-\Delta t}^{\Delta t} (S + P)e^{-(S+P)t}\mathrm{d}t \tag{43}\\
&= \eta_i(-e^{-(S+P)\Delta t} + e^{(S+P)\Delta t}) \tag{44}\\
&\approx 2\eta_i\,(S + P)\,\Delta t, \tag{45}
\end{align}
$$

where the last equation results from a Taylor series approximation to first order. By multiplying the signal rate by the right hand side of Eq. (45), we find that the rate of accidentals equals $2\eta_s\eta_i\Delta t(S + P)^2$.

Then, for the case of two detectors synchronized for photon pair detection we have that the observed coincidence rate is given by

$$
P_{\mathrm{obs}}^{\mathrm{synced}} = \eta_s\eta_i\left(P + 2\Delta t(S + P)^2\right), \tag{46}
$$

while for the case of two desynchronized detectors we have

$$
P_{\mathrm{obs}}^{\mathrm{desynced}} = \eta_s\eta_i 2\Delta t(S + P)^2. \tag{47}
$$

The following are good approximations for our experimental values: $\Delta t = 6$ ns, $\eta_1\eta_2 \approx 0.045$, $P_{\mathrm{max}} \approx 1.2 \times 10^6$ s^{-1} and $(S + P) \approx 2 \times 10^6$ s^{-1}. With these values, we can predict from Eq. (46) a total amount of observed pairs per second of about 54000, while from Eq. (47) we can expect a coincidence rate due to accidentals of approximately 2500. These quantities are comparable to observations from the Mk-II experiment where, at

high photon rates, the synchronized coincidence detection channel measured a rate of 47187 coincidences per second, while the accidental correction channel observed 2523 coincidences per second.

### B.1.3 Simulating the coincidence-detection process

To test the consistency of the theory and the experimental observations we developed a simulation of the detection, pulse-processing and coincidence discrimination systems. The simulation uses an exponential random number generator for the waiting time between photon arrivals and accounts for detector efficiency, dead time, output lag, pulse length and the minimum pulse overlap that is required by the logic gate for coincidence detection. The rate-dependent timing accuracy of the PQ detector, described in Section A.2.2.2, was not considered as it is not needed for the main features of the observations to be reproduced.

The calculated rates are estimated from one second. The experimental rates represent an average from two consecutive 1 s measurements. The results from the simulation were compared with the experiment at two different synchronization configurations.

The first configuration has detectors which are synchronized for photon pair detection, this is achieved with a 30 ns delay on the idler channel. Figure 45 shows the result for this case. Although both the simulation and the experiment present a downward quadratic deviation from linearity, the deviation is much stronger in the experimental case. This is attributed to the rate-dependent timing accuracy of the PQ detector which was shown to present this behavior in Fig. 40.

The second configuration has desynchronized detectors for measuring the accidentals. This does not require any delay since the detectors have very different detection-to-output times. Figure 46 shows the comparisons in this configuration. Good agreement can be seen between the numerical and experimental result, both showing the characteristic quadratic behavior of the accidentals.

This analysis has several shortcomings which prevent the direct use of these results for the accurate subtraction of the accidentals. The development for an arrangement of
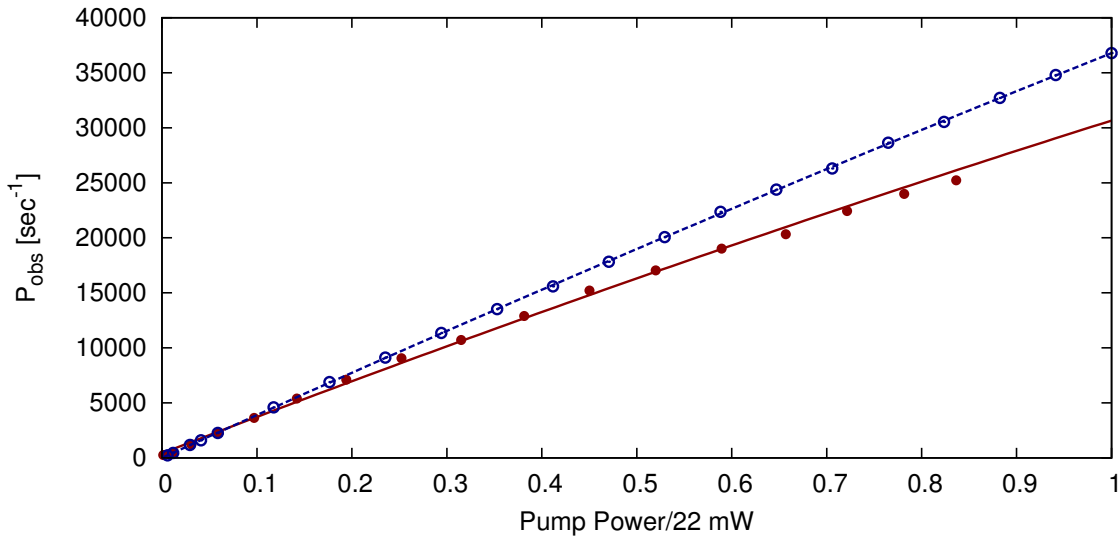
Figure 45: Rate of observed coincidences P_{obs} as a function of pump power (normalized to 22 mW) for a synchronized detection experiment (filled circles) and data from a numerical simulation (open circles). The continuous lines are least-squares fits to a quadratic polynomial (solid line for the experiment, dashed for the simulation).
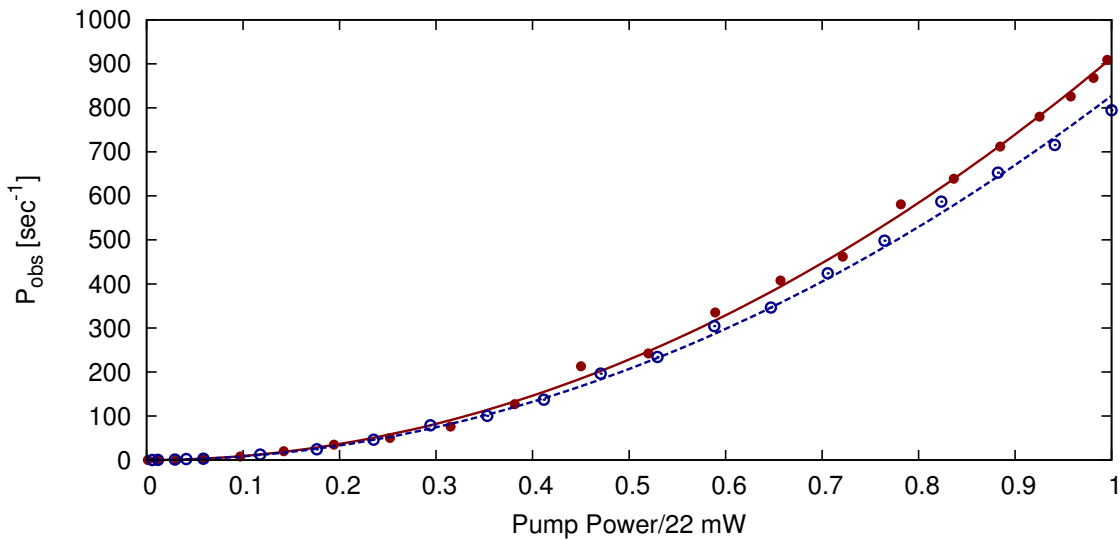
Figure 46: Rate of observed coincidences P_{obs} as a function of pump power (normalized to 22 mW) for a desynchronized detection experiment (filled circles) and data from a numerical simulation (open circles). The continuous lines are least-squares fits to a quadratic polynomial (solid line for the experiment, dashed for the simulation).

equal polar angles and apertures is not useful when studying the angular distribution of the pairs. Additionally, the determination of the exact experimental conditions is difficult and some parameters such as the one-photon SNR ratio, and the optical and quantum efficiencies for both channels may be hard to estimate. Finally, the photon-pairs are observed along with a distribution of light of unknown origin, a so-called polarization dependent fluorescence, which has a nontrivial angular and temperature distribution. Considering the previous reasons, no attempt was made to correct for accidentals in post-processing with this model. The solution we implemented, which is described next, does not suffer from any of these shortcomings.

B.2   The removal of accidentals

Equations (46) and (47) suggest a technique for removing the accidentals from our measurements. If two measurements for each desired experimental condition are made with different synchronization conditions, then subtracting the desynchronized measurement from the synchronized one yields a measurement which is free from accidentals. The corrected result is then expected to have a zero mean in observations where no photon pairs are present.

B.2.1   Two-pass correction

An experiment with the Mk-II experiment was designed to test the method. Both apertures were set to 5 mm and the pump power was set to the maximum available to produce high rates. The idler arm was set to $\theta = 2.5°$ and the crystal temperature was set to 40°C. This temperature phase-matches at approximately $\theta = 3°$ and is lower than the optimal for the observation at the $\theta = 2.5°$ by approximately 8°C.

Two consecutive polar angular scans were performed with delays on the idler channel of 30 ns and 0 ns producing synchronized and desynchronized observations, respectively. Figure 47 shows the result of these angular scans and the result of the subtraction. It can be seen that a secondary lobe in the synchronized measurement at $\theta = 3°$ was entirely composed of accidentals. The corrected result shows a well defined distribution with no secondary lobes without background.
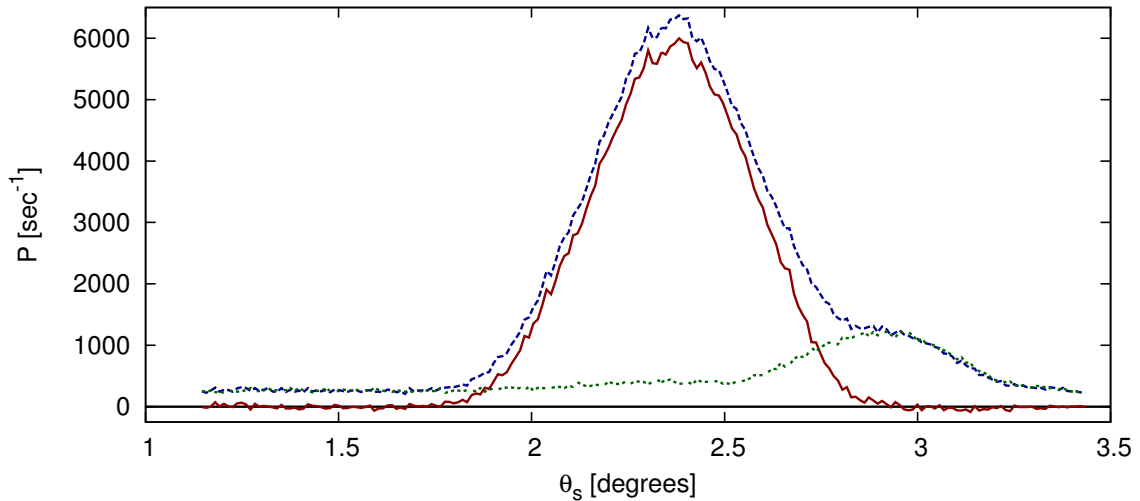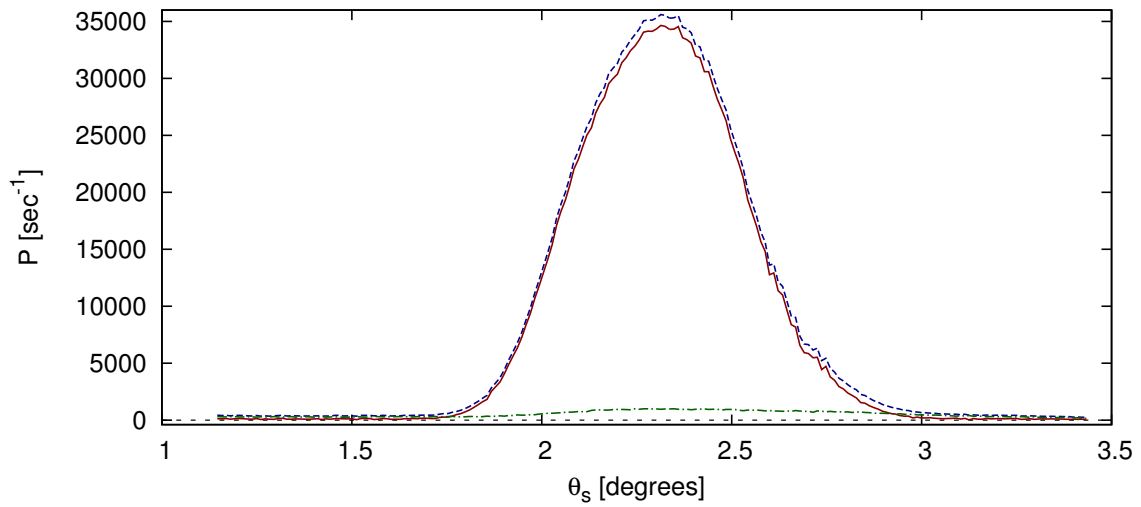
Figure 47: Rate of coincidence detection as a function of signal detection angle for synchronized detection experiment (solid line) and desynchronized experiment (dashed line). The accidental-corrected result (solid circles) is obtained by subtracting the desynchronized data from the synchronized data. The idler detector is set to $\theta = 2.5°$ and the crystal temperature is $\mathbf{T} = 40°\mathrm{C}$.

This result proves that the subtraction method for removal of accidentals works and that the two-pass method can be used successfully. However, the demands on system stability are high and some results from other tests showed evidence of laser mode-jumps or intensity fluctuations affecting the correction.

B.2.2 Live correction

The use of a second electronic counter allows for the monitoring of an additional coincidence detection logic unit. As described in Section 3.5, the two coincidence detection systems have different delays and can measure coincidences simultaneously. This is called the *live* or *real-time* monitoring of accidentals. Figure 48 shows the results from a measurement using this system. As can be seen, the accidentals form a non-constant background which is accurately removed with the simultaneous monitoring of accidentals.

The performance of the live detection system is satisfactory, the simultaneous measurement of the synchronized and desynchronized channels offers a better correspondence between the observations yielding a higher quality result. The results from Section 4.2 have all been measured with this system and the resulting entangled photon-pair rates are corrected for saturation by the method described in Section A.3.

Figure 48: Rate of coincidence detection as a function of signal detection angle for synchronized detection experiment (dashed line) and desynchronized experiment (dot-dashed line). The accidental-corrected result (solid line) is obtained by subtracting the desynchronized data from the synchronized data. The idler detector is set to $\theta = 2.4°$ and the crystal temperature is $T = 48.8°C$.

Appendix C.   Extended set of experimental observations

In this appendix, the more detailed set of the experimental observations made with the Mk-II experiment are shown for reference. The results from crystal-temperature scans and signal polar-angular scans that have been shown and compared with the theory in Section 4.2 are a selection from this set. The measurements are presented for a variety of detection integration angles which determine the rates and distribution shape, as has been discussed in Chapters 2 and 4.

The crystal temperature scans are presented in Figs. 49 through 53. These include three cases with equal aperture diameters and a single observation with unequal aperture diameters, as stated in the figure caption. The signal and idler polar angles are $\theta_{s,i} = 2.5°$ for all cases.

The signal polar angular scans are presented in Figs. 54 through 59. These include three cases with equal apertures and three cases with unequal apertures, as stated in the figure caption. The idler polar angle is a constant $\theta_{s,i} = 2.5°$ throughout the experiments. An additional plot of interest is presented in Fig. 60, where the signal-normalized pair rate P/R_s with equal 5 mm aperture diameters is seen to present a plateau. This plot uses the data from the measurement which provided Fig. 56.
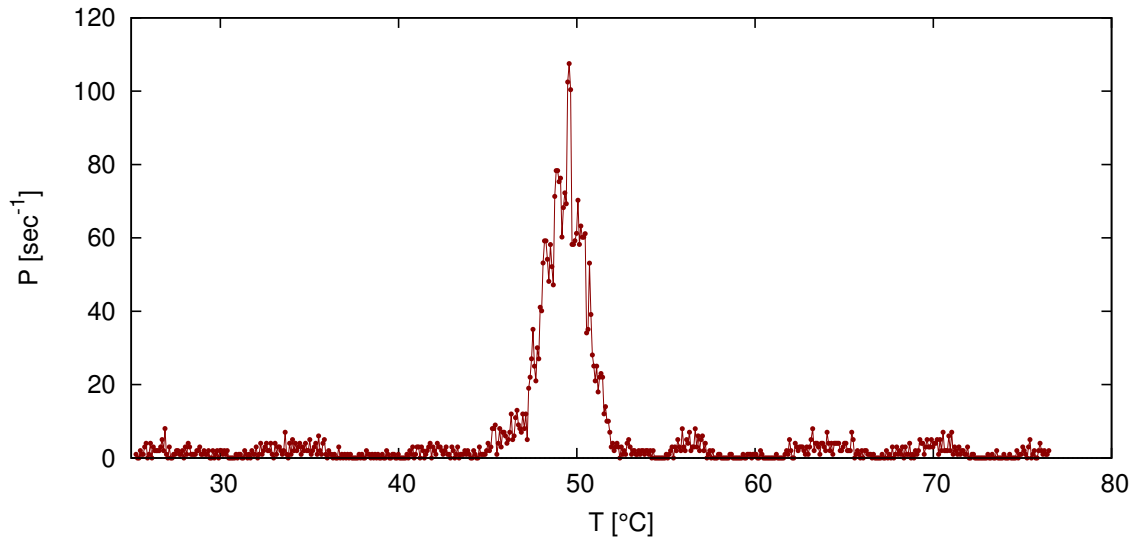
Figure 49: Measured pair rate P as a function of crystal temperature with apertures set to 0.25 mm.
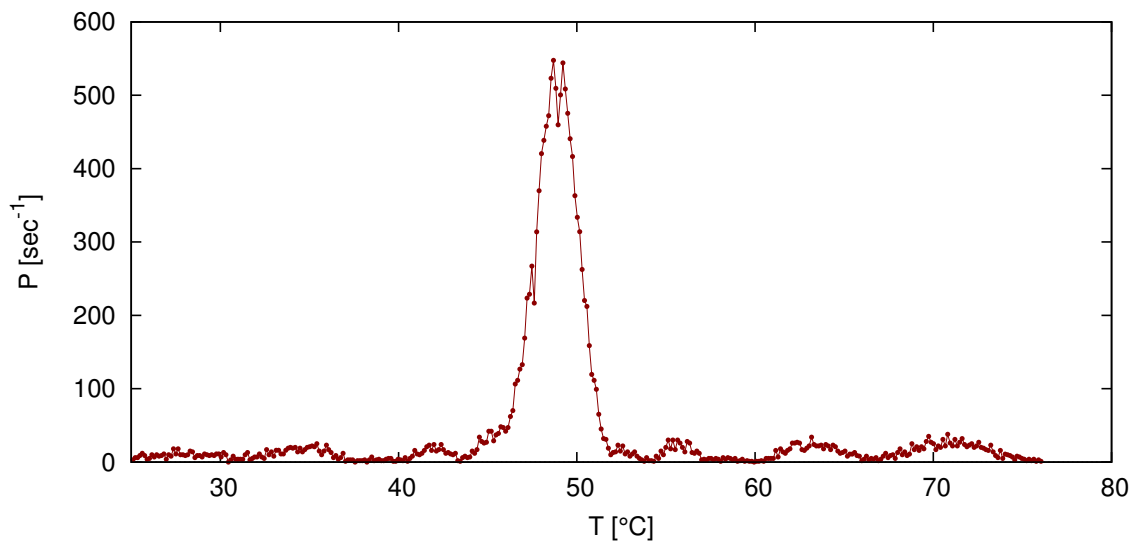

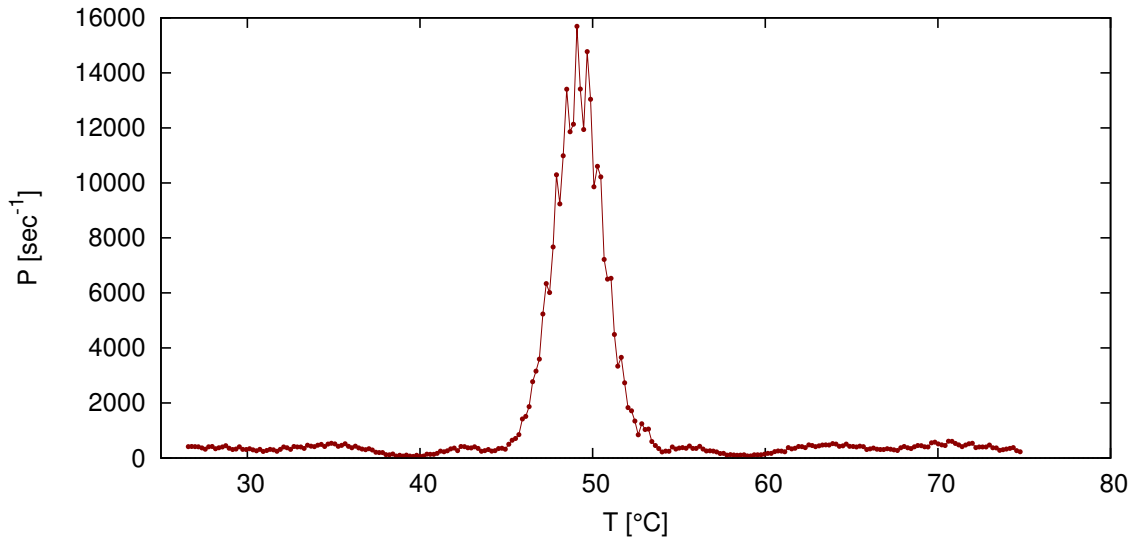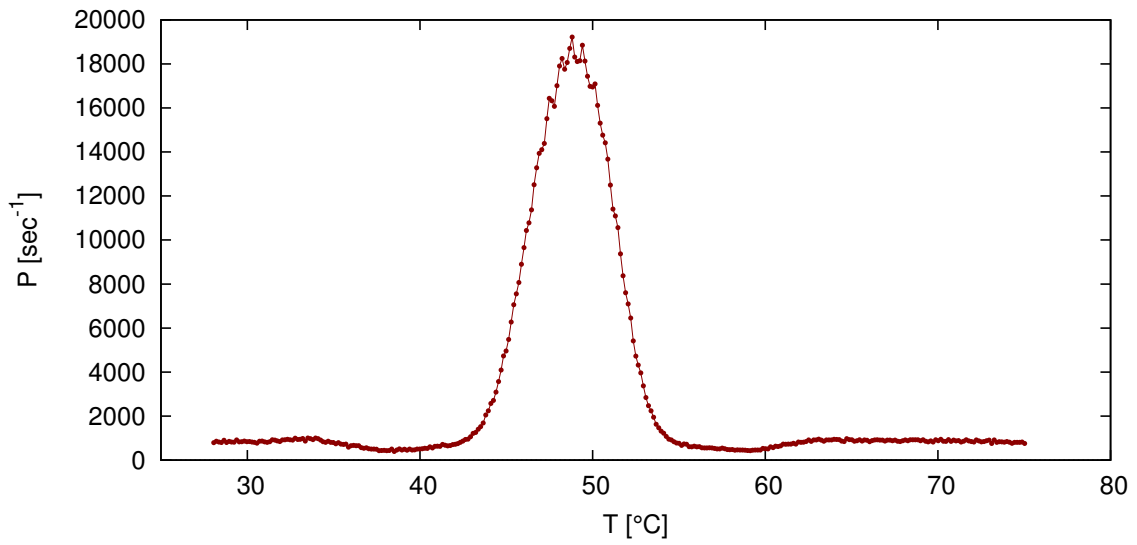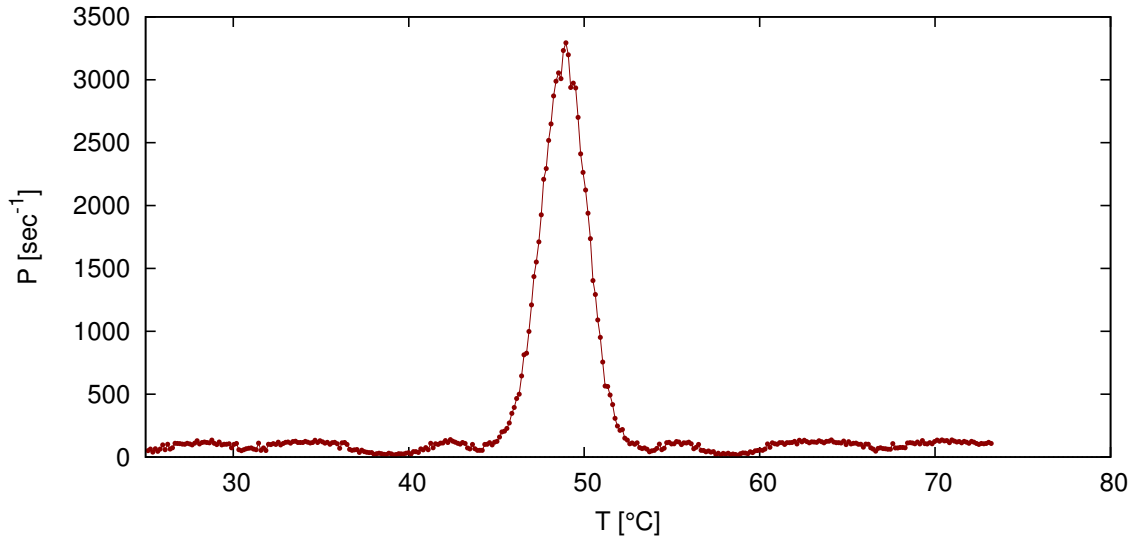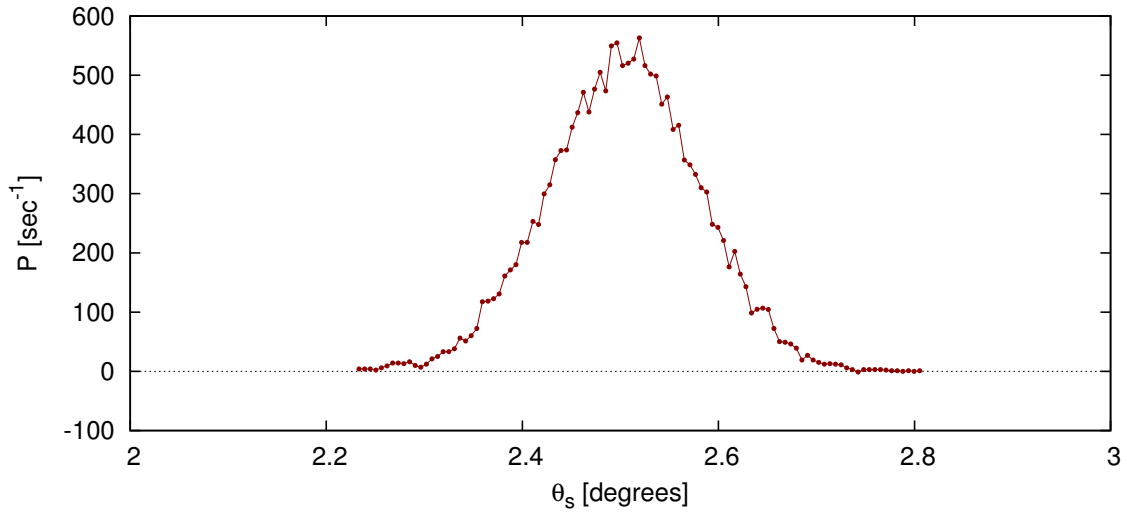**Figure 50: Measured pair rate P as a function of crystal temperature with apertures set to 0.5 mm.**

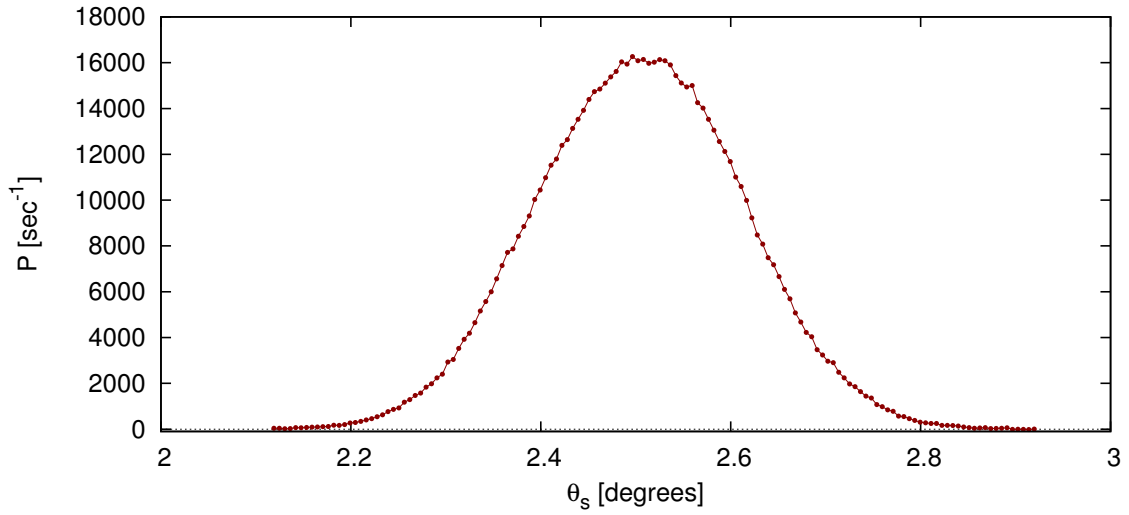**Figure 51: Measured pair rate P as a function of crystal temperature with apertures set to 3 mm.**

Figure 52: Measured pair rate P as a function of crystal temperature with apertures set to 5 mm.

Figure 53: Measured pair rate P as a function of crystal temperature with the signal aperture set to 0.5 mm and the idler aperture set to 5 mm.

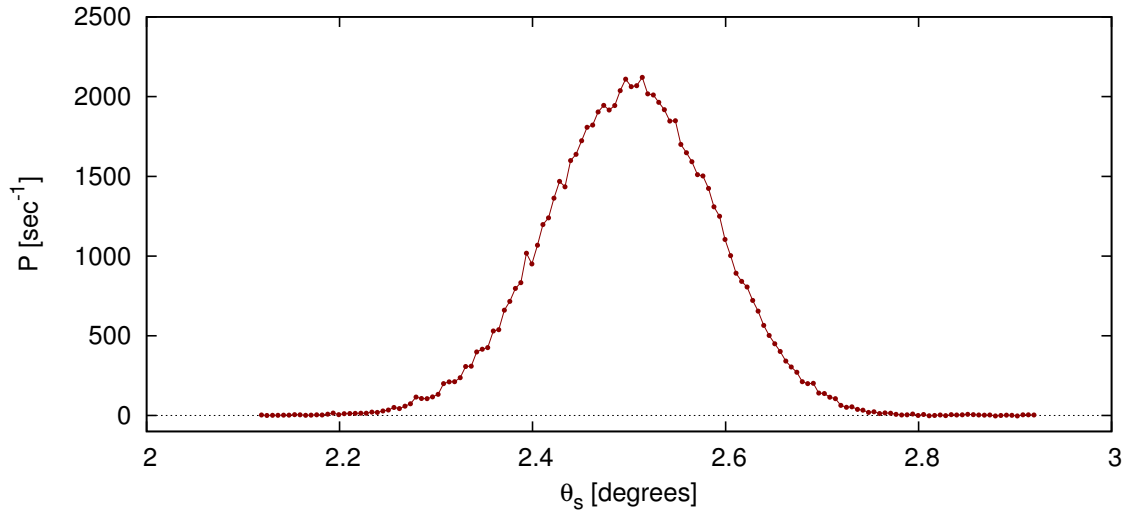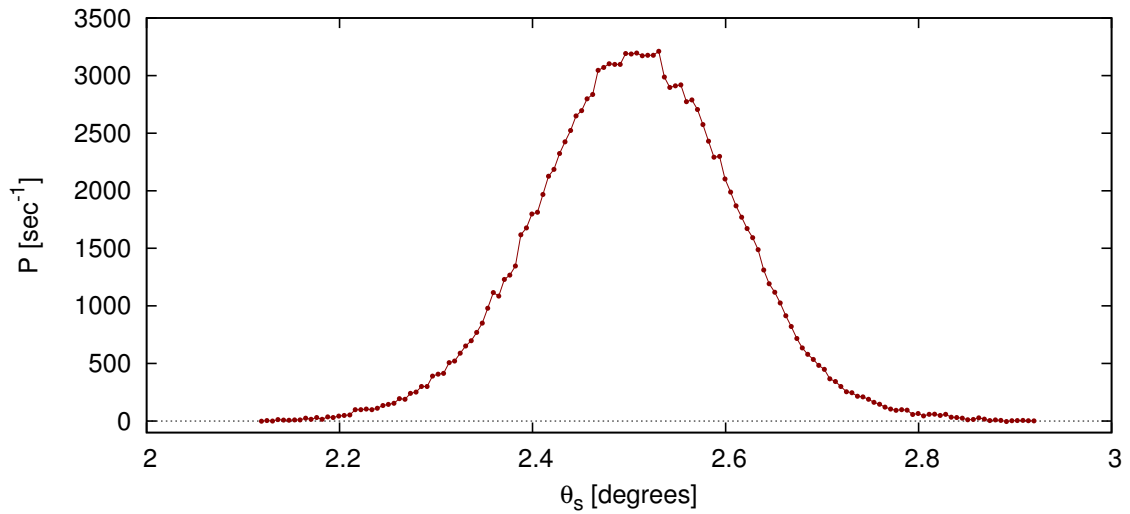**Figure 54: Measured pair rate P as a function of signal polar angle θ_s. The apertures are set to 0.5 mm.**

Figure 55: Measured pair rate P **as a function of signal polar angle** θ_s**. The apertures are set to 3 mm.**
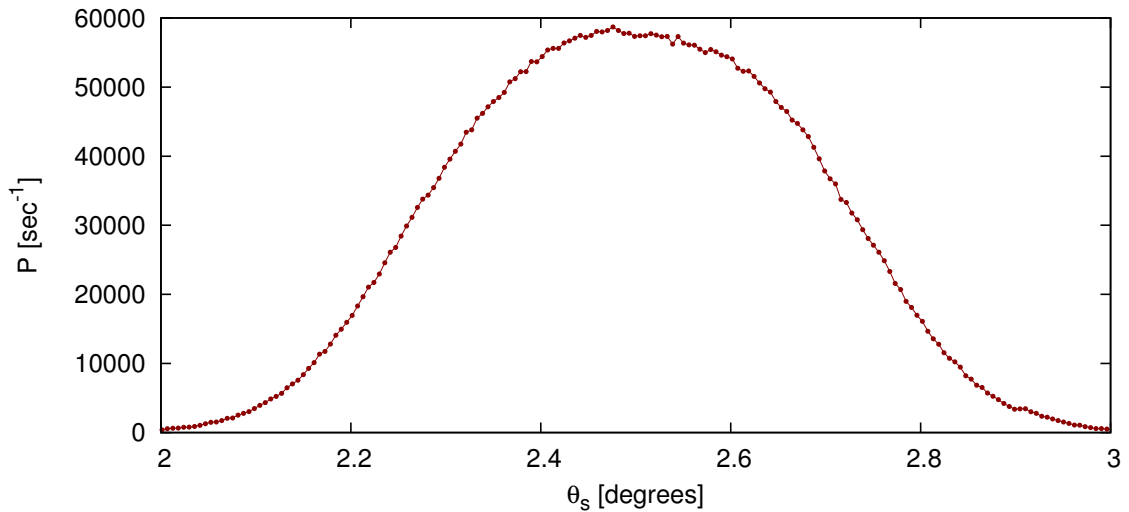
Figure 56: Measured pair rate P **as a function of signal polar angle** θ_s**. The apertures are set to 5 mm.**
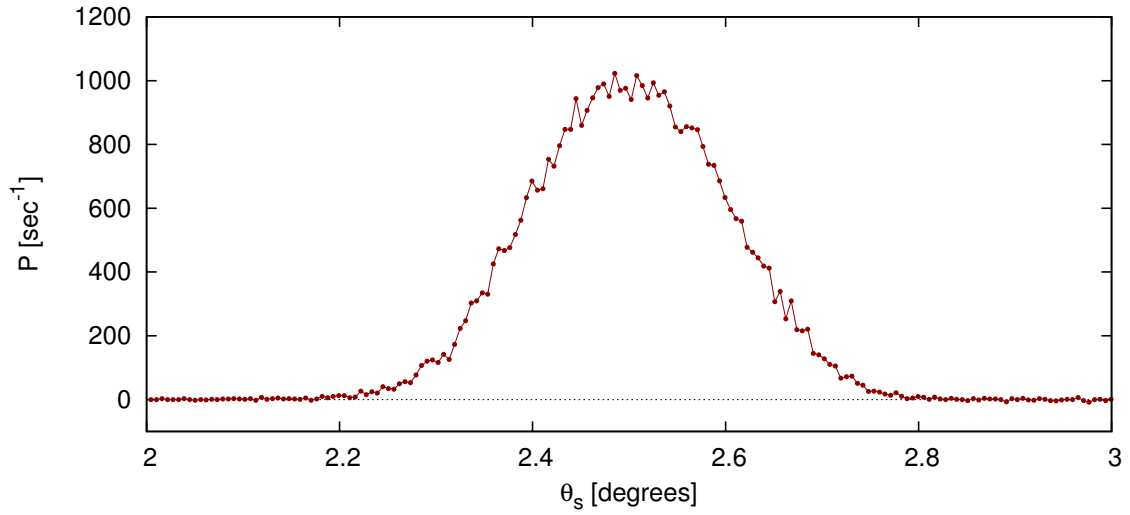
Figure 57: Measured pair rate P **as a function of signal polar angle** θ_s. **The signal aperture is 0.5 mm and the idler aperture is set to 3 mm.**

Figure 58: Measured pair rate P **as a function of signal polar angle** θ_s. **The signal aperture is 0.5 mm and the idler aperture is set to 5 mm.**

Figure 59: Measured pair rate P as a function of signal polar angle θ_s. The signal aperture is 3 mm and the idler aperture is set to 0.5 mm.
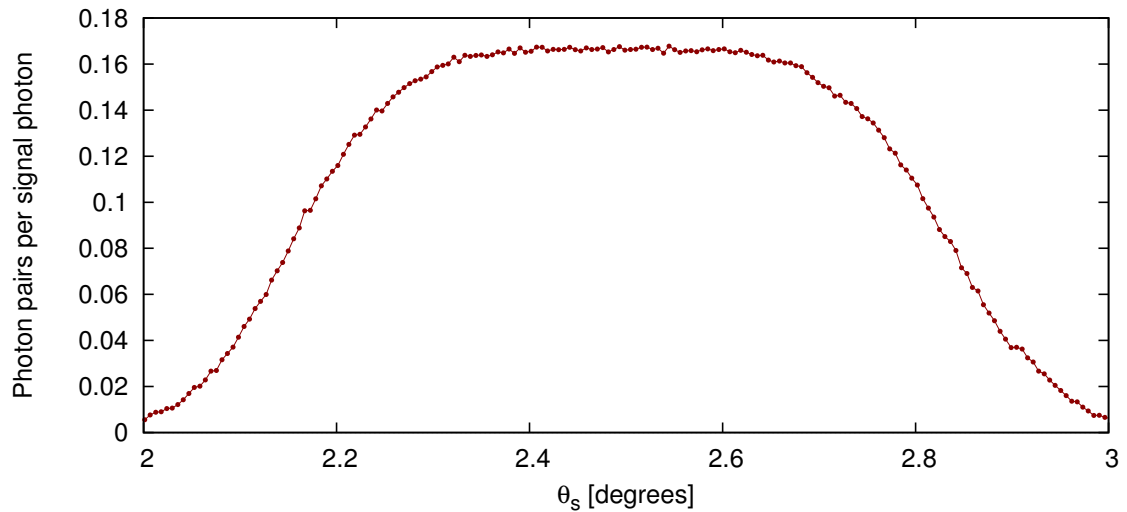
Figure 60: Measured normalized coincidence rate $\mathrm{P}/\mathrm{R}_\mathrm{s}$ as a function of signal polar angle θ_s. The apertures are set to 5 mm.